Homeostasis and Volume Regulation in the *Plasmodium Falciparum* Infected Red Blood Cell

UNIVERSITY OF CAMBRIDGE

Department of Chemical Engineering and Biotechnology

Jakob Martin Andreas Mauritz
Sidney Sussex College

A thesis submitted for the degree of
Doctor of Philosophy
January 2011

PREFACE

This dissertation is submitted for the degree of *Doctor of Philosophy*. It presents work carried out in the Department of Chemical Engineering and Biotechnology and the Department of Physiology, Development and Neuroscience of the University of Cambridge between October 2007 and October 2010. The work contained in this thesis has not been submitted for any other degree. This dissertation is the result of my own work and includes nothing which is the outcome of work done in collaboration except where specifically indicated in the text.

This dissertation contains approximately 45,000 words.

I would like to take the opportunity to thank the following people who have supported my research during this time:

Dr Alessandro Esposito
Dr Virgilio Lew
Dr Clemens F. Kaminski
Dr Teresa Tiffert
Dr Jeremy Skepper
Dr Alice Warley
Dr Jochen Guck

This work would not have been possible without the generous funding of the EPRSC and the RSC analytical science studentship.

Content

Nomenclature

CHV	Critical haemolytic volume
CLSM	Confocal laser scanning microscope
EM	Electron microscope
EPXMA	Electron probe X-ray microanalysis
FLIM	Fluorescence lifetime imaging
FRET	Förster resonance energy transfer
Hb	Haemoglobin
[Hb]	Haemoglobin concentration
IRBC	Infected red blood cell
NPP	New permeation pathway
OF	Osmotic fragility
Pf	*Plasmodium falciparum*
RBC	Red blood cell
RT	Relative tonicity

The variables of the computational model of malaria infected red blood cells are listed in a separate glossary in Appendix A.

Table of Figures

Summary

The thesis reports on the application of advanced microanalytical techniques to answer a fundamental open question on the homeostasis of *Plasmodium falciparum* infected red blood cells, namely how infected cells retain their integrity for the duration of the parasite asexual reproduction cycle. The volume and shape changes of infected cells were measured and characterized at femtolitre resolution throughout the intraerythrocytic cycle using confocal microscopy. Fluorescence lifetime imaging and electron probe X-ray microanalysis were applied for the quantification of intracellular haemoglobin and electrolyte concentrations. The cytomechanical properties of uninfected and infected red cells were studied using a novel optical stretcher device, which enabled individual cells to be trapped and manipulated optomechanically in microfluidic channels. Combined, these methods offered a unique insight into the homeostatic and rheological behaviour of malaria-infected red cells. The results were analysed by comparison with predictions from a detailed physiological model of the homeostasis and volume regulation of infected cells, providing broad support to the view that excess haemoglobin consumptions by the parasite was necessary for the integrity of infected cells (the colloidosmotic hypothesis). The dissertation is introduced with an overview of malaria, red blood cells homeostasis and the changes induced by *Plasmodium falciparum* infection. In the following, this description is extended to an in-depth theoretical analysis of the infected red blood cell homeostasis, from which the need to characterise certain parameters arises. The subsequent chapters address sequentially the assessment of the haemoglobin and electrolyte concentration, cell shape and volume changes and ultimately alterations in cell elasticity. The experimental part is complemented with a comparison of the resulting data to the predictions from the theoretical analysis and an outlook on future work.

Chapter 1: Introduction

Malaria

Malaria is one of humankind's considerable scourges. It is estimated, that every year between 300 and 500 million people worldwide are infected, with a mortality rate of over one million yearly. The disease spreads in tropical and subtropical regions through the bite of the female mosquito *anopheles.* The infection is not contagious between humans, except for unborn children who can be infected through an injured placenta (during birth). Pathogens are the protozoa of the genus *Plasmodiae*, the only pathogenic types for humans being *P. falciparum, P. vivax*, *P. malariae*, *P. ovale* and recently also *P. knowlesi.* These differ considerably in their course of disease (aetiopathology), *Plasmodium falciparum (Pf)* being the clinically most significant and severe. This is why most medical research as well as this thesis focuses on *Plasmodium falciparum*. Its incubation period is between 7 and 30 days. Symptoms of malaria are a periodically returning high fever, ague, convulsions and gastrointestinal disorders, in severe cases with lethal complications. Especially in children the illness can quickly lead to coma and death (Breman et al., 2004).

Among the various kinds of *plasmodia*, *Pf* is predominant in sub-Saharan Africa. Indeed ninety per cent of malaria sufferers live in Africa (WHO, 2009). Malaria used to be endemic in most parts of the world, but military vector control programs during World War II had proven so successful, that they were continued on a large scale afterwards. The measures included the application of insecticides (DDT) from airplanes, drainage and the removal of mosquito breeding sites. In the 1950s malaria had been eradicated from most developed countries. But anopheles mosquitoes continue to be endemic in most habitable parts of the world (Kiszewski et al., 2004). These regions are at the constant risk of re-introducing the disease.

Direct costs of malaria (for example, illness, treatment, premature death) are enormous and have been estimated to be at least US$ 12 billion per year (2009). The costs of lost economic growth in malaria endemic regions are many times more than that (McCarthy et al., 2000; Gallup and Sachs, 2001; Sachs and Malaney, 2002; Greenwood et al., 2005).

The development of a malaria vaccine has faced several obstacles in the past: the lack of a traditional market, few developers, and the technical complexity of developing any vaccine against an intracellular parasite. An acquired immunity only partially protects against future disease. Currently (2010), there is one promising candidate for a vaccine termed RTS,S in Phase III clinical trials, developed by GlaxoSmithKline plc., Brentford, UK. It is a pre-erythrocytic vaccine candidate based on the circumsporozoite surface antigen. As the probability of intercepting all sporozoites in time after a mosquito bloodmeal is low, the vaccine protection is only partial and the efficacy of the drug is below 60% (Alonso et al., 2004; Alonso et al., 2005). A good source for more general information is the online malaria compendium of the Centre for Disease Control and Prevention, Atlanta, USA (CDC, 2008).

The homeostasis of the human red blood cell

The main function of red blood cells (in the following RBCs) is the transport of oxygen and CO_2 between the lungs and the body tissues. Haemoglobin, which is present at a very high concentration in mature RBC acts as carrier molecule for O_2. RBCs completely lack intracellular structures such as organelles or a nucleus, but the red cell membrane has a plethora of membrane transport systems, some of them having no known functions in the mature cell. These are thought to be vestiges from the cells from which the erythrocyte is derived, which have much higher metabolic and biosynthetic requirements.(Kirk, 2001).

Homeostasis is the ability of the cell to regulate its volume, pH, membrane potential and ion content within narrow margins over the whole RBC life span of 120 days.

The complexity of the main active and passive processes involved in the erythrocyte homeostasis can be appreciated in Figure 1. These comprise the main passive and active ion transporters, the Jacobs-Stewart mechanism, the volume occupancy and non-ideal osmotic behaviour of haemoglobin, the composition and charge distribution on the impermeant cell solutes, and the proton, Ca^{2+} and Mg^{2+} buffering behaviour of the erythrocyte cytoplasm (Lew and Hockaday, 1999).

The Jacobs-Stewart mechanism (Jacobs and Stewarts, 1947) is the combined operation of the anion exchange carrier (AE1) and a CO_2 shunt (rapid diffusive exchange across the cell membrane). CO_2 diffuses through the shunt and is converted to bicarbonate by the enzymatic activity of carbonic anhydrase according to $H_2O+CO_2 \leftrightarrow HCO_3^- + H^+$.

The proton is buffered by haemoglobin whereas only a fraction of the CO_2 binds to Hb (carbaminohaemoglobin). The excess HCO_3^- is extruded from the cytosol via the AE1, which rapidly equilibrates intra- and extracellular chloride and bicarbonate concentrations. AE1 is a band 3 counter-transporter, mediating electroneutral exchange of chloride and bicarbonate at a 1:1 stoichiometry.

The combined contributions of the Ca^{2+}-ATPase, extruding Ca^{2+} from the cytosol, the cytoplasmic Ca^{2+} buffers and endocytotic vesicles keep the intracellular (free) calcium concentration, $[Ca^+]_i$ very low, at levels around 50nM (Lew et al., 1982; Gilboa et al., 1994).

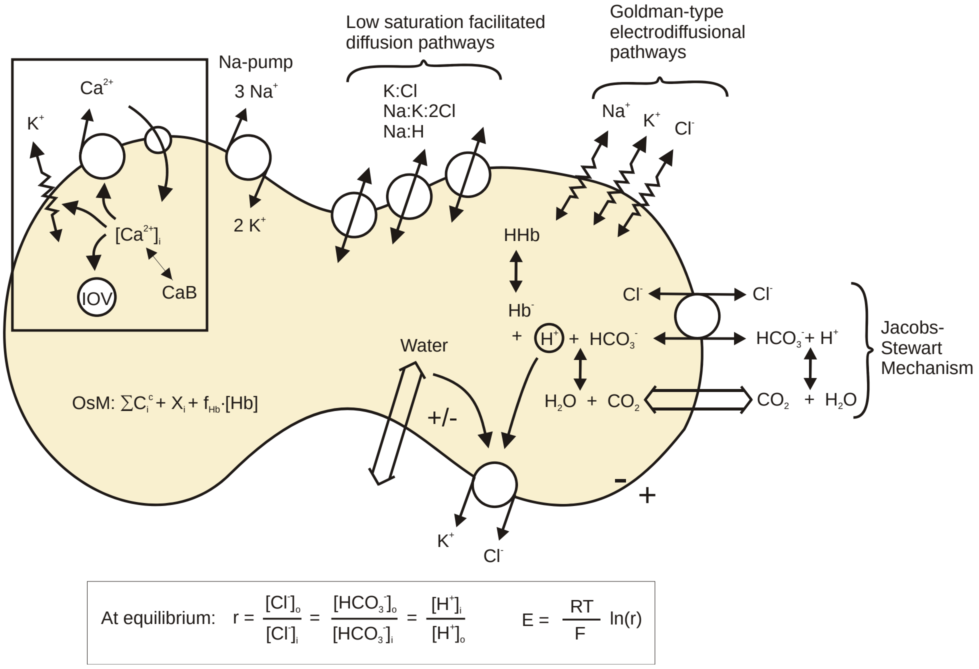

Figure 1: Mechanisms of red blood cell homeostasis. *The image identifies the main regulatory processes in RBC homeostasis. These comprise the Jacobs-Stewart mechanism, the electrodiffusional and low saturation facilitated diffusion pathways, the* Na^+*- and* Ca^{2+}*-ATPases, endocytotic inside out vesicles (IOV), aquaporins, the proton and* Ca^{2+} *buffers (HHb and CaB), the contribution of haemoglobin (Hb) and impermeant anions (X) to cell osmolality (OsM) and charge, the membrane potential (+/-/E), the equilibrium distribution of transported anions and protons (r) and the control of K:Cl cotransport activity by cell volume and pHi. Figure adapted from (Lew and Hockaday, 1999).*

The fluxes through the Goldman-type electro-diffusional pathways (including the Ca^{2+}-sensitive K^+ (Gardos) channel, KCNN4) are also regulated by the membrane potential of the RBC, whereas the fluxes of the low saturation facilitated diffusional pathways depend mainly on the concentration gradients of the substrates across the membrane.

The latter lump together all other possible passive membrane mechanisms (Lew and Bookchin, 1986), namely the Na:K:2Cl, K:Cl, Na:Cl cotransporters and the Na:H exchanger.

The Na^+-pump consumes ATP to extrude Na^+ out of the cytosol in exchange for K^+ at a K:Na stoichiometry of 2:3, thus maintaining a steep K^+ / Na^+ gradient with respect to the extracellular medium. This chemical potential can serve as an additional energy source and facilitates co-transport of other ions.

RBC volume regulation is determined by the pump-leak traffic of Na^+ and K^+ since the membrane is highly permeable to water (through aquaporins). Water fluxes are driven by the osmotic gradient generated by net salt transfers (noting the contribution of impermeant haemoglobin to the total osmolality of the cell).

At equilibrium, the concentration ratios of Cl^-, HCO_3^- and H^+ follow $r_H = [H_i^+]/[H_0^+] = [A_0^-]/[A_i^-]$, which applies to any permeable anion A^- and also to the sum of all permeable anions present in the system (Funder and Wieth, 1966).

If an outward concentration gradient of A^- is set up, thus perturbing the initial equilibrium, even contaminant traces of HCO_3^- ions will provide a rapid exchange of HCO_3^- for Cl^- through the powerful anion exchanger. The CO_2 shunt effectively prevents the buildup of intracellular HCO_3^- or the maintenance of meaningful CO_2 gradients. The net result is therefore a 1:1 exit of H and Cl from the cells with deprotonation of haemoglobin and cell dehydration (Bookchin et al., 1984). This proceeds until a new equilibrium is reached, again defined by $r_{Cl} = r_H$. This ratio determines the membrane potential. Because the diffusional permeability of permeant anions, thought to represent an infrequent (1/10000) slippage through the anion exchange carrier, is several orders of magnitude greater than that of any cation permeability, the Nernst equation can be used as a simplified approximation of the membrane potential (E, bottom of Figure 1), neglecting cationic contributions.

Plasmodium falciparum – the asexual stage

In the course of its life cycle (Figure 2), *Pf* changes its host (CDC, 2008). Humans serve as intermediary hosts (the parasite's asexual reproduction stage), while the sexual reproduction stage takes place in the *anopheles* mosquito. Humans are infected by the transfer of *aporozoites* from the mosquito saliva during its bloodmeal. The aporozoites are transported through the circulation to the liver, where they invade hepatocytes and develop to liver *schizonts*. After reproducing asexually in the liver, the organism differentiates into *merozoites* (up to 30.000 per liver cell), which are released into the blood circulation after rupturing the liver cell. The merozoites invade red blood cells in the circulation and progress to the ring stage, termed after the microscopic appearance of the parasite at this stage. After a relatively quiescent period of about 15-20 h post-invasion, the infected red blood cells (RBCs) exhibit huge increases in metabolic activity and solute traffic across their membrane which persist until the end of the asexual reproduction cycle of the parasite, about 48 h post-invasion (Ginsburg and Stein, 1987; Ginsburg, 1988; Kanaani and Ginsburg, 1988; Kanaani and Ginsburg, 1989; Kanaani and Ginsburg, 1991; Kirk et al., 1999; Kirk, 2001). The infection then progresses to the trophozoite stage (24-30 h post invasion) with the nucleated parasite displaying a prominent food vacuole.

The parasite ingests through endocytosis and degrades up to 80 per cent of the host cell haemoglobin, which is typically present at a concentration of 7 mM in the uninfected red blood cell. Haemoglobin is degraded into haeme and globin, and the globin is further digested to small peptides in the food vacuole and to aminoacids in the parasite cytoplasm. Only a fraction (~15%) of these aminoacids is used for the synthesis of new parasite proteins. The remainder is exported out of the cell (Krugliak et al., 2002). To avoid the potent oxidative stress caused by the haeme moiety, the haeme is further processed and stored in the parasitic food-vacuole in the more inert form of haemozoin, an iron containing polymer crystal. In the final schizont stage the parasite segments and develops several nuclei. The infected red blood cell (IRBC) ruptures at 48 h post-invasion to release between 10 and 32 new merozoites into the blood circulation, which restart the erythrocytic cycle by invading new RBCs.

The new permeation pathways (NPPs) induced by Pf infection.

The previous homeostatic condition of the RBC is considerably disturbed during *Pf* infection. The biggest homeostatic change is the induction of so called new permeation pathways (NPP) into the red cell membrane.

The molecular nature of the NPPs is not clearly identified yet, but their function and permeability to the most relevant physiological ions is well characterized. The NPPs behave like a pore or a channel, with very low ion selectivity. Their main functions are thought to comprise an increased nutrient uptake (glutamate, pantothenic acid), metabolic waste disposal (lactate, glutathione), volume regulation of the IRBC and changing the ionic composition of the cytosol during the trophozoite stage of the parasite (Kirk, 2001) . It is still an open question whether the NPPs are inserted by the parasite into the host cell membrane or represent parasitic re-activation of an existing silent channel, that had been active in earlier developmental stages, and that is not functional in mature erythrocytes. (Kirk, 2001).

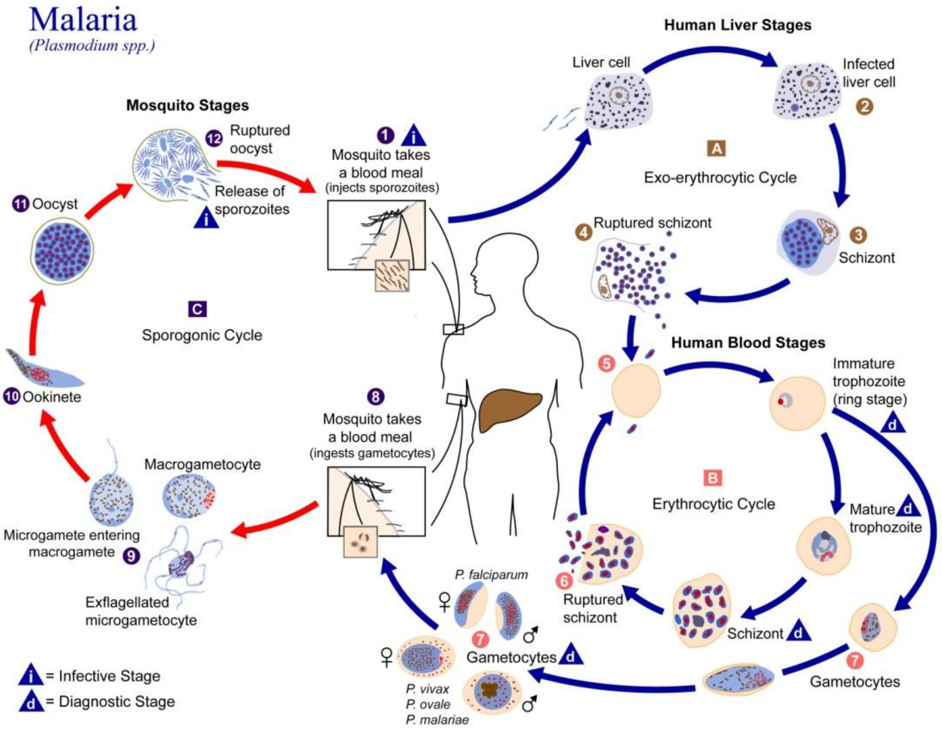

__Figure 2 : Life cycle of Plasmodia__ (Courtesy of Centre for Disease Control, Atlanta (Da Silva and Moser, 2002)). __(1)__ Humans are infected through the intravenous release of sporozoites from the mosquito saliva during its bloodmeal. __(2)__ These are transported through the circulation to the liver, where they invade the hepatocytes and develop to liver schizonts __(3)__. __(4)__ After reproducing asexually in the liver the organism differentiates into merozoites (up to 30,000 per cell), which are released into the blood circulation after the rupture of the liver cell. __(5)__ The merozoites invade the red blood cells and progress to the ring stage. After the parasites mature to schizonts, the IRBC ruptures __(6)__ and releases new merozoites that restart the erythrocytic cycle. __(7)__ In each cycle a small number of parasites develop into the sexual form called gametocytes. The male gametocytes are called microgametocytes, the female macrogametocytes. __(8)__ The gametocytes can be picked up by mosquitoes during a bite. In the mosquito intestine the gametocytes develop into gametes. __(9)__ The microgamete

penetrates the macrogamete forming a zygote. ***(10)*** *The zygote changes into a motile, linear form called the ookinete which nests between the tissue layers of the mosquito intestine and turns into an oocyste* ***(11)****. About 1.000 new sporozoites develop in the oocyste, which travel into the salivary glands of the mosquito and are ready for re-infecting a human* ***(12)*** *Adapted from (Da Silva and Moser, 2002).*

Puzzles and open Questions

Staines et al. (Staines et al., 2001) calculated that if uninfected human RBCs were permeabilized to the same extent than IRBCs, the uninfected cells would haemolyze by the unbalanced net gain of NaCl and osmotic water over a shorter time-course than that needed for parasite maturation and exit. How can the integrity of parasitized cells be preserved for the duration of the intraerythrocytic cycle, considering that they have a parasite growing to a substantial volume inside?

This puzzle prompted an investigation on how premature lysis is prevented in falciparum-infected RBCs. A mathematical model of the homeostasis of parasitized RBCs was formulated to attempt an understanding of the processes involved (Lew et al., 2003). The model encoded all known kinetic parameters relevant to the control of host red cell volume, i.e. pH, membrane potential, ion content, ion transport across the RBC membrane and parasite growth. The initial simulations with the model produced a result which led to the formulation of a “colloid-osmotic hypothesis” to explain how infected RBCs (IRBCs) resist premature lysis (Lew et al., 2003; Lew et al., 2004). The hypothesis linked lysis resistance to haemoglobin consumption, a link hitherto never suspected.

It had been well established that during the process of growth and maturation within RBCs malaria parasites ingest and digest haemoglobin (Hb) to levels far above those required by parasite protein synthesis

(Zarchin et al., 1986). Moreover, the amino acids produced in vast excess by haemoglobin proteolysis are rapidly released to the medium across the host RBC membrane through the NPPs (Ginsburg et al., 1983; Ginsburg et al., 1985; Zarchin et al., 1986; Kirk, 2001; Krugliak et al., 2002), without apparent generation of any osmotic stress. Hb ingestion, digestion and haeme detoxification, required to prevent damage to both parasite and host cell, are high energy-consuming processes (Orjih et al., 1981; Ridley et al., 1997; Ginsburg et al., 1999). It was therefore puzzling why Hb was consumed in such vast excess. The original model simulations (Lew et al., 2003) suggested that excess Hb digestion was necessary to reduce the colloid-osmotic pressure within the host cell, thus preventing its premature swelling to the critical haemolytic volume (CHV).

Issues addressed in the present investigation

The main aim of the experimental work reported in this thesis was to test the critical predictions of the colloidosmotic hypothesis, and through these, the validity of the ideas encoded in the model. The thesis presents a detailed re-assessment and analysis of the homeostasis of *P. falciparum*-infected RBCs in the light of the new experimental results.

The key prediction of this model was that the Hb concentration within the host cell, not just its Hb content, had to decrease monotonically during the second half of the asexual reproduction cycle. Therefore in Chapter 3 an assay based on fluorescence lifetime imaging microscopy (FLIM) is presented, capable of measuring intraerythrocytic Hb concentration quantitatively in live IRBCs. Chapter 4 presents additional results on the use of electron probe X-Ray microanalysis. This method is particularly suited to quantify the elemental composition of thin cell sections. These data reveal more detailed information, not only on intracellular Hb concentration but also on the accompanying electrolyte composition of the host and parasite cytosol.

An ongoing dispute in the literature concerns the volume variations of the infected red blood cell during the parasite cycle (Zanner et al., 1990; Saliba et al., 1998; Elliott et al., 2001; Allen and Kirk, 2004; Lew et al., 2004). All claims so far are based on indirect observations, which is why a clarifying, direct measurement of IRBC volumes is needed. Chapter 5 presents such IRBC volume measurements performed with high resolution confocal microscopy. The findings showed that the IRBC volumes are largely conserved during parasite development and that there is a significant loss of membrane surface area. The extent of membrane area loss was not sufficient to account for the marked increase in the osmotic fragility of IRBCs with late-stage parasites. The reason may be found in the stiffening of the host cell membrane during the parasitic cycle.

Therefore Chapter 6 is devoted to assess the mechanical properties of the cell membrane with optical stretcher. This novel technique allows quick characterisation of the cell mechanics and has also future potential in automated screening and cell sorting applications.

In summary, the novel contributions of this thesis are an improved understanding of the homeostasis of *Plasmodium falciparum*-infected red blood cells. This has been achieved through modelling the homeostatic processes involved and experimentally characterising important stage-dependent parameters. These comprise the quantification of electrolyte and haemoglobin concentrations in the host cytosol and a more accurate assessment of cell volume and cell elasticity by employing advanced measurement techniques.

Chapter 2: Understanding the homeostasis of normal and falciparum-infected human red blood cells

Introduction

Although the empirical kinetics for each single membrane pathway can be described by relatively simple equations, the combined interaction of only the main transport processes creates significant complexity, which quickly goes beyond intuitive grasp (compare also Figure 1). Under these circumstances a need for modelling arises. Simulating the combined effects of several processes allows the modeller to vary its input parameters and anticipate responses under physiological, pathological and experimental conditions. The goal of modelling in general is achieved when it provides *additional* insight by unexpected explanatory links or new, testable predictions. The red cell model has provided several of these in the past, including an improved understanding of sickle-cell disease (Lew and Bookchin, 1986; Bookchin et al., 1991; Lew et al., 1991) and the formulation of the colloid-osmotic hypothesis in malaria infected red blood cells (Lew et al., 2003; Lew et al., 2004).

The original simulations of the *Pf* infected erythrocyte led to two critical predictions: i) that excess Hb ingestion and digestion would cause not only a dramatic fall in the Hb content of the host cell, as had been established already from experimental evidence, but also a progressive and large decline in its Hb *concentration*, and ii) that parasite volume growth together with host cell swelling late in the cell cycle would bring IRBC volumes very near their CHV. Allen and Kirk (Allen and Kirk, 2004) argued that parasite volume growth was overestimated in the model because of its assumption that the parasite retains all of the volume taken up via the endocytotic feeding process, leading to exaggerated IRBC volume estimates. They stressed that most of the host volume ingested may be lost by different processes (e.g, Hb breakdown, Na^+ extrusion from the parasite compartment) thus freeing up space for the parasite to expand into the host cell and limit the extent of swelling undergone by the infected cell as the parasite volume increases and cations enter the cell through colloid-osmosis. If IRBC volumes do not approach the presumed CHVs, then both the role attributed by the model to excess Hb consumption and the need for freeing space appear irrelevant. It became clear from these considerations that a thorough re-evaluation of the model assumptions and predictions in the light of past and recent experimental evidence became necessary.

The original model simulations (Lew et al., 2003) were generated using a restricted set of parameter values and were reported using a minimal subset of model variables, leaving out much potentially useful information on the homeostasis of IRBCs. The present account overcomes these shortcomings and defines the current understanding of the homeostasis of *P. falciparum*-infected RBCs. Furthermore it integrates the findings of experiments that were performed to critically test and potentially falsify this model.

For improved readability, the algorithm used for these simulations is described in Appendix A. It was developed and implemented in PowerBasic by Dr Lew of the University of Cambridge. It is based on the red cell model (Lew and Bookchin, 1986) and was adapted for simulating malaria infected red blood cells (Lew et al., 2003). This model has been modified since, allowing for a volume growth that is only proportional (previously: equal) to the volume of digested haemoglobin. The results produced for this extensive analysis were made possible through automating the execution of the model by the author (using Matlab scripts and modifying the Powerbasic source code). In several sequential auto-executed runs, the model would assume a predefined set of parameters for each new simulation and thus generate a predictive range (“landscape”) of target variables.

Results

The presentation of the results below, and their analysis, was guided by two specific aims: to provide a critical overview of the experimental evidence on which the information encoded in the model is based, and to allow a rational exploration of the model predictions over a wide range of possible parameter values. This exercise is necessary to enable predictions to be confronted with available results in the literature, to outline the open questions in the field and to direct future research.

Figure 3A illustrates the time courses of NPP development and of Hb consumption, as encoded in the original version of the model, based on the experimental results from Staines et al., (Staines et al., 2001) and from Krugliak et al., (Krugliak et al., 2002), respectively. Figure 3B shows the time-dependent increase in Na^+, K^+ and anion permeabilities through the NPP pathway (Kirk, 2001). Note the difference in ordinate scales between anion and cation permeabilities, corresponding to the well-documented anion selectivity of the NPP pathway (Kirk, 2001; Ginsburg and Stein, 2004). We analyse first the rationale behind the two curves in Figure 3A and then the significance of the time shifts between the onset of the NPP-mediated permeabilization and of Hb consumption.

NPP development.

The stage-dependent changes in NPP-mediated permeabilities were measured in samples from synchronized Pf cultures (Staines et al., 2001). They were encoded in the model as represented in Figure 3A-B. The curves may be interpreted in either of two ways: as a gradual simultaneous increase in NPP-mediated permeability in all the parasitized cells (graded response), or as the net population variation in onset time of sudden permeability changes in individual cells (all-or-none response). Can the available experimental evidence help discriminate between graded or all-or-none alternatives? Isotonic solutions of NPP-permeant solutes such as sorbitol have been extensively used to selectively haemolyse IRBC with developed NPPs (Lambros and Vanderberg, 1979).

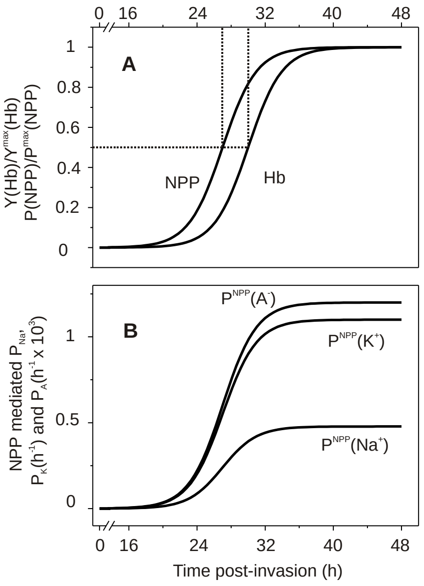

Figure 3: NPP development and Hb consumption as a function of time post-invasion*. Panel A: Normalized time-course of NPP development and of Hb consumption as originally encoded in the model (Lew et al., 2003; Lew et al., 2004) represented as fraction of maximal NPP permeability (P_{NPP}/P^{max}_{NPP}) and maximal digested Hb (Y_{Hb}/Y^{max}_{Hb}), respectively (see equations S**32** and S**33** in Appendix A). The half-time and slope values for the NPP and Hb curves shown here were (in h) 27-2 and 30-2, respectively. Panel B: cation and anion permeabilities through NPPs as a function of time. Note the difference of three orders of magnitude between cation and anion permeabilities.*

Analysis of the lysis kinetics of IRBCs renders results compatible with both types of responses (Krugliak and Ginsburg, 2006). Patch-clamp studies have not yet documented intermediate conductance stages in NPP activated IRBCs (Bouyer et al., 2007). Therefore, the all or none response remains a distinct possibility, deserving investigation here by analysing the predicted effects of a sudden increase in NPP-mediated permeability.

Haemoglobin consumption and significance of the time-difference between NPP development and haemoglobin consumption.

The stage-dependent changes in Hb consumption were defined within wide error margins (Krugliak et al., 2002; Elliott et al., 2008). Hb consumption of up to 80% of the host cell Hb is known to proceed gradually (see. e.g. (Elliott et al., 2008)), and there is no “all or none” alternative to gradual Hb consumption. The most important and well supported feature of the two curves in Figure 3A is that NPP development precedes Hb consumption. Sorbitol, alanine and other solutes whose permeability through uninfected RBC membranes is negligible have been extensively used to probe for NPP permeabilization (Kirk, 2001). In isotonic solutions of sorbitol or alanine, IRBCs with developed NPPs rapidly lyse; only those with young ring-stage parasites remain intact. The importance of delayed Hb digestion relative to NPP development is that by the time the large excess of amino acids produced by globin proteolysis reaches the host cell membrane, the permeability path available for their rapid downgradient exit is available, thus preventing osmotic stress from accumulated amino acids within the host. However, the experimental errors in the observed half-times of NPP development and Hb ingestion curves are relatively large and the possible effects of interval variations between the curves in Figure 3 on IRBC homeostasis deserve exploration.

IRBC homeostasis.

Figures 4 and 5 show the results of a typical simulation with parameter values chosen for convenient illustration of the five homeostatic periods defined by inflexions in the curves reporting net fluid movements in the host RBC (Phases 1 to 5 in Figure 4A). The model predictions here allow a detailed analysis of the homeostatic processes at work during the different stages of parasite development.

During the stage of *initial quiescence* (Phase 1), from invasion to about 20h post-invasion, all IRBC variables remain essentially unchanged from their initial levels. Phase 2, *K^+-driven net fluid loss*, is triggered by NPP activation. The immediate effect of the increase in Na^+, K^+ and anion (A^-) permeabilities (Figure 3B) is to induce the dissipation of the steep initial Na^+ and K^+ gradients (Figure 4B-C), unrestricted by co-anion movements (Ginsburg et al., 1986; Lee et al., 1988).

Initially the opposite driving forces for Na^+ and K^+ gradient dissipation have similar magnitude, as represented in Figure 4D-E by the respective electrochemical driving gradients ΔE_{Na} and ΔE_K. The P_K/P_{Na} permeability ratio for cation selectivities is however set at 2.3 (Staines et al., 2001) and thus determines that the loss of KCl transiently exceeds NaCl gain. This causes a transient net fall in RBC cytosolic anion content and concentration (Figure 4, panels B and C, respectively) and net loss of water (Figure 4A, solid triangles and Figure 4F). Figure 5A shows that the K^+ efflux, which initially exceeds Na^+ influx, rapidly returns to near-zero baseline levels as the K^+ gradient is dissipated.

The transient dehydration of the IRBC during this second period generates secondary transient changes in other homeostatic variables: increase in Hb concentration (Figure 5B), reduced anion content (Figure 4B, A^-) and anion concentration (Figure 4C, $[A^-]$), and cell acidification (Figure 5C). The transient acidification results from the brief increase in $[Cl^-]_o/[Cl^-]_i$ ratio due to net KCl loss; the combined operation of the CO_2 shunt and anion exchanger rapidly readjusts the proton ratio to restore the equilibrium condition $[H^+]_i/[H^+]_o = [Cl^-]_o/[Cl^-]_i$, with consequent cell acidification (Lew and Bookchin, 1986; Freeman et al., 1987; Lew and Bookchin, 2005).

In Phase 3, *Na^+-driven fluid gain*, the direction of net fluid movement is reversed following the reversal of the gradients driving net salt flows. This reversal also affects the direction of change in all associated variables (Figures 4 and 5). Figure 5A shows that the net fluxes of Na^+ and anions into the cell persist long after the net K^+ flux has returned to baseline levels, and Figure 4D-E shows the time-dependent changes in driving gradients which determine the direction of net ion and fluid fluxes at all times according to the model (see Appendix A).

In Phase 4, *fluid loss*, the rate of Hb consumption is maximal. This rate determines the volume of cytosol that the parasite needs to ingest in order to incorporate the amount of Hb prescribed by the Hb consumption function (Figure 3). When this volume exceeds the concomitant Na^+-driven fluid gain, host cell water contents and host cell volume are transiently reduced (Figure 4A). Phase 4 is characterized by the steepest rates of Hb fall (Figure 5B, Hb) and parasite growth (Figure 4A, open triangles), and by a decline in cell water (Figure 4A, solid triangles). Transient reductions in Na^+ and anion contents (Figure 4B, Na^+,A^-) result from the transfer of RBC cytosol to the parasite as part of the Hb ingestion process. Additional reduction in host cell volume results from the removal of the space occupied by Hb molecules. Hb has a specific volume of about 0.74 ml/g (Bureau and Banerjee, 1976) and contributes with about 25% to the total volume of a normal RBC. Therefore, a loss of 70-80 % of Hb from a cell containing in average 34 pg of Hb is equivalent to a volume loss of between 15-20 fl by the end of the asexual cycle.

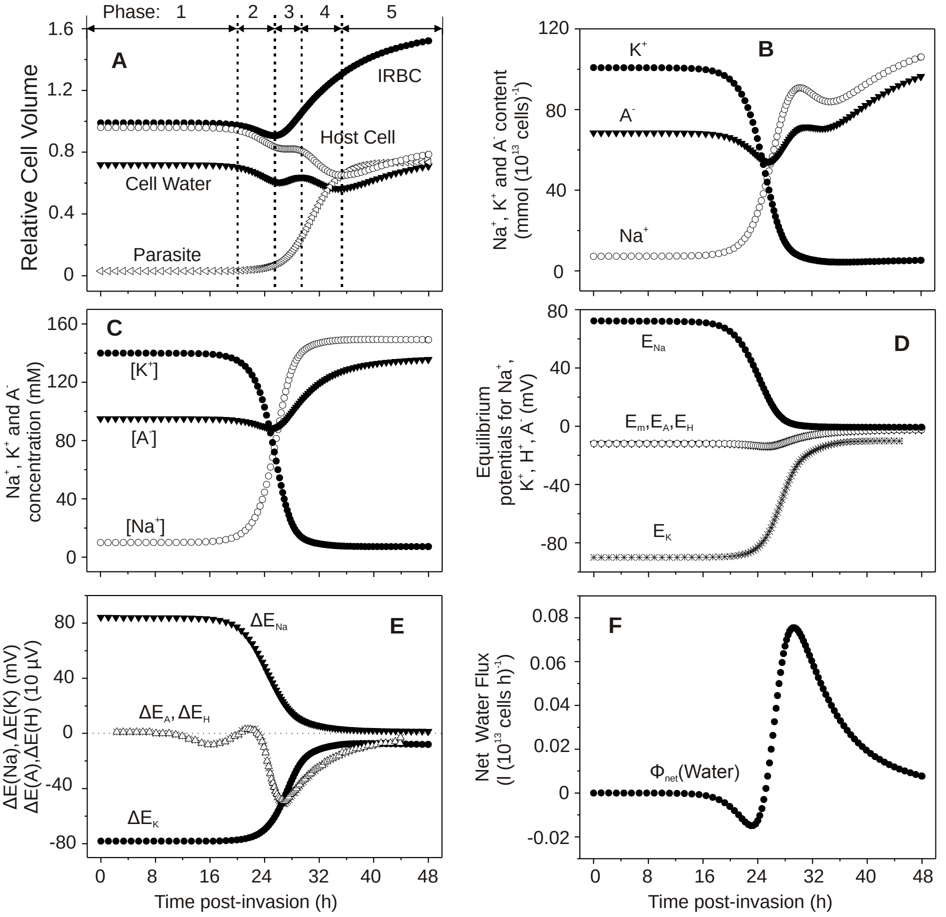

Figure 4: Predicted changes in selected model variables as a function of time post-invasion. *The parameter values chosen for this simulation were: coupling factor, 1.0; maximal fraction of Hb consumed, 0.7; half times and slope values for NPP development and Hb consumption curves as in Figure 1 (in h, 27-2 and 30-2). Panel A: volumes of parasite, host cell water, host RBC and IRBC, relative to IRBC volume at t=0. Panel B:* Na^+, K^+ *and diffusible anion content of IRBCs, in mmol* $(10^{13}\ \text{cells})^{-1}$ $(10^{13}$ *cells is taken to represent the approximate volume of a litre of normal, uninfected packed red blood cells with a mean cell volume of 100 fl). Panel C:* Na^+, K^+ *and diffusible anion concentration in host cell water, in mM. Panel D: Membrane potential* (E_m) *and equilibrium potentials (Nernst potentials) of* Na^+ (E_{Na}), K^+ (E_K), *diffusible anion* (E_A) *and protons* (E_H)

across the host cell membrane. Panel E: Differences between E_X (X = Na^+ and K^+ in mV, A^- and H^+ in mV 10^{-2}) and E_m ($\Delta E_X = E_X - E_m$), representing the changing driving forces for passive ion fluxes across the host cell membrane throughout the asexual reproduction cycle, in mV. Panel F: Net water flux across the host cell membrane, in $l(10^{13}$ cells$)^{-1}(h)^{-1}$.

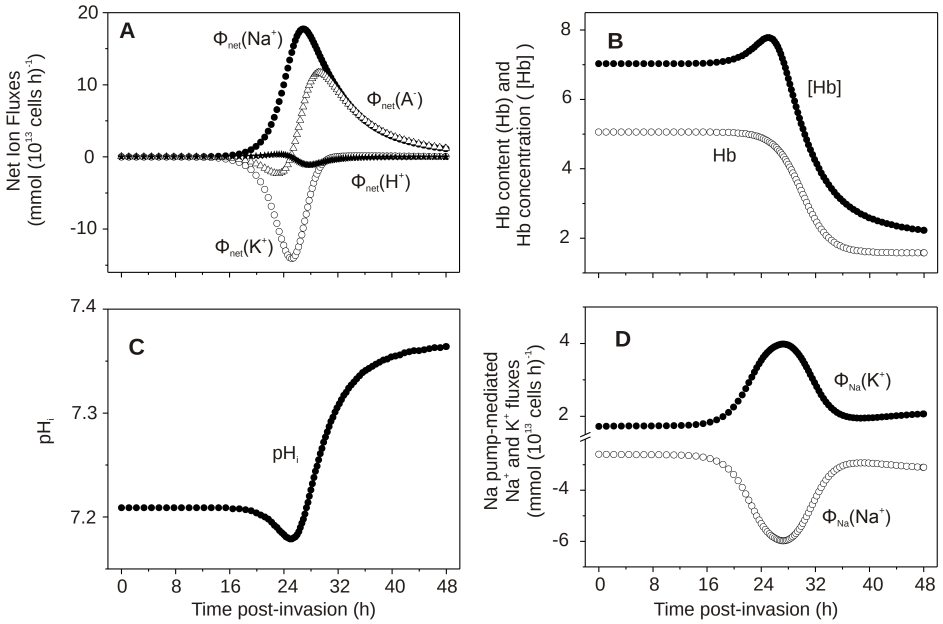

Figure 5: Predicted changes in additional model variables as a function of time post-invasion. *Panel A: Net fluxes of Na^+, K^+, A^- and H^+ across the host cell membrane, in mmol$(10^{13}$ cells$)^{-1}(h)^{-1}$. Panel B: Changes in host cell Hb content, in mmol$(10^{13}$ cells$)^{-1}$, and in Hb concentration within host cell water phase, in mM. Panel C: pH of host cytosol. Panel D: Na pump-mediated fluxes of Na^+ and K^+, in mmol$(10^{13}$ cells$)^{-1}(h)^{-1}$.*

Phase 5, *sustained swelling*, is characterized by continuous NaCl and water gains by the host cell (Figures 4A (cell water), 4B (Na^+ and A^-), and 4F) driven by the inward Na^+ gradient. The rate of fluid gain is reduced relative to that in phase 3 (Figure 4F) because of the marked reduction in driving force for net NaCl gain (Figure 4D-E) and in colloid-osmotic pressure due to the fall in Hb concentration (Figure 5B). Parasite and IRBC volumes also increase at slower rates (Figure 4A (Parasite, IRBC)) following the reduced Hb consumption and fluid gains relative to Phase 4. As the anion concentration increases (Figure 4C), the membrane potential becomes progressively more depolarized and the equilibrium potentials of all ions approach the membrane potential E_m (Figure 4D-E), with consequent cell alkalinisation (Figure 5C). The Na pump, initially stimulated by the increased intracellular Na^+ concentration, shows late inhibition (Figure 5D). This inhibition results from a predicted reduction in Mg^{2+} concentration in the host cell cytosol following global cytosolic transfers to the parasite during Hb ingestion. Late swelling further reduces the Mg^{2+} concentration. The Mg^{2+}/ATP ratio is an important regulator of Na pump activity and departure from its normal value near unity is inhibitory to the pump (Garrahan and Glynn, 1967; Flatman and Lew, 1979). Atamna and Ginsburg (Atamna and Ginsburg, 1997) measured the Mg^{2+} content of host and parasite compartments in IRBCs with mature trophozoite stage parasites and found that the Mg^{2+} content of the host cell compartment was over 60% lower than that of uninfected RBCs. They suggested that such a reduction may partially inhibit active transport by the sodium and calcium pumps. It remains to be elucidated whether the actual mechanism of Mg^{2+} deprivation in the host cell is the one implied by the model.

Figure 6 illustrates a condition in which NPPs are switched on almost instantly to analyse the homeostatic effects of all-or-none NPP activation (Figure 6A). The rest of parameter values were the same as for Figure 4. It can be seen that the main effect of all-or-none NPP activation is to compress the time-course of the events described for phase 2 (Figure 4), with relatively minor long-term quantitative changes in volumes (Figure 6B) and in Hb concentration (Figure 6C). The relative duration and magnitude of the effects described for each period in the examples chosen for Figures 4 and 6 will vary with the choice of parameter values. These effects are shown in Figure 8 and analysed below. The important point to note is that the underlying homeostatic processes described for each period remain essentially the same.

Design of a modelling strategy for parasite volume growth; introduction of a coupling factor linking parasite volume growth to haemoglobin consumption.

The time course of volume growth of *P. falciparum* parasites throughout their asexual reproduction cycle in human RBCs has not been characterized. Parasite volume increases throughout the cycle but it is unknown whether this growth is uniform or variable. The minimal final parasite volume in a cell with a single parasite has to equal the sum of the volumes of all the merozoites produced plus the volume occupied by the residual body. Without relevant information available, it was difficult to design a rational strategy to model parasite volume growth. Because the time-course of parasite volume growth could be roughly associated with that of Hb ingestion, linking these two variables was considered an acceptable modelling strategy. In the initial formulation of the model (Lew et al., 2003), parasite volume at each instant of time was defined by the cumulative volume of ingested host cell cytosol up to that time. This volume, in turn, was determined by all the complex homeostatic factors that influenced the volume of host cytosol in which the prescribed amount of Hb to be digested at each time was contained.

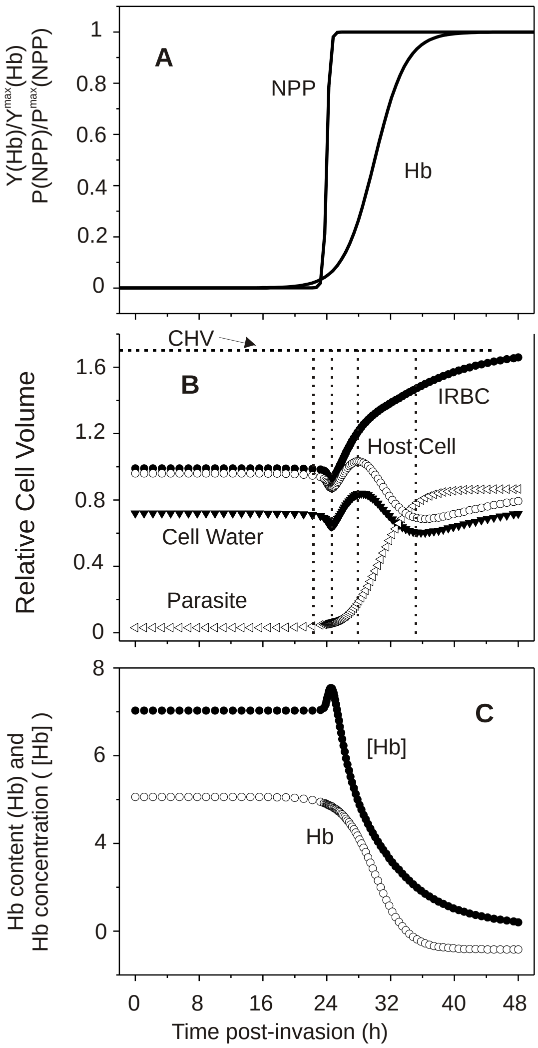

Figure 6: Time dependent effects of all-or-none NPP activation on selected model variables. *Panel A: Normalized curves representing the time-course of NPP development and of Hb consumption applied in this simulation. The half-time and slope values for the NPP and Hb curves shown here were (in h) 24-0.2 and 32-2, respectively. Panels B and C, as for Figures 2A and 3B respectively. Following Ponder (Ponder, 1948), the critical haemolytic volume shown was set at 1.7 times the relative cell volume.*

For maximal Hb consumption around 70-80%, this strategy predicted terminal parasite volumes of about 70 to 90 fl (Figure 4A, Parasite), values near the mean volume of uninfected RBCs. However, previous results suggested that this approach overestimated parasite volume.

Saliba et al. (Saliba et al., 1998) measured the water content of parasites at the mature trophozoite stage to be less than 30 fl. Recent results by Elliott et al., (Elliott et al., 2008) suggest that single parasite volumes seldom exceed 50 fl at any developmental stage. Therefore, to explore the effect of more realistic estimates of parasite volumes a coupling factor was introduced. It defines the global volume-growth of the parasite in each iteration of the numerical computation as a fraction of the volume of cytosol incorporated during that iteration (see Appendix A). For coupling factor values of less than 0.7, this approach implicitly corrects for parasite volume losses due to Hb breakdown, because, although haemozoin is retained, the volume occupied by the globin molecules largely vanishes in the process of exporting the resulting amino acids to the external medium . As explained above, this volume may account for up to 20 fl. The results of simulations using the same set of parameter values applied in the example of Figure 4, varying only the value of the coupling factor, are shown in Figure 7 which reports predicted parasite volumes as a function of time post-invasion. From these results, only coupling factor values in the range 0.3 to 0.7 appear to cover the observed range of terminal parasite volumes for single infections. This range then will be tested in the global simulations attempted below, in comparison with the original value of 1 (Lew et al., 2003; Lew et al., 2004).

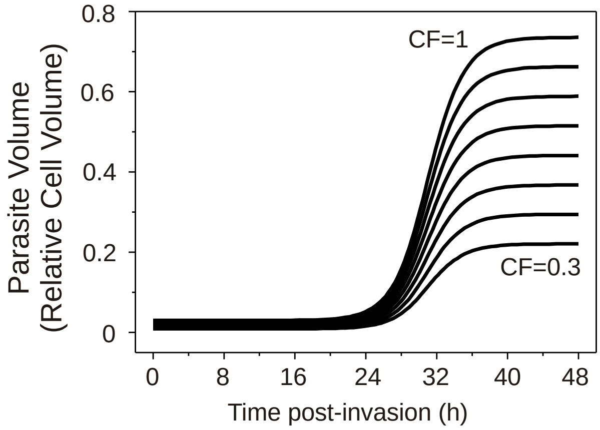

Figure 7: Effect of coupling factor on the magnitude of parasite volume-growth*. The time-course of parasite volume growth was linked to the ingestion of host cytosol. The volume of cytosol incorporated into the parasite at each instant of time is determined by the need to provide the right amount of Hb, as prescribed by the Hb consumption function (equation S****33** *in Appendix A). The coupling factor defines the fraction by which the cumulative cytostomal ingestions convert to parasite volumes (equation S****39** *in Appendix A). With a coupling factor of 1, parasite volume growth reflects the cumulative sum of all cytostomal ingestions. It can be seen that with a maximal Hb consumption set at 70% in the present simulation, parasite volume nears 80% of the original host cell volume. In the curves shown here the coupling factor was varied from 0.3 to 1.0 in steps of 0.1. All other parameters are as in Figures 2 and 3.*

Model predictions over the range of variation in parameter values.

Figure 8 shows the model predictions for five selected variables, plotted as a function of time post-invasion. The chosen range of variation for each parameter was based on experimental results when available or on outcomes of simulations consistent with observation. For instance, although single parasite volumes may remain within the 30 to 50 fl range, IRBCs are often seen with two viable parasites reaching segmentor stages, or with additional volume occupied by developmentally arrested parasites (Simpson et al., 1999). From the perspective relevant to the homeostasis of the host cell, it is the combined parasite volume that counts, hence the choice of coupling ratios spanning values from 0.3 to 1. The range of half-time values for NPP development and Hb ingestion is shown within ±1 standard deviation of the experimentally-reported means (Staines et al., 2001; Krugliak et al., 2002). Figure 8 shows only simulations with parameter values in which IRBC volumes remain below the spherical volume cells can attain within a maximally-stretched membrane, at which point they would lyse. This maximal volume is usually described as the critical haemolytic volume. Following Ponder (Ponder, 1948), the nominal CHV was set at a mean value of 1.7 times the original volume of the modelled cell. The immediate conclusion from gross comparisons between Figure 8A-C and Figure 8D-E is that whereas host cell water (Figure 8A), IRBC volume (relative to uninfected RBC volume, Figure 8B), and parasite volumes (Figure 8C) can vary over a very wide range and with large oscillations within the five homeostatic periods described for Figure 4 (Figure 8A-B), the predicted decline pattern in host cell Hb concentration remains remarkably uniform (Figure 8E). Therefore, the single novel and invariant prediction of the colloid-osmotic hypothesis is that the Hb concentration within the host cell has to become progressively reduced, regardless of parasite and IRBC volumes (Figure 8E).

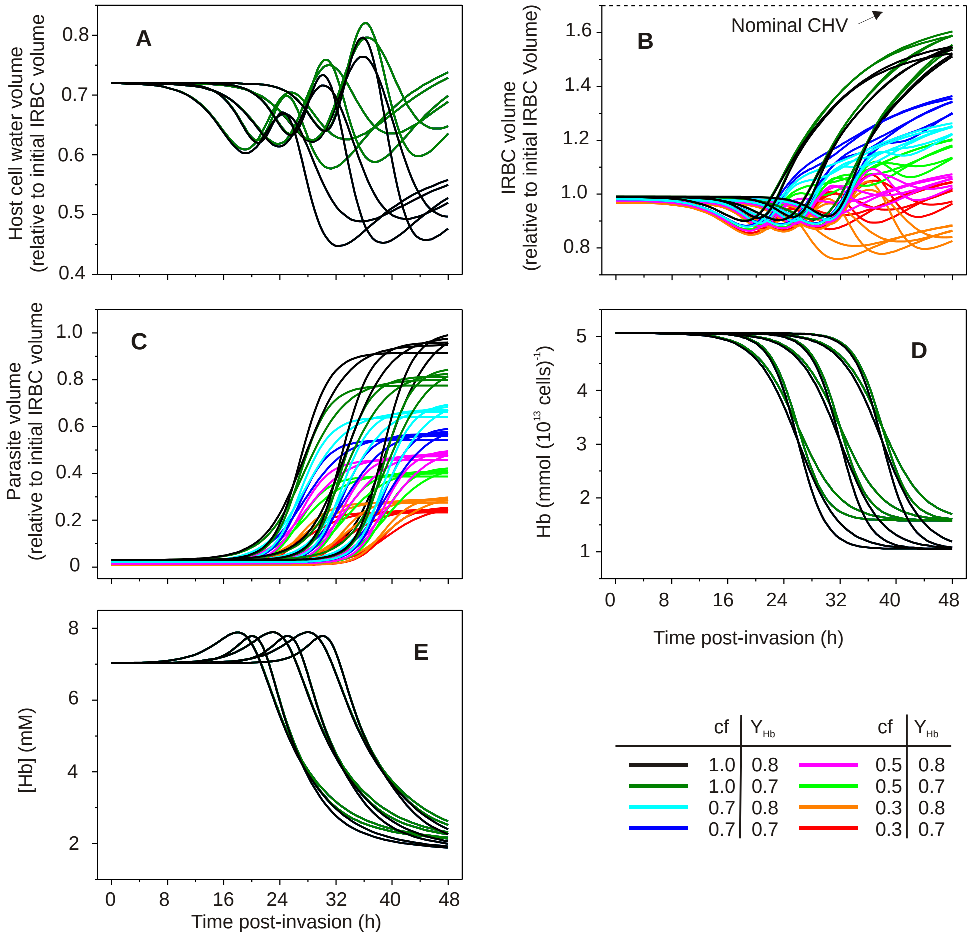

Figure 8: Effect of parameter variation on predicted changes as a function of time post-invasion. *The parameters varied and the range of values reported in the 48 curves of this figure are as follows: coupling factor (cf), 0.3, 0.5, 0.7 and 1; paired half-times of NPP development and Hb consumption (in h), 22-26, 27-32, and 32-38; slope-parameter of NPP and Hb curves (in h), 2 and 3; maximal Hb consumption (fraction of total initial Hb), 0.7 and 0.8. Panel A: host cell water volume, relative to initial IRBC volume; Panel B: IRBC volume, relative to initial volume. The broken line represents the nominal CHV based on a mean value of 1.7 reported for normal uninfected RBCs (Ponder, 1948); Panel C: relative*

parasite volume; Panel D: host cell Hb content, in mmol(10^{13} cells)$^{-1}$; Panel E: Hb concentration in host cell water, mM. Overlapping curves in Panels A, D and E conceal all the 48 curves within the 12 that can be discerned.

Discussion

The analysis of the homeostasis of *Pf* infected RBCs (Figures 4, 5, 6 and 8) provides a number of novel insights:

i) it identifies five distinct periods associated with dynamic changes in ionic driving gradients, in haemoglobin and ion contents, in ionic fluxes through NPPs and Na pump, and in water fluxes (Figures 4 and 5);

ii) it predicts specific stage-dependent variations in host cell pH (Figure 5C) and membrane potential (Figure 4D);

iii) it reveals a wide domain of homeostatic stability compatible with large variations in parasite and IRBC volumes throughout the asexual reproduction cycle of the parasite (Figure 8), and

iv) it demonstrates the homeostatic compatibility of an all-or-none mode of activation of NPPs (Figure 6). The graded and all-or-none alternatives for NPP activation in single IRBCs are relevant to ongoing controversies on whether NPPs represent upregulated endogenous pathways of the RBC membrane or whether they are parasite-induced insertions (Desai et al., 2000; Bouyer et al., 2007; Staines et al., 2007). Upregulation, as recently suggested (Bouyer et al., 2007), could explain better an all-or-none modality by a developmental-stage controlled release of a NPP-activation factor within each IRBC. However, the all-or-none alternative remains untested experimentally. One possible approach would be to measure NPP-mediated conductance in stage-segregated IRBCs using the cell-attached patch clamp configuration. Graded NPP development predicts a clear trend of increasing conductance with parasite developmental stage whereas all-or-none predicts similar large NPP conductances at all developmental stages whenever detected. We now discuss some of the issues arising from this analysis.

We consider next how experimental results in the literature compare with our model predictions. In Figure 9, experimental measurements of the five selected variables reported in Figure 8 are shown as rectangles over the grey silhouettes of the variable ranges in Figure 8.

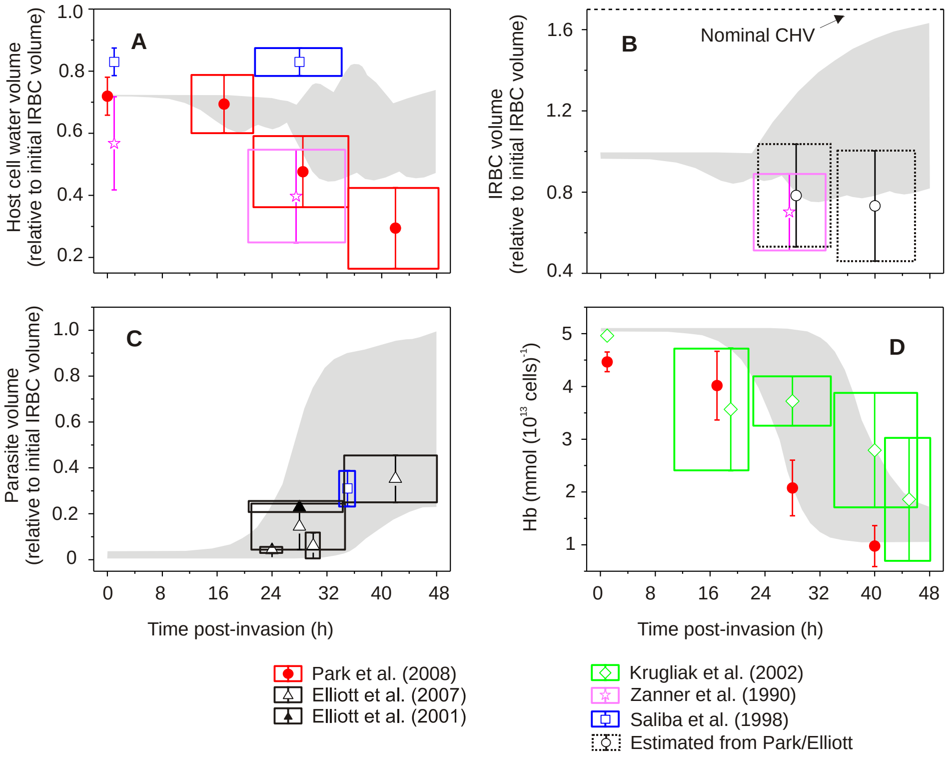

Figure 9: Comparison between predicted and measured variable values. *Measured values were obtained from the references listed. The ranges of predicted variable values shown in Figure 8 are redrawn as grey silhouettes; the experimental data is plotted as boxes. On the ordinate the box indicates the reported statistical errors; on the time axis the box width is arbitrarily set to 26 h – 34 h for trophozoites, 36 h – 46 h for schizonts,*

and 42 h – 48 h for segmentors using the period assignations in the original papers. Data for uninfected cells is shown at time = 0, where available. Symbols indicate the source of the data, as follows: closed circles - Park et al. (Park et al., 2008); open and closed triangles - Elliott et al. (Elliott et al., 2001; Elliott et al., 2008); open diamonds – Krugliak et al. (Krugliak et al., 2002); open stars – Zanner et al.(Zanner et al., 1990); open squares – Saliba et al. (Saliba et al., 1998). Panel A: host cell water volume, relative to initial IRBC volume; Panel B: IRBC volume, relative to initial volume; Panel C: relative parasite volume; Panel D: host cell Hb content, in mmol(10^{13} *cells)*$^{-1}$*. Data in panel B were modified from the original references to provide plausible estimates in the absence of direct measurements. IRBC volumes in panel B (dotted lines) were estimated from data in Park et al. (Park et al., 2008) and Elliot et al. (Elliott et al., 2008) by adding the cytosol volume from Park et al. (Park et al., 2008) to the parasite volume from Elliot et al. (Elliott et al., 2008).*

Despite the large variability in the experimental results, it is clear that they fall within the low range of values for host cell water (Figure 9A), IRBC volume (Figure 9B), and parasite volume (Figure 9C) for single infections (Zanner et al., 1990; Saliba et al., 1998; Elliott et al., 2001). The haemoglobin content measurements show a declining pattern covering the full range of the values encoded in the model (Figure 9D).

Do the large variations in parasite and host cell volumes explored with the model and also apparent in the experimental measurements (Figure 9) reflect true IRBC polymorphisms or merely error margins? IRBC polymorphisms are evident in relation to a number of characteristics which can be easily observed and recorded in live cultures: single or multiple invasion, developmental and viability differences among parasites in multiple invasions, IRBC shapes and volumes, parasite sizes and shapes, haemozoin particle content, aggregation state of haemozoin crystals, number of merozoites contained and released, etc.

Many of these variations are observed in highly synchronized populations and cannot be attributed simply to differences in developmental stage of the parasite, or to viability state of the IRBCs. It is therefore plausible that the domain of stable homeostatic solutions predicted by the model (Figure 8) does indeed reflect, at least in part, true homeostatic polymorphisms of IRBCs. If so, parasite, host and IRBC volumes may vary within wide margins from cell to cell without necessarily compromising the osmotic stability of the IRBC. This, however, questions the fundamental tenet of the colloid-osmotic hypothesis, that excess Hb consumption is necessary to prevent premature IRBC lysis.

The problem can be clearly illustrated with an example. Let us consider an IRBC whose volume remains near a relative cell volume of 1 throughout the asexual reproduction cycle, as in many of the curves shown in Figure 8B, and as documented experimentally (Saliba et al., 1998; Elliott et al., 2008; Park et al., 2008). If the critical haemolytic volume remains set at 1.7 times the initial RBC volume, as originally assumed based on data from uninfected RBCs (Ponder, 1948), model simulations indicate that ~ 20% Hb consumption would be enough to prevent the premature lysis of a cell with relative volume around 1. So, for such a cell, excess Hb consumption would appear irrelevant for lysis prevention. But the available evidence overwhelmingly supports the view that Hb is consumed in large excess in all viable IRBCs. It follows that reduced colloid-osmosis may not be the main reason for excess Hb consumption, at least not in all instances. However, as discussed next, the conundrum here rests with the rigid attribution of a CHV of 1.7 in the model simulations, not with the basic understanding of IRBC homeostasis provided by the model.

Previous results from osmotic fragility studies in IRBCs showed that the osmotic fragility of RBCs infected with mature trophozoite- and schizont-stage parasites is substantially increased relative to IRBCs with ring-stage parasites or to uninfected cohorts (Lew et al., 2003; Lew et al., 2004). If the actual volume of at least some IRBCs harbouring mature parasites remains low, then for the osmotic fragility to be increased their CHV has to be somehow reduced.

How can this occur? The CHV of each RBC depends critically on membrane area (Ponder, 1948; Svetina, 1982; Lew et al., 1995). If membrane area is reduced by infection, the CHV will also be reduced. The relation between volume (V) and area (A) in a sphere is given by $V = A^{3/2}/(6\pi^{1/2})$. Therefore, since the ratio of maximal volumes (V_1, V_2) of two cells with different surface areas (A_1, A_2) is $V_1/V_2 = (A_1/ A_2)^{1.5}$, a fractional decrease in area will propagate to a fractional decrease in volume to the power of 1.5, stressing the magnified effect of effective membrane area reductions on CHV. Early results in the literature report opposing claims in relation to membrane area changes in infected IRBCs: population estimates report substantial reductions (Zanner et al., 1990) whereas single cell measurements suggested no change (Nash et al., 1989). Recent movies by Glushakova et al., (Glushakova et al., 2005) show infected cells about to rupture whose near spherical diameter is less than 80% that of surrounding uninfected discocytes indicating reduced membrane area. Considering, in addition, that the membrane geometry and fluid properties of Pf-infected RBCs become progressively altered by knobs and increased rigidity (Paulitschke and Nash, 1993; Paulitschke et al., 1994; Paulitschke et al., 1995; Glenister et al., 2002; Suresh et al., 2005; Glenister et al., 2009), the increased osmotic fragility may be compounded by an increased lytic vulnerability to volume expansion, resulting from reductions in membrane area, in the capacity to effect a normal expansion of the full membrane area before lytic rupture, or both.

The increase in the osmotic fragility of IRBCs reflects a progressive haemolytic vulnerability of *Pf*-infected RBCs to volume expansion by fluid gains. This shows that IRBCs become progressively closer to their effective CHV as the parasite matures, regardless of their actual volume levels. Although the contributions of membrane area loss and other factors to this haemolytic vulnerability remain to be elucidated, excess Hb consumption retains its credential as a general protection mechanism for IRBCs of all volumes, by preventing excessive rates of fluid gain. This mechanism depends critically on the prediction illustrated in Figures 5B that the Hb concentration must become progressively reduced in all IRBCs, regardless of the specific volume evolution of each IRBC.

In conclusion: the original formulation of the colloid-osmotic hypothesis, using a coupling coefficient of one, predicted that IRBCs would swell close to a CHV level taken as the mean value for uninfected RBCs, premature rupture being prevented by the reduced Hb concentration. Simulations with coupling coefficient values below 0.7 deliver more realistic IRBC volume estimates (Figures 7B and 9B), but experimental results indicate that the progressive proximity of IRBCs to a reduced CHV is retained. Thus, whatever the reason for CHV proximity, reduction in Hb concentration remains essential for preventing rapid fluid gains leading to premature IRBC lysis (Mauritz et al., 2009).

Chapter 3: Measurement of stage-related changes in host haemoglobin concentration by resonance energy transfer

Motivation

A reduction in host cell haemoglobin concentration is the critical prediction of the homeostatic model described in Chapter 2. It was well known that the haemoglobin *content* of the host cell is reduced by parasitic consumption, but its *concentration* ([Hb]) depends furthermore on the water volume of the host cell. The following two chapters present two independent methods to measure intracellular [Hb]. According to the model predictions, the time from 32 to 40 h post invasion should be a period of mature parasite growth with a high probability of detecting substantial reductions in Hb concentration within the host cell cytoplasm (Figure 8E), from normal values of about 7 mM in uninfected or ring-stage infected red cells down to ~4 mM in cells with mid-age trophozoites and 2-3 mM in schizont-containing cells, regardless of the IRBC volume (Figure 8B).

Preliminary indirect estimates of [Hb] were performed with transmision electron microscopy (Lew and Hockaday, 1999; Dondorp et al., 2004). The electron densities of the image-sections were thought to be proportional to [Hb]. But the attempt to calibrate the electron density against different, known [Hb] levels in osmotically swollen erythrocytes yielded inconsistent results and rendered the technique inapplicable.

An alternative approach for testing the colloid-osmotic hypothesis is to detect increased osmotic fragility and premature IRBC lysis when Hb digestion is prevented or reduced with the use of protease inhibitors. In early (Lew et al., 2004) and recent attempts (Naughton et al., 2010) it proved impossible to block Hb consumption without impairing parasite development at the same time. In these conditions, failure to detect increased lysis or osmotic fragility has no relevance as a test of the colloidosmotic hypothesis because the IRBCs never reach the stage of osmotic compromise.

Mapping the light absorption of Hb within the infected RBC appeared a feasible alternative for [Hb] quantification. However, a number of drawbacks appeared to limit the applicability of this method. The need for simultaneous estimation of cell thickness at each pixel together with the need to discriminate unambiguously between RBC and *Pf* compartments with sufficient resolution makes this approach less practicable. At this time in the malaria project, it was decided to move to electron probe X-ray microanalysis (EPXMA) for mapping the haemoglobin concentration (Chapter 4). It was thought to be more prospective for yielding reliable results, because it is a well established, classical technique. Light microscopy was to be used for quantifying the IRBC volumes. The author was assigned to work on the X-ray microanalysis, while assisting in the microscopy work referred to Dr Alessandro Esposito. In the course of the volumetric microscopy work a second method of quantifying [Hb] was developed by Dr Esposito. Because of its relevance to verify the colloid-osmotic hypothesis for the homeostasis of the malaria infected erythrocyte, these results are presented next. Most of the actual experiments described here and in Chapter 5 were performed in parallel sessions by Dr Esposito and the author (measuring [Hb] and volumes on two different microscopes), to make the most economic use of the parasite cultures, which are time and cost intensive to grow and sustain.

Introduction

A quantitative method for the determination of Hb concentration in live parasitized blood cells was envisaged during measurements of IRBC volume in cells loaded with the dye calceine-AM to obtain improved contrast for confocal sectioning and volume estimations (see Chapter 5). While observing RBC samples under the microscope that was accidentally left dehydrating, frequent cell photolysis occurred, induced by the mercury lamp. Surprisingly, lysis events resulted in bright flashes of fluorescence. This initially puzzling phenomenon was recognised to stem from the dequenching of the calcein fluorescence upon cell lysis. Because of the spectral characteristics of the haeme chromophore (Horecker, 1943), haemoglobin is a powerful quencher of any fluorophore with fluorescence emission spectra peaking below 600 nm. Calculations show that Hb molecular crowding is so high that any fluorophore in the cytosol would only be, on average, a few nanometers away from multiple haeme moieties at any given time (see Appendix B). This causes non-radiative Förster resonance energy transfer (FRET) (Förster, 1948) from calcein to the neighbouring Hb molecules, as the absorption spectrum of Hb features significant overlap with the calcein emission spectrum. On lysis, the mean distance between calcein and Hb molecules increases rapidly, causing a sudden increase of fluorescence as calcein becomes dequenched. FRET occurs when an excited donor molecule is close (typically less than 10 nm) to an acceptor molecule with an efficiency that decays with the inverse of the 6th power of the distance between donor and acceptor (Lakowicz, 1999) (see Appendix B). Our observations suggested that the decrease in fluorescence lifetime due to FRET could be used to quantify Hb molecular crowding and therefore to map Hb concentration in live blood cells.

The fluorescence emmission lifetime of fluorophores, calcein in this case, can be measured by combining the high spatial resolution of a confocal laser scanning microscope with the high lifetime resolution of time-correlated single photon counting (TCSPC). High spatial resolution is needed to discriminate between host- and parasite compartments. High fluorescence lifetime resolution is necessary to measure the very fast decays observed when calcein is quenched by Hb over the relevant range of haemoglobin concentrations (2-7 mM).

Time-Correlated Single Photon Counting

Time-correlated single photon counting can be used for fluorescence lifetime imaging by measuring the arrival time of the first photon emitted after a short (fs or ps) excitation pulse. Figure 10A illustrates the principle of TCSPC imaging; the upper left part of the panel shows the time measurement. Typically, a photomultiplier tube is used for detection. The time measurement is started by a constant fraction discriminator (CFD), which triggers at a constant fraction of the pulse amplitude of the detector, thus avoiding pulse-height induced timing jitter. The CFD toggles a time-to-amplitude converter (TAC), which is read-out and reset with the following excitation pulse. Like a capacitor, the TAC builds up a voltage over time (charging), that accurately reflects the time between the triggering events. This configuration is called “reversed start-stop” and it avoids resetting the electronics after every excitation pulse (only when a photon arrives the acquisition is triggered). It enables higher repetition rates of the excitation source and thus minimizes pile-up (the undesired effect of several photons arriving in the same signal period). (Becker et al., 2004; Becker, 2005; Becker, 2010). The arrival time of each photon is then recorded in the memory of the acquisition electronics and assigned to an image pixel, which will correspond to a particular position of the galvanometric scanners of the confocal microscope. Typical fluorophores exhibit mono- or multi-exponential fluorescence decays that can be deduced by plotting histograms of the arrival times of many photons collected after the pulsed excitation of the sample with a high repetition rate laser. Figure 10B illustrates how FLIM data is adressed after accumulating numerous photons.

The information is stored as a 2D spatial image of the sample, but each image pixel contains a photon arrival time distribution. From these arrival time distributions, the fluorescence lifetime can be estimated in each image pixel.

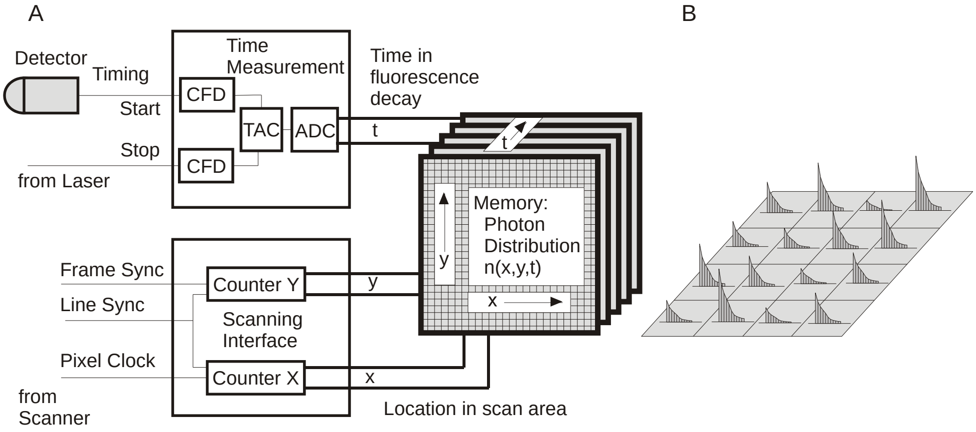

Figure 10: Schematics of TCSPC Imaging, *scan sync in mode. (A) The recorded photon arrival time at the light detector is encoded with the spatial information from the microscope scanners and stored in memory. The time measurement is performed by a constant fraction discriminator (CFD), which triggers at a constant fraction of the pulse amplitude of the detector, thus avoiding pulse-height induced timing jitter. The time-to-amplitude converter (TAC) generates an output signal proportional to the time between the start and the stop pulse. Conventional TACs use a switched current source charging a capacitor. The start pulse switches the current on, the stop pulse off. If the current in the start-stop interval is constant, the final voltage at the capacitor represents the time between start and stop. (B) This acquisiton results in an spatial array of photon distributions, from which the fluorescence lifetimes (decay constants) can be estimated and visualised in a fluorescence lifetime image (see Figure 15 and 16 for examples). Adapted from (Becker, 2010)*

Materials and methods

Chemicals. All chemicals were analytical reagent quality. Calcein-AM was from Invitrogen Ltd., Paisley, UK. Plasmagel was from Bellon, Neuilly Sur Seine, France. All common salts, EGTA, Hepes, glucose, inosine, pyruvate, DMSO, RPMI 1640 medium, gentamicin sulphate, glutamine, free calcein, triton X-100 and bovine serum albumin (BSA) were from Sigma-Aldrich Company Ltd., Gillingham, UK. Human blood and serum used in cultures were from the National Blood Service (UK).

Cultures. The culturing of parasites here and in the following experiments was performed by Dr. Teresa Tiffert and Rachel Seear, who are gratefully acknowledged here. Two *P. falciparum* clones (ITO4 and A4BC6, kindly provided by B.C. Elford, Institute of Molecular Medicine, Oxford, UK) (Berendt et al., 1989) were cultured separately in human erythrocytes under a low-oxygen atmosphere by standard methods (Trager and Jensen, 1976). The culture medium was RPMI 1640 supplemented with 40 mM HEPES, 25 mg/l gentamicin sulphate, 10 mM d-glucose, 2 mM glutamine and 8.5 % (vol/vol) pooled human serum. Parasite development and replication were assessed in cultures by microscopic examination of Giemsa-stained thin blood smears, as reported before (Tiffert et al., 2000). Parasitised RBCs were harvested from cultures immediately prior to experimentation.

Solutions. Solution *A* contained (in mM): NaCl, 145; KCl, 3; Na-HEPES (pH 7.5 at 37^{o} C), 10; $MgCl_2$, 0.15. Solution *AE*: as *A* plus 0.1 mM Na-EGTA. Solution *AIP*: as *A* plus 5 mM inosine and 5 mM pyruvate. Calcein-AM was used as a stock solution of 0.7 mM in DMSO. The stock solution of free calcein was 10 mM in DMSO.

Calcein loading. Cell samples from malaria cultures were washed once in *AIP*, resuspended at 2% haematocrit (Hct) in the same medium and incubated at 37 °C for 20 min with calcein-AM at a concentration of about 120 μmol per litre RBCs, assuming 100 % free calcein incorporation into the cells. Inosine in the medium was used as a glycolytic substrate and pyruvate to bypass the glycolytic block generated by the release of formaldehyde during the breakdown of the acetoxymethyl ester that remains fully retained by the cells (Tiffert et al., 1984; Garcia-Sancho, 1985). After incubation, the cells were washed twice by centrifugation and resuspension in *AIP*; ~$4\cdot10^6$ cells were then transferred to a chamber with glass bottom coated with poly-L-lysine (#1.0, MatTek Corp., Ashland, MA, USA) and further incubated at 37 °C for 60 min to allow adherence to the coverslip. The supernatant was then exchanged with fresh solution *AE* supplemented with 1 % BSA and the chamber transferred to the stage microscope for imaging.

Preparation of lysate for [Hb] calibrations. Venous blood (5-10 ml) from healthy volunteers was drawn, after written consent, into syringes containing EGTA. The cells were immediately spun (1500 g, 10 min) to separate the plasma, washed twice by centrifugation (1500 g, 5 min) and resuspension in 10 ml of solution *AE* to remove Ca^{2+} loosely bound to the cells (Harrison and Long, 1968), and then washed two more times in solution *A* to remove EGTA from the medium. Supernatant and buffy coat were removed after each centrifugation. After the washes, the cells were packed by centrifugation (11000 g, 3 min) and lysed by addition of Triton X-100 (1% vol/vol). The original [Hb] in the lysate was estimated by optical absorption at 415 nm in diluted samples. [Hb] in the concentrated lysate was in the range of 6.5 to 7.0 mM. Suitable Hb concentrations for calibration were obtained by diluting the concentrated lysate with solution *A*. Free calcein was added to the Hb samples from the 10 mM stock in DMSO to render the indicated final calcein concentrations. Further tests of the reliability of [Hb] estimates in intact cells were carried out on calcein-loaded RBCs exposed to hypotonic media to vary their [Hb]. Hypotonic media were prepared in the pre-lytic 0.6 to 1 range of relative tonicities by dilution of solution *A* with double distilled water.

Microscopy. Fluorescence lifetime imaging microscopy was performed with the use of a setup developed in the Laser Analytics Group, Department of Chemical Engineering and Biotechnology at Cambridge University. It is based on a confocal microscope Olympus FluoView 300 (Olympus UK Ltd, Watford, UK) coupled with a supercontinuum laser source (SC450, Fianium, Southampton, UK) (Frank et al., 2007). The SC450 provides ~5 ps pulses at a repetition rate of 40 MHz, suitable for TCSPC. The system was upgraded with a PMC-100-20 photomultiplier tube and an acquisition board SPC-830, both by Becker & Hickl GmbH (Berlin, Germany). Calcein was excited at 485 nm and the fluorescence emission was collected over the 520-570 nm range. TCSPC data was analysed with SPCImage software (Becker & Hickl GmbH) with a three-exponential decay and scatter light fitting to provide the average lifetime shown in Figures 12A, 13, 15B and 16. Average count rates were kept below 10^5 counts per second in order to avoid pulse pile-up. All images were acquired at room temperature with an oil immersion 63x objective and a large (300 μm) pinhole in order to collect enough photons during the 60 s acquisition time.

Data analysis. The fluorescence images were segmented in the phasor space by performing a sine (A) and cosine (B) transformation of the TCSPC data (Clayton et al., 2004; Digman et al., 2007). The AB-plots were generated by a Matlab (The MathWorks Inc., Novi, MI, USA) routine programmed by Alessandro Esposito (Laser Analytics Group, Cambridge University). Photons from each segmented region were binned together and the following equation was fitted by iterative reconvolution (Barber et al., 2005):

$$I(t) = \int d\zeta \cdot \left\{ a \exp\left(-\frac{t}{\tau}\right) \left[c + \exp\left(-\frac{[Hb]}{[Hb]_0} \sqrt{\frac{t}{\tau}} \right) \right] + s \exp\left(-\frac{t}{\tau_s}\right) \right\} \cdot$$

$$\cdot\, IRF(t - \zeta, w, t_0) + b \qquad (1)$$

This represents the decay of calcein starting at t_0, quenched by freely diffusing haemoglobin in the presence of unquenched donor (of lifetime τ) and scatter ($\tau_S = 10$ ps), convolved with the instrument response function (*IRF*) and in the presence of background (b). a, b, c and s are absolute amplitudes of the different components. The best fit was found minimizing the cost function proposed by Awaya (Awaya, 1979) in order to minimize biases generated by the presence of data bins with low counts. The molecular fraction of quenched calcein ($f_{CA\text{-}Hb}$) can be inferred by the following equation:

$$f_{CA-Hb} = 1 - c \cdot \left\{ 1 + c - \sqrt{\pi} X \exp\left(X^2\right) \operatorname{erfc}(X) \right\}^{-1}, \qquad (2)$$

where $X = [\mathrm{Hb}] \cdot [\mathrm{Hb}]_0^{-1}$ represents the haemoglobin concentration and the slope from a linear fit of equation 1 (see Figure 14). Additional information on FRET induced by molecular crowding and on the data analysis is provided in Appendix B and in the literature (Förster, 1948; Bennett, 1964; Lakowicz, 1999; Beghetto et al., 2000; Wouters et al., 2001).

Numerical computation. The Förster radius of calcein-haeme chromophores was computed by numerical integration of the fluorescence emission spectrum of calcein and the corrected tabulated absorption spectrum of oxy-haemoglobin obtained from Invitrogen Ltd. (http://probes.invitrogen.com) and the Oregon Medical Laser Center (http://omlc.ogi.edu), respectively; numerical integrations were performed with Mathematica (Wolfram Research Europe Ltd., Long Hanborough, UK).

Results

Quenching of calcein via FRET. At the so called Förster distance (R_0, see Figure 11A), the energy transferred from donor to acceptor is 50 %. The Förster distance depends on the spectral properties of donor and acceptor (Figure 11B) and it was estimated to be ~ 4.1 nm for the calcein-haeme pair. This confirms that at physiological haeme concentrations (~28 mM; 1 Hb molecule = 4 haeme moieties) there is always a significant probability to have acceptors in close proximity (~R_0) of a donor. The critical haemoglobin concentration, i.e., the concentration at which 76 % of energy is transferred (Lakowicz, 1999), can be thus estimated to be about 1.7 mM (see Appendix B).

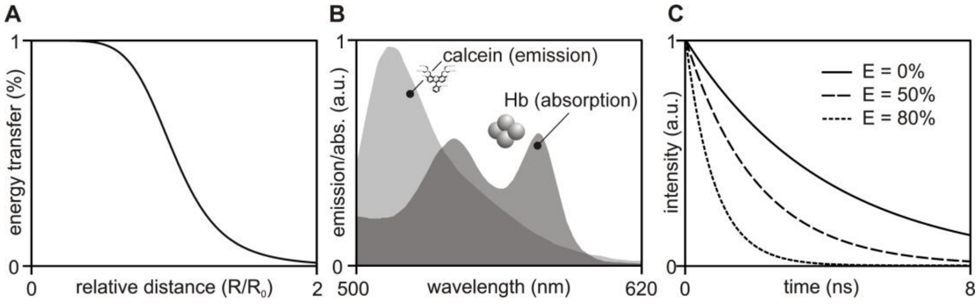

Figure 11. Fluorescence lifetime and FRET*. (A) Curve illustrating the strong dependence of energy transfer efficiency on the relative distance between donor and acceptor fluorophores. (B) Spectral overlap between the emission spectrum of a donor and the absorption spectrum of an acceptor fluorophore such as calcein and haeme on which FRET depends (abs., absorption; a.u., arbitrary units). (C) Predicted fluorescence decay of a fluorophore such as calcein, in the presence of 0 % (solid line), 50 % and 80 % (dashed lines) FRET efficiency.*

FRET decreases the fluorescence lifetime of a donor fluorophore proportionally to the FRET efficiency, as illustrated in Figure 11C, and therefore it is feasible that FRET induced by molecular crowding can be used to map [Hb] in living cells. For calibration, this dependency was initially tested with dilute Hb solutions.

Figure 12 shows fluorescence images of lysates in the presence of calcein (100 μM) and their representation as phasor plots. The fluorescence decay *I(t)* in a given pixel with index *i* and *j* is transformed to AB-plot coordinates A and B given by:

$$A_{i,j} = \int_0^\infty I_{i,j}\,(t)\cos(\omega t)\mathrm{d}t \Big/ \int_0^\infty I_{i,j}\,(t)\,\mathrm{d}t \qquad (3)$$

$$B_{i,j} = \int_0^\infty I_{i,j}\,(t)\sin(\omega t)\mathrm{d}t \Big/ \int_0^\infty I_{i,j}\,(t)\,\mathrm{d}t \qquad (4)$$

where ω is the laser repetition angular frequency (Clayton et al., 2004; Digman et al., 2007). In this representation molecules with a similar lifetime will cluster close to each other, regardless of their spatial location. This facilitates data analyses, as regions of interest (similar lifetimes often meaning similar molecular properties) can be selected in the phasor plot by the experimenter and then highlighted in the real, spatial microscope image (compare also Figure 17). Lysate dilutions rendered Hb concentrations between 0 and 6 mM. The average fluorescence lifetimes are shown in Figure 13A: the fluorescence lifetime of calcein in the absence of haemoglobin was 4.08 ± 0.01 ns and the [Hb]-dependent quenching of calcein appeared to be consistent with the proposed model (eq. S48).

Calcein is known to exhibit self-quenching at high (millimolar) concentrations (Hamann et al., 2002), and it has also been suggested that self-quenching can occur at concentrations as low as 3 μM (Roberts et al., 2003). Self-quenching may result in either a decrease or increase in fluorescence lifetime, and could become a serious impediment for [Hb] measurements. It was therefore important to test for possible self-quenching effects within the range of calcein concentrations intended for intact cell measurements (< 150 µM). *In vitro* tests showed that the maximal variation in calcein fluorescence lifetime within the 10-500 µM concentration range was ~70 ps (data not shown) in phosphate buffer saline, growth medium and solution *A*.

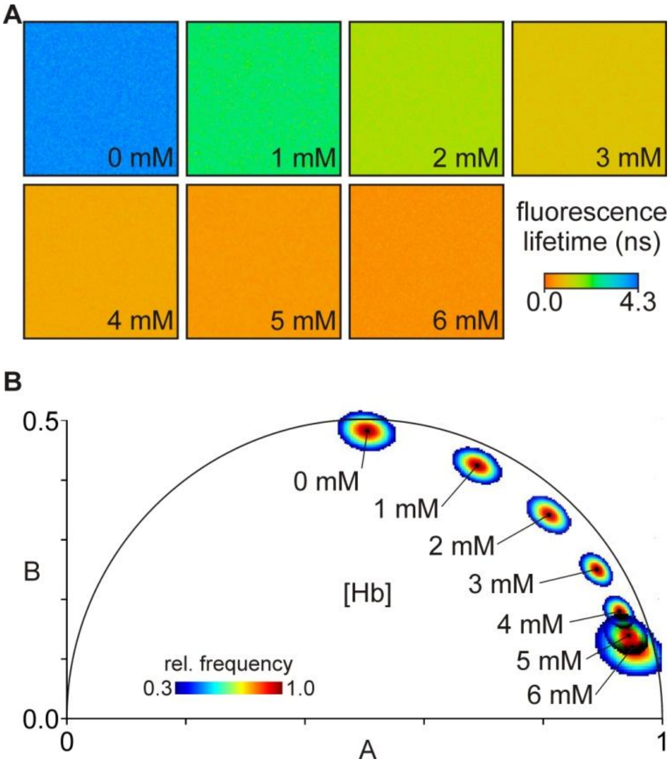

Figure 12. Quenching of calcein by haemoglobin. *A) Images show the decrease in fluorescence lifetime of calcein (100 µM) with haemoglobin concentration (0 to 6 mM) in RBC lysates. Fluorescence lifetimes are easily distinguishable in the 0-4 mM range of [Hb]. B) Same calibration data are represented in the phasor space. The centroids of phasor distributions are also shown in Figure 17 (circles). Rel. frequency: relative frequency.*

Figure 13B shows that no significant de-quenching of calcein occurred at decreasing calcein concentrations (150 µM, 100 µM and 50 µM). Therefore, calcein can be used for the quantitative detection of haemoglobin concentration within the cytosol domain of infected red cells. The calibration data shown in Figure 12 was then fitted with equation 1. Figure 14 shows the relation between estimated and measured [Hb]. The slope rendered $[\mathrm{Hb}]_0 = 1.70 \pm 0.02$ mM, a value in good agreement with the predicted one.

The results so far confirm that the prime mechanism for fluorescence quenching of calcein loaded into RBCs is dynamic quenching mediated by FRET via the non-fluorescent haeme chromophore. The use of FRET induced by haemoglobin molecular crowding may thus be applied to report [Hb]. The lack of specificity of this mechanism may explain the quenching observed with other fluorophores emitting below 600 nm such as Fura-2, Indo-1 and Fluo-4 (Lew et al., 1993; Kaestner et al., 2006).

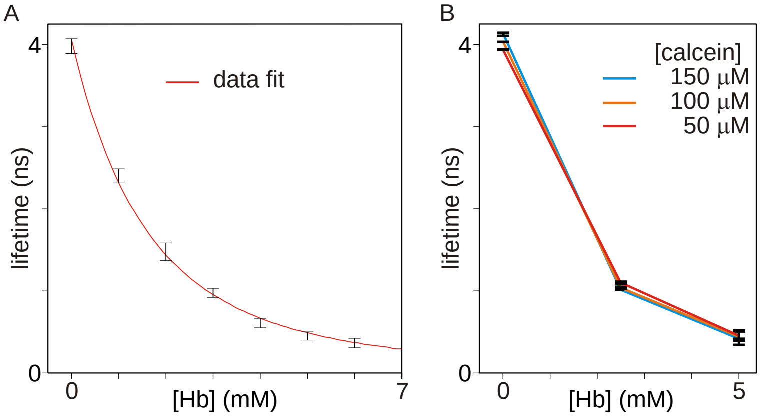

Figure 13. Quenching of calcein at different calcein and haemoglobin concentrations: *(A) Average fluorescence lifetime* versus *[Hb] (mean of three experiments). Experimental values were fitted by equation S52. (B) Hb-dependent quenching of calcein at different calcein concentrations (50, 100 and 150 µM).*

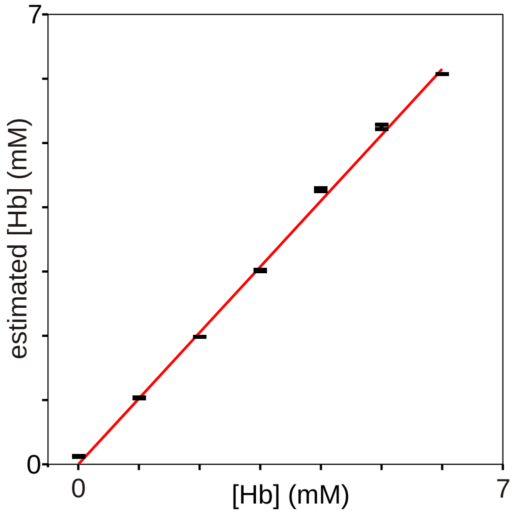

Figure 14. Measurement of [Hb]$_0$. *[Hb], estimated from Equation 1, is plotted as a function of measured [Hb] (ordinate intersection set to zero). The parameter [Hb]$_0$ was estimated from the slope of the linear fit, as explained in the text. Bars are standard deviation from measurements performed in triplicates.*

Lifetime imaging of normal, uninfected red blood cells. Figure 15 shows a low magnification image of red blood cells acquired by TCSPC. The high physiological concentration of haemoglobin renders the method only moderately sensitive to [Hb] variations near physiological conditions. Normal RBCs (Figure 15A-B) exhibited an average fluorescence decay time of (mean ± SD) 250 ± 20 ps (n = 37) corresponding to a [Hb] of 6.3 ± 0.3 mM. When the RBCs were swollen in solutions of lower relative tonicity (RT), fluorescence lifetime changes were clearly detected (Figure 15C). At RTs of 0.8 and 0.6, the fluorescence lifetime of calcein increased to 280 ± 20 ps (n = 38) and 380 ± 40 ps (n = 30), respectively, equivalent to Hb concentrations of 5.9 ± 0.3 mM and 4.8 ± 0.3 mM. At lower RTs significant lysis interfered with the [Hb] estimates and could not be pursued.

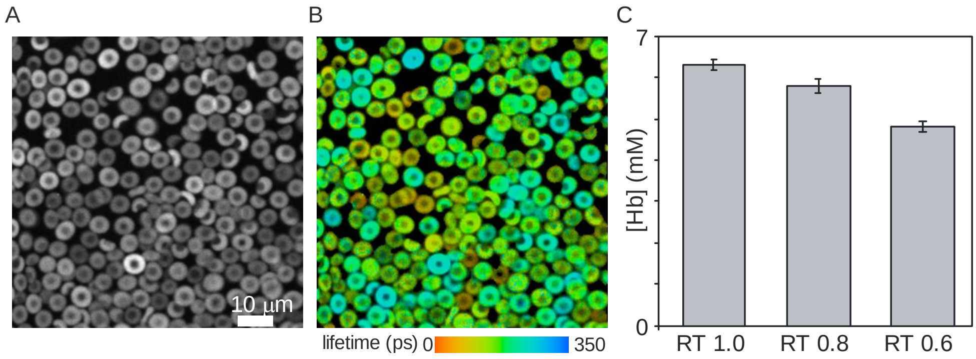

Figure 15. Fluorescence lifetime imaging of calcein loaded red blood cells. *(*A*) Fluorescence emission (520-570 nm). (*B*) Fluorescence lifetime of calcein showing a decrease from about 4 ns at zero [Hb] down to 250 ps in intact uninfected RBCs. Note the variation in fluorescence intensity and fluorescence lifetime among the cells. These reflect the normal distribution of incorporated calcein and [Hb] in red cells (Lew et al., 1993; Lew et al., 1995). (C) [Hb] measured by fluorescence lifetime in RBCs whose [Hb] was reduced by equilibration in hypotonic media (RT: relative tonicity).*

Lifetime imaging of parasitized RBCs. Figure 16 shows representative images of infected and non-infected RBCs. Non-infected cells showed homogeneous fluorescence intensity and fluorescence lifetime. The fluorescence lifetime of calcein averaged over the uninfected cells in these samples was 250 ± 12 ps (Figure 16B, right) and 250 ± 10 ps (Figure 16E, right).

In the cytoplasm of infected cells the fluorescence lifetime of calcein ranged from 290 ± 20 ps (Figure 16B, left) for a RBC containing a parasite at ring stage to 590 ± 13 ps (Figure 16 E, left) and 1050 ± 60 ns (Figure 14 G) for a young and late stage trophozoite / early schizont, respectively.

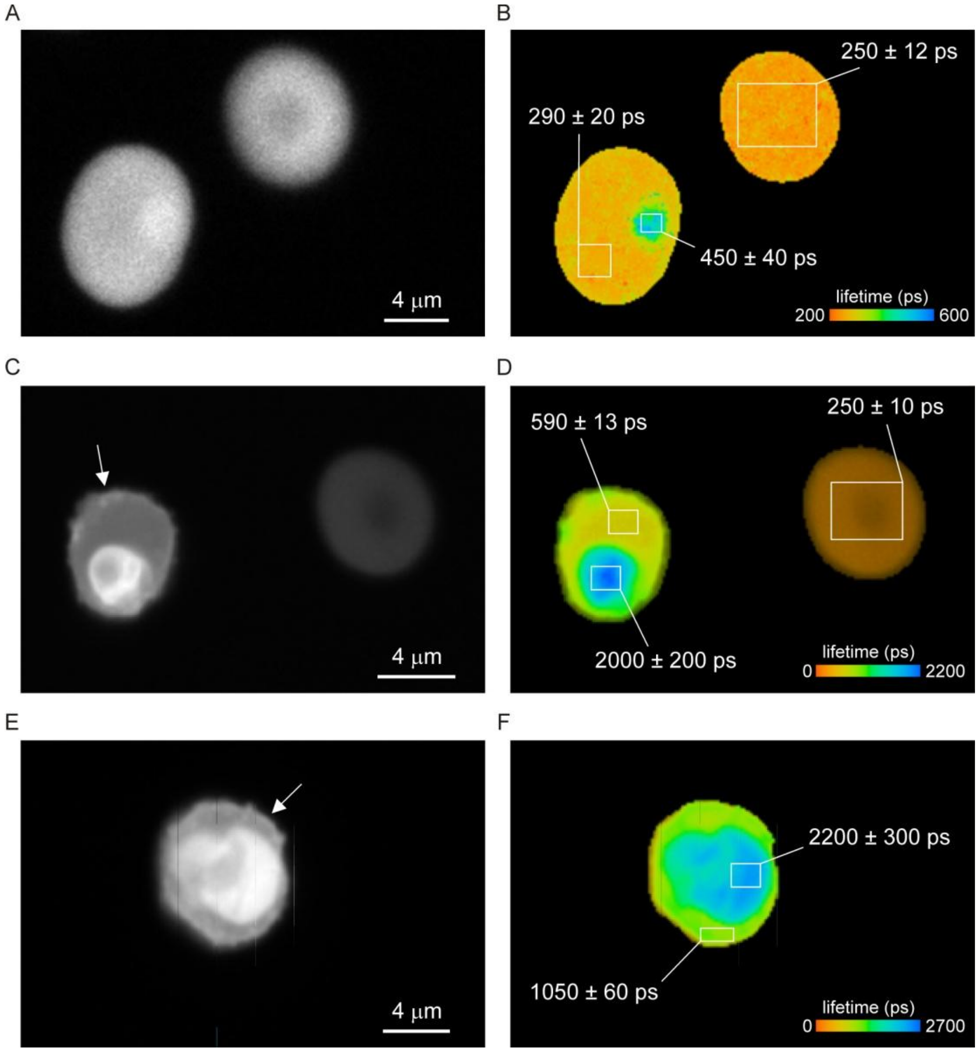

***Figure 16. Lifetime images of infected red blood cells**, Panels A, C and E show fluorescence intensity images of an uninfected RBC (A and C, right), a ring stage (A, left), a young trophozoite (C, left) and a mature trophozoite/early schizont (E). Arrows in panel C and E indicate the appearance of a bright edge in the IRBCs. The correspondent fluorescence lifetime images (B, D and F) reveal a significant increase in fluorescent lifetime in the host cytosol of infected cells relative to that in uninfected RBCs reflecting a decreased haemoglobin concentration.*

In order to discriminate between regions of the RBC where the parasite is located and the remaining cytoplasm, the lifetime images were mapped to the phasor space resulting in AB-plots (Figure 17) where pixels with similar lifetimes cluster together (Clayton et al., 2004; Digman et al., 2007; Wouters and Esposito, 2008).

These clusters can be selected and the corresponding regions segmented. Uninfected RBCs always exhibited single clusters (Figure 17A) with occasional tails that converged to the fluorescence background (data not shown). All infected cells exhibited two or three clusters with the one at lower lifetimes corresponding to the RBC cytoplasm. Figure 17B shows an IRBC containing a ring-stage parasite; here, the parasite-related cluster (ii) is less defined (note the different scale) because of the small region occupied by the ring relative to the RBC cytoplasm (i). IRBCs containing early trophozoites (Figure 17C) or late trophozoites / early schizonts (Figure 17D) typically exhibit three clusters corresponding to (i) RBC cytoplasm, (ii) the parasite and (iii) two other regions within the IRBC, one immediately encircling the parasite and the other forming a peripheral zone beneath the IRBC plasma membrane. Late trophozoites / early schizonts (Figure 8D) often exhibit only two regions with comparatively low [Hb] estimates. The cytosolic cluster with the highest [Hb] in each cell was used to estimate cytosolic [Hb].

Haemoglobin concentration in parasitized cells. The average fluorescence lifetimes of uninfected cohorts was 270 ± 30 ps (*n* = 45), and of IRBCs with ring-stage parasites was 267 ± 13 ps (*n* = 10). There was no statistical difference between these two groups. The distribution of fluorescence lifetimes and corresponding [Hb] was much wider in trophozoite/schizont-containing IRBCs (550 ± 230 ps, *n* = 30). Figure 18 shows the cumulative statistics for the estimates of cytosolic [Hb].

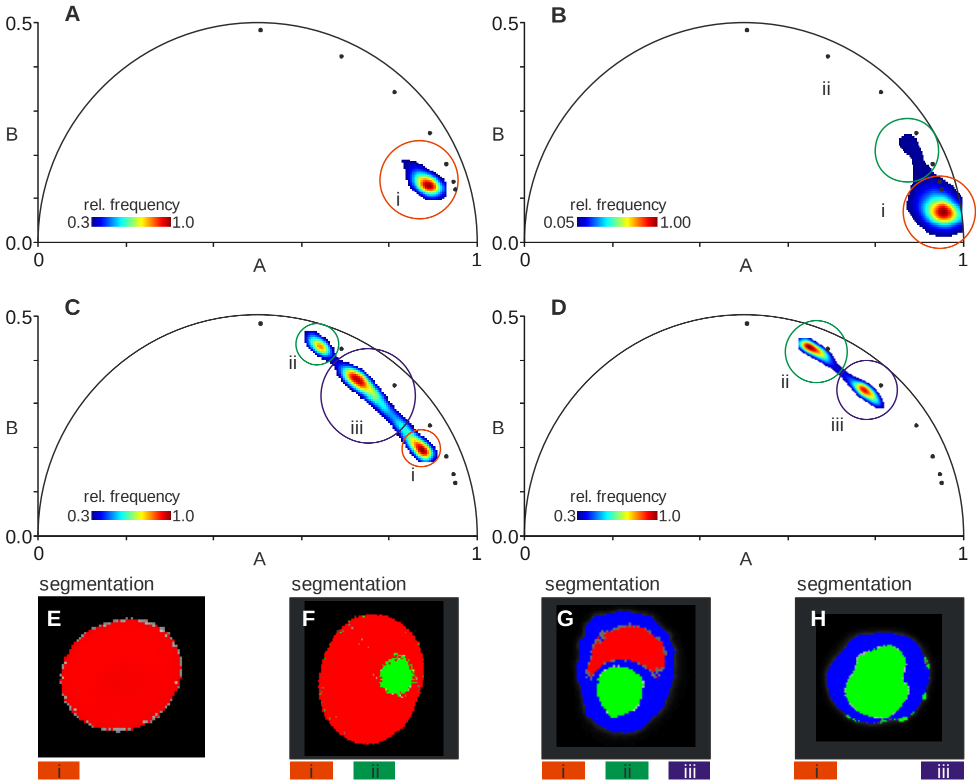

Figure 17. Segmentation of lifetime images by AB- (phasor) plots*. AB-plots and corresponding segmented regions of the cells shown in Fig. 16. The segmented regions are shown on cells in green, red and blue colours in the lower panels. (A), (E) Uninfected RBC (Figure 16B right). (B),(F) Ring-IRBC (Figure 16B left). (C),(G) Young trophozoite-IRBC (Figure 16D left). (D),(H) Mature trophozoite- / early schizont-IRBC (Figure 16E). The centroids of the phasor distributions from the calibration data (Figure 12) are indicated by the small black circles ranging clockwise along the arc from 0 mM to 6 mM. Three segmented regions are shown in the AB-plots by coloured circles: i) RBC cytosol (red), ii) malaria parasite (green) and iii) a mostly peripheral compartment (blue) within trophozoites / schizonts: see also text. Rel. frequency: relative frequency.*

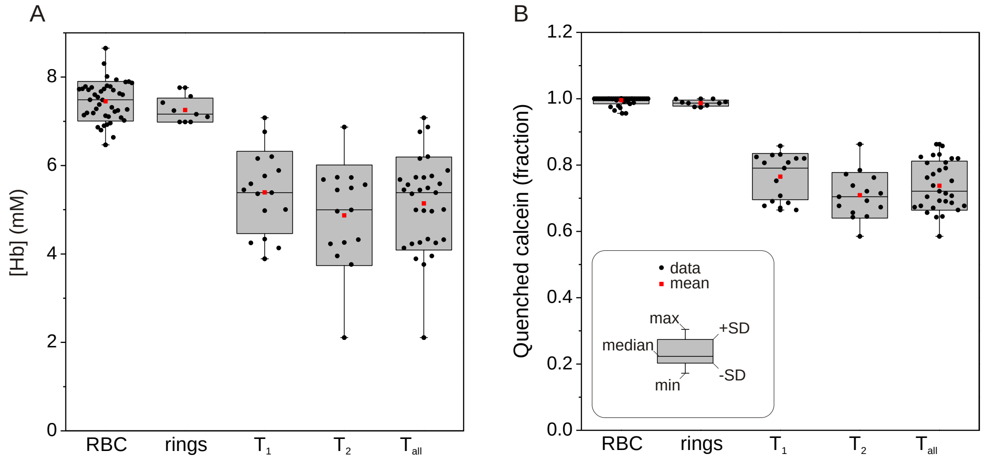

Figure 18. Statistical analysis of cytosolic [Hb] (A) and quenched calcein fractions (B). *Columns report uninfected cohorts (*RBC*), IRBCs containing ring-stage parasites (*ring*), trophozoite stage parasites (*T_1*) and trophozoite-schizont stage parasites (*T_2*), and pooled* T_1+T_2 *data (*T_{all}*). The values shown in the statistical box charts were measured in the host cytoplasm from the phasor-assisted segmentation.*

Uninfected RBCs and ring-containing IRBCs exhibited statistically similar haemoglobin concentrations of 7.3 ± 0.4 mM (n = 45) and 7.2 ± 0.3 mM (n = 10), respectively. In both cases, the fraction of quenched calcein was equal to 1.00 ± 0.01, i.e., all calcein molecules are undergoing energy transfer. RBCs containing trophozoites and schizonts were classified into two classes: young parasites (T1) and mature parasites (T2). Without specific stage and viability markers, it is impossible to attribute a more precise developmental stage and viability condition to individually selected IRBCs under confocal observation.

The visual inspection of the sample allows the classification of the IRBCs accordingly to their morphology or the presence of haemozoin aggregates. The trophozoite/schizont attribution based on fluorescent size outlines (Figure 16) and degree of pigment aggregation can only be considered a rough approximation. Notwithstanding this uncertainty, the results in Figure 18A unambiguously demonstrates the reduction in the Hb concentration within the cytosol of IRBCs with mature-stage parasites. In fractions T_1 and T_2, the haemoglobin concentrations in host-cell cytoplasm were 5.4 ± 0.9 mM (n=16) and 4.9 ± 1.1 mM (n=14), respectively, with a pooled average of 5.1 ± 1.1 mM (n=31; T_{all}). The scatter of [Hb] values was much wider in trophozoite-infected than in uninfected red cells, ranging between 2.1 and 7.1 mM (Fig 18A, T_{all}). The fraction of quenched calcein (Figure 18B) was 0.77 ± 0.07 (T_1), 0.71 ± 0.07 (T_2) and 0.74 ± 0.07 (T_{all}) suggesting a moderate compartmentalization of calcein; about 25 % of calcein molecules in the cytosol of infected RBCs was not found in close proximity of haeme moieties in spite of the high [Hb] still detected. Two thirds of trophozoite-infected RBCs (T_1) showed a third cluster, but only 20% of the cells in the fraction T_2 showed three distinct clusters in the phasor space. Analysis of values from the third cluster indicated slightly lower values of [Hb] (4.3 ± 1.1, n=13) spanning a range between 1.7 and 5.8 mM and a significantly higher compartmentalization (0.61 ± 0.09). The parasite compartment showed an apparent [Hb] value of 3 ± 1 mM and a fraction of quenched calcein of 0.46 ± 0.08. These values of course relate to sampling which included IRBC cytosol below and above the parasite as well as the parasite itself.

Discussion

The experiments presented here were designed to test a critical prediction of the colloid-osmotic hypothesis (Chapter 2, Figure 8E), that parasite development is accompanied by a progressive decline in haemoglobin concentration in the host cell cytoplasm (Lew et al., 2003; Lew et al., 2004; Mauritz et al., 2009). Some aspects of the methodological approach applied in this investigation are discussed first. As highlighted in the Motivation, the optimal way to test this hypothesis is to map the local haemoglobin concentration in the cytoplasm of intact, live, infected red blood cells. The method developed and applied for such measurements here was based on fluorescence quenching of the cell-incorporated fluorophore calcein. Both *in vitro* (lysate) and *in situ* (intact RBC) calibrations using the fluorophore calcein (Figs. 12 and 13) proved that fluorescence lifetime is sensitive to the local haemoglobin concentration. The observed reductions in fluorescence lifetimes proved that molecular crowding induced FRET is indeed the main cause of quenching and that it can be applied to estimate local [Hb].

Confocal detection together with TCSPC provided the spatial resolution required for the quantitative mapping of [Hb] in the host cell cytosol. However, the limited number of photons per pixel (~300) that could be collected in 60 s of acquisition time made image binning (5x5 pixels, see Figure 16) necessary to reach the high signal-to-noise ratios required to fit multi-parameter fitting curves (eq. S48 and eq. S52 (Esposito et al., 2007)). This standard image processing blurs structures in the sample and reduces the contrast in the cytosol of infected RBCs. The analysis of the average fluorescence lifetimes (eq. S52) indicated a significant reduction in [Hb] (data not shown), but did not provide the necessary spatial resolution. We therefore used a recent technique representing lifetime data based on AB-plots (or phasors) which map the time-resolved fluorescence decays to a linear bidimensional space where trajectories of clusters can be interpreted (Clayton et al., 2004; Digman et al., 2007). AB-plots are particularly useful for fluorescence lifetime data segmentation (Wouters and Esposito, 2008) because regions of the sample with similar fluorescence lifetimes will cluster together in the phasor space.

The results showed that the [Hb] in the host cytosol of parasitized cells decreased from values around 7.5 mM in the RBCs used for cultures, to values between 2.1-7.1 mM in IRBCs, well within the range predicted by the numerical model (Chapter 2, Figure 8E). This approach presents a more detailed view of the molecular processes occurring in a living IRBC. In fact, one of the most important advantages of this representation is the possibility of segmenting regions of the sample that exhibit different fluorescence lifetime prior to any data fitting (Wouters and Esposito, 2008). Owing to this strategy, it was possible to discriminate clearly between parasite and RBC cytoplasm. The photons collected from the segmented regions (10^5-10^8) provided the signal-to-noise ratios required to fit the proposed physical model (equation 1) and to demonstrate the reduction in cytosolic [Hb].

A surprising finding in the phasor analysis was the presence of a component with distinctive properties in IRBCs with mature parasites. Edge effects caused by RBC motion artefacts can be excluded because healthy RBCs show, at worse, a very narrow edge defined by slightly different lifetimes, which can be attributed to the mixing of calcein lifetime with background photons, resulting in faint tails in the phasor phase (Figure 17). The distinct appearance of the three clusters in phasor diagrams of trophozoite- IRBCs (see Figure 17C) suggests the formation of microdomains within the host cell cytoplasmic environment, in which haemoglobin appears largely excluded from close contact with calcein. In young trophozoites these domains are seen mainly as an extensive peripheral zone beneath the IRBC plasma membrane, with a similar though narrower zone around the parasite. In more mature IRBCs where the parasite is larger, the two regions coalesce, with no intervening Hb-rich zone (Figure 17D). This change is paralleled by an increased compartmentalization measured for calcein.

These developments are likely to reflect localized changes induced in the IRBC by the parasite (see Figure 19), including the export and assembly of molecules destined for Maurer's clefts, knobs and other parasite-derived structures in the peripheral zone of the host cell (Cooke et al., 2004; Frischknecht and Lanzer, 2008; Hanssen et al., 2008; Przyborski, 2008).

It has to be noted that also the fluorescence intensity of calcein appears higher at the cell periphery of trophozoite containing IRBCs (arrows in Figure 16C and E), but not in uninfected RBCs (Figure 16 A and C, right) or ring-stage IRBCs (Figure 16A, left), supporting the interpretation of significant calcein de-quenching beneath the membrane surface. Likewise, the traffic of parasite proteins from the parasitophorous vacuole surrounding the trophozoite is intense at this stage (Taraschi et al., 2003), and this may be related to the altered region close to the parasite surface.

The model parameters from which the colloidosmotic hypothesis was derived ensure maintenance or rapid restoration of osmotic equilibria between host cell cytoplasm and extracellular medium. Could the Hb-restricted microdomain under the host cell membrane interfere with such equilibria? It is well established that isotonic sorbitol or alanine retain their lytic potential of IRBCs with parasites of all stages beyond the ring stage indicating that the Hb-restricted domain under the membrane represents no limiting permeability barrier to water or NPP-mediated fluxes. Therefore, any domains between the bulk Hb-containing cytosol of the host cell and the external medium cannot alter the way in which osmotic equilibria are maintained or restored between these two compartments.

In conclusion, the present results demonstrate that the well known reduction in Hb content of malaria-infected RBCs is accompanied by a concomitant reduction in Hb concentration, providing support for the colloid-osmotic interpretation of excess Hb consumption. They also reveal the existence of a submembrane compartment where Hb is partially excluded, locally diluted, or both. The molecular basis of this change awaits a more detailed analysis of the complex parasite-host cell interaction.

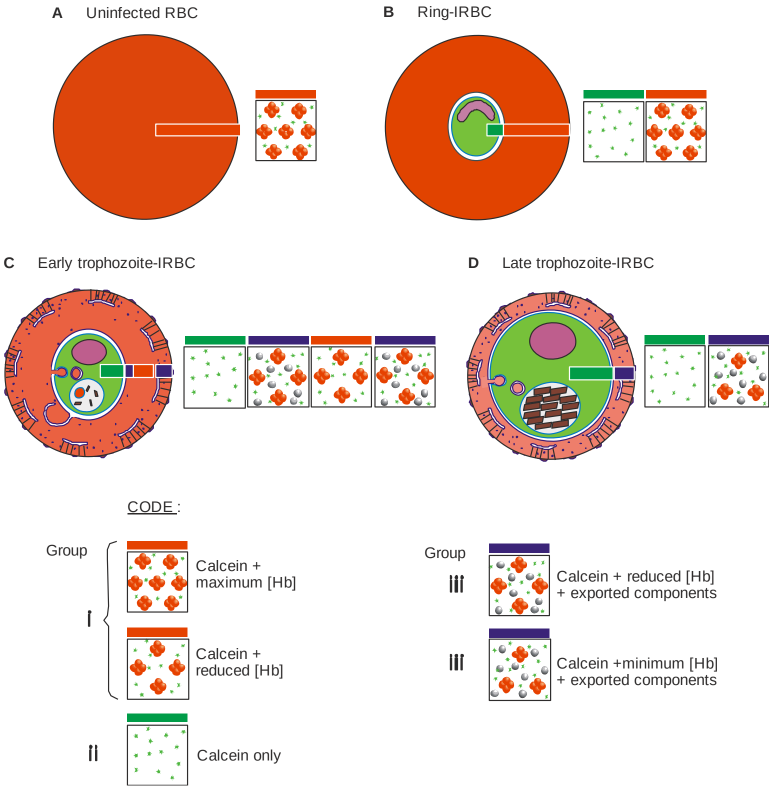

Figure 19. Interpretative diagram illustrating the observed [Hb] and compartmentation effects throughout parasite development. *The boxes represent the state of the RBC / IRBC cytosol as determined by FRET, with horizontal red, blue and green bars, as for Figure 17.*

Chapter 4: Measurement of stage-related changes in host electrolyte and haemoglobin concentrations by X-ray microanalysis

Introduction

This chapter describes the assessment of host cytosol haemoglobin concentrations with another, independent method. In contrast to optical fluorescence microscopy techniques (e.g. FLIM), electron microscopy (EM) is performed with fixed samples. Thus, the viability of the analysed cells cannot be endorsed which is a definitive disadvantage, which is compensated to some extent by the superior spatial resolution that this technique routinely achieves. EM measurements of the Hb concentration in *falciparum*-infected RBCs were attempted in the past with different methodologies and conflicting results. Comparisons of electron density between cytoplasmic domains of neighbouring IRBCs and uninfected RBCs in electron micrographs failed to detect significant differences (Lew and Hockaday, 1999). In samples from another laboratory, similar comparisons in cells from rosettes, cultures and capillaries showed a marked decrease in electron density of infected cells relative to nearby uninfected cells (Dondorp et al., 2004). There is no obvious explanation for these discrepancies. The feasibility of electron density as a measure, or rough estimate, of the original [Hb] of the cells (before sample processing for electron microscopy) requires a proper calibration procedure, not yet developed.

In the work presented here we have attempted a new approach, applying electron probe X-ray microanalysis (EPXMA) to estimate [Hb] by measuring the local elemental Fe, Na and K composition in host cytosolic domains and using the Na/K ratio as a developmental stage marker. In IRBCs with ring or young trophozoite parasite stages we expected a high Fe signal associated with a low Na/K ratio, whereas in IRBCs with mature parasites we expected a low Fe signal associated with a high Na/K ratio. From the elemental signals, the original haemoglobin concentration in the host cytosol was estimated applying a novel algorithm independent of the alterations caused by sample processing. In addition, we present here for the first time comprehensive X-ray maps of the Na, K, Cl and Fe distribution in IRBCs and a quantitative analysis of host cytosol composition in different stages of parasite development.

EPXMA has been used in malaria research previously. Lee et al. quantified the influence of the antimalarial drugs qinghaosu and chloroquine on the potassium, sodium and phosphor concentrations in host and parasite cytosol (Lee et al., 1988). It was observed that these drugs reduced parasite phosphorous concentrations, suggesting an arrest of growth. Furthermore it was found that the Na/K gradients were dissipated during parasite maturation.

Rohrbach et al. employed EPXMA to observe only moderate Ca concentrations in the parasite food vacuole and concluded that it is not a major intracellular Ca^{2+} store (Rohrbach et al., 2005). These studies raised confidence that EPXMA is a suitable method to verify the [Hb] predictions of the homeostatic model.

Electron probe X-ray microanalysis

Electron probe X-ray microanalysis is a well-established technique for the quantification of intracellular elements such as Na, K, Cl, Ca, S, P and Fe (Fernandez-Segura and Warley, 2008). In an electron microscope the interactions between the incident electron beam and individual atoms in the specimen produce various signals that can be used to determine the elemental composition of the specimen.

Through the excitation of the electron beam multiple electron-sample interactions occur and produce various signals that can be imaged, e.g.

secondary electrons, backscattered electrons or cathodoluminescence. When electrons interact with the atoms of the specimen they can also generate Auger-electrons and X-rays (Warley, 1997). The X-rays can be generated by two different mechanisms: when an incident electron collides with and ejects an electron of the inner atomic shell of a specimen atom, this electronic vacancy in the shell is filled by relaxation of higher energy shell electrons. Figure 20 sketches the naming of the different possible transitions. Such an electronic relaxation is accompanied by the emission of X-rays, whose energy is characteristic for the emitting element and its transition order. Usually only the basic K_{α}-line is intense enough for quantification. The generated X-rays do not always emerge from the specimen, as the energy can cause another outer shell electron to be ejected in a secondary reaction (Auger emission).

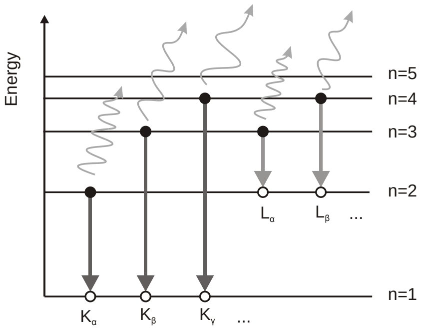

Figure 20 : Labeling of electronic transitions in X-ray spectroscopy. *Upon excitation of the sample, an electron with main quantum number n is ejected from the atomic shell. The following relaxation into a lower energy state can be accompanied by emission of an X-ray photon. These transitions are labelled according to the main quantum number of the ejected electron (alphabetically starting from K) and the origin of the electron relaxing to this vacancy (greek letters, starting from α). In this nomenclature* K_{α} *means that the electron with orbit n=1 was ejected and its vacancy filled by the electron with n=2.*

The energy of the transition is specific for the atom that had been excited and can be used to deduce the elemental composition of the investigated sample (Warley, 1997). The position of the characteristic peak in the energy spectrum can be determined by the generalized Moseley law (Gerthsen and Meschede, 2002):

$$E = R_y \cdot (Z - K)^2 \cdot \left(\frac{1}{n_1^2} - \frac{1}{n_2^2}\right), \qquad (5)$$

where R_y is the Rydberg energy (~13.6 eV), Z the elements atomic number, K the screening constant of the electronic shell and n_1 and n_2 the orbital quantum numbers of the electronic vacancy and the electron filling it. The second mechanism of X-ray generation is the deceleration and deflection of the incident electron in the Coulomb potential of the atomic nucleus. This results in a continuous spectrum termed “Bremsstrahlung” and is a quantitative measure for the specimen mass given by Kramer’s equation (Gerthsen and Meschede, 2002):

$$W = k_3 M_t \sum_a \left(f_a \cdot \frac{Z_a^2}{A_{r(a)}}\right), \qquad (6)$$

where k_3 is a constant, M_t the mass per unit area in the irradiated region, a represents any constituent element in the specimen, f_a is the mass fraction of element a, Z_a the atomic number of element a and A_r the atomic weight of a.

Sample preparation is a very critical step in any EM investigation. Because electron microscopes are operated under high vacuum, water needs to be removed from the specimen. Freezing the cells in liquid propane cooled in liquid nitrogen at specified developmental stages immobilises the elements of interest. It is important that the ice crystals generated during freezing are much smaller than the volumes to be analysed. In a 1 µl sample of packed erythrocytes only the first few micrometres will be adequately frozen and can be used. The cells are then cryo-sectioned (to improve the transversal resolution) in the frozen, hydrated state and subsequently freeze-dried to avoid the redistribution of the freely diffusible elements (Na and K) (Warley and Skepper, 2000). A thin coating of carbon is applied to improve the stability of the sections during subsequent analysis. In thin sections (100 nm thickness) a lateral spatial resolution of 10-20 nm and a minimum detectable elemental concentration of 1 mmol per kg dry mass can be achieved (Fernandez-Segura and Warley, 2008). The accuracy of this technique depends on several factors, but chiefly on the ability to separate peak from background in the spectrum and the accuracy of the calibration standards used (Warley, 1997). An accuracy for K of ±1% is possible since this element is plentiful in normal, uninfected cells and the peaks are well separated. The accuracy for Na is less than this, due to its low concentration and the higher background under this peak, whereas the accuracy for Ca is affected both by its low concentration within the cell and by overlap of its main peak (Ca-K_α) by a secondary K peak (K-K_β).

This technique is well established for biological specimens and has been in use since the 1960’s (Gupta and Roomans, 1993). It is a very robust method for gaining spatially highly resolved data, the only limitations being its lengthy and invasive sample preparation requirements.

Materials and Methods

Chemicals and Solutions.

Solution A contained (in mM): NaCl, 145; KCl, 3; Na-HEPES (pH 7.5 at 37°C), 10; $MgCl_2$, 0.15. Solution AE: same composition as solution A with the addition of 0.1 mM EGTA. The solutions used for the nystatin controls were named LA, LB, WA, WB, NA, NB and M. Their composition was (in mM): LA: NaCl, 10; KCl, 130; sucrose, 55. LB: NaCl, 130; KCl, 10; sucrose, 55. WA and WB: same composition as LA and LB, respectively, with the addition of 1 mM Na-HEPES (pH 7.4 at 37°) and 0.1% human serum albumin. NA and NB: same composition as LA and LB, respectively, with the addition of nystatin to a final concentration of 40 μM (from a stock solution of 20 μg/μl in DMSO, equivalent to 20 mM). M: $MgCl_2$, 110. All chemicals were analytical reagent quality. With the exception of the gelatin solution ("Plasmagel"; Bellon, Neuilly Sur Seine, France), RPMI-1640 culture medium and all other chemicals were from Sigma-Aldrich Company Ltd., UK.

Cultures and preparation of cells.

Red cells infected with *P. falciparum* clones ITO4 and A4BC6 (kindly provided by B.C. Elford, Institute of Molecular Medicine, Oxford, UK) (Roberts et al., 1992) , and strain POM19 (kindly provided by E. Gotuzzo, Instituto de Medicina Tropical Alexander von Humboldt, Universidad Peruana Cayetano Heredia, Lima, Peru) were cultured under a low-oxygen atmosphere by standard methods (Trager and Jensen, 1976). The culture medium was RPMI-1640 supplemented with 40 mM HEPES, 25 mg/l gentamicin sulphate, 10 mM D-glucose, 2 mM glutamine and 0.5% albumax II. Parasite development and replication were assessed in cultures by microscopic inspection of Giemsa-stained thin blood smears and parasite count, as reported before (Tiffert et al., 2000). IRBCs containing mature trophozoites or schizonts were concentrated from culture samples by gelatin flotation (Jensen, 1978; Pasvol et al., 1978) immediately prior to freezing.

Preparation of nystatin-treated RBCs.

To ascertain the reliability of the EXPMA-based estimates of cell Na and K concentrations, the Na and K content of fresh RBCs from healthy volunteers was altered by the nystatin method (Cass and Dalmark, 1973; Freedman and Hoffman, 1979) to generate high-Na and high-K RBCs covering the range of mean sodium/potassium concentration ratios expected in normal (~0.2) and trophozoite-stage infected (>5) red blood cells. RBCs were obtained from healthy volunteers by venipuncture into a syringe with heparin after informed, written consent. The RBCs were washed thrice by centrifugation and resuspension in over 10 volumes of solution AE, and once in solution A. The buffy coat was removed after each wash. After the last wash, the cells were distributed in three equal aliquots, one to serve as an untreated control was suspended in solution A, and of the other two one was equilibrated for 20 min in high-K medium NA, and the other one in high-Na medium NB, both containing nystatin. The haematocrit was 10% and all the suspensions were kept on ice. Nystatin was removed by washing the cells four times in A, WA or WB, respectively, with three final washes of all samples in isotonic $MgCl_2$ (solution M) to remove extracellular Na and K prior to EPXMA analysis.

Sample processing for electronmicroscopy.

Samples containing RBCs in suspension in 1.5 ml nominal capacity microfuge tubes were briefly spun down and the supernatant removed. Wooden cocktailsticks were dipped into the cell pellet, which was then quickly plunge-frozen in liquid propane, cooled in liquid nitrogen (−196°C), immobilising the elements of interest (Warley, 1997; Warley and Skepper, 2000). The frozen pellet was cut into thin sections of 180 nm thickness at −100°C in a cryo-sectioning stage (Leica UltraCutS, with FCS, Leica Microsystems, Wetzlar, Germany). The sections were put on carbon film-coated nickel grids and subsequently transferred under liquid nitrogen into a turbo molecular pumped carbon coater (Auto 306, Edwards Ltd., Crawley, UK) were they were freeze-dried overnight and carbon coated. The EM grids were stored in a dessicator until analysis.

Electron Microscopy and X-ray microanalysis.

For the EXPMA analysis the samples were transferred at room temperature into a transmission electron microscope (Tecnai T12, FEI Company, Hillsboro, USA) fitted with an electron beam and image deflection (EBID) board to allow collection of X-ray maps(Morgan et al., 1994), and a Si(Li) energy dispersive X-ray detector (EDAX, Tilberg, The Netherlands). For the X-ray microanalysis, the microscope was operated at 120 kV in nanoprobe mode using a probe size of roughly 10 nm diameter. The grid was tilted 25° towards the detector. The relative detector sensitivity (S-values) was calibrated for Na, K and Fe with Na-K-tartrate and K-ferricyanate in gelatine. For spectrum analysis and element mapping EDAX Genesis software (EDAX, Tilberg, The Netherlands) was used. Data of the electron probe measured elemental composition were recorded from between 5 and 40 different cells in each sample, and the results are reported as the mean and standard error of the mean.

Quantifying cytosol composition.

The calibrated electron probe data obtained from freeze-dried cryosections are reported in units of mmol/(Kg dry weight), or mmol/Kg. A main aim in this investigation was to estimate the haemoglobin concentration in the red cell cytoplasm in units of mmol/(litre cell water), or mmol/Lcw. This required a reliable conversion procedure for both uninfected controls and infected RBCs, independent of the nature of the dry weight material. Searching for a reliable conversion strategy (Somlyo et al., 1985), we developed one based on the well established fact that RBCs attain and maintain osmotic equilibrium across their plasma membrane because of their high water permeability (Whitham, 1964). With RBCs equilibrated in solution A (~ 300 mOsM) prior to freezing, the intracellular concentrations of Na plus K in cell water ([Na]+[K]) would have to be very near 150 mmol/Lcw because K and Na are the main intracellular cations available to balance the negative charges on cell anions. Let *cNa* and *cK* represent the respective electron probe measured elemental composition of Na and K in each spot, in units of mmol/(Kg dry weight). The ratio $f = (cNa+cK)/([\mathrm{Na}]+[\mathrm{K}])$, in units of Lcw/Kg, renders the volume of cell water associated with a unit Kg dry weight of each imaged spot in the cryosection. We can now divide the elemental composition of Fe in that sample, cFe, by *f* to obtain the monomeric haemoglobin concentration in units of mmol/Lcw. Thus, the concentration of the Hb tetramer, [Hb], in units of mmol/Lcw, will be given by: $[\mathrm{Hb}] = cFe/(4f)$. Similarly, the electron probe measured Na and K concentrations per Kg dry weight, *cNa* and *cK*, respectively, can be converted to the original concentrations of Na and K in RBC water, [Na] and [K], in units of mmol/Lcw, using $[\mathrm{Na}] = cNa/f$ and $[\mathrm{K}] = cK/f$. The individual electron probe concentrations retrieved from each imaged spot differ greatly. The *cX* to [X] conversion defined above normalizes all values to comparable quantities, and, as shown in Results, renders values well within the expected ranges for uninfected RBCs and nystatin-treated controls. The same approach was applied to estimate the Na and K concentrations within parasite cytoplasm.

Results

Sample X-ray spectra.

Figure 21 shows representative X-ray spectra of cytosolic domains of uninfected (A) and trophozoite-stage infected (B) red blood cells, and of the parasite cytoplasm away from the food vacuole (C). In the uninfected RBC, K is the dominant peak (Figure 21A), whereas in the infected red cell Na is dominant and the K peak is much reduced (Figure 21B). In the parasite cytoplasm (Figure 21C), K is again dominant over Na, and shares dominanace with phosphate (P), reflecting high metabolic activity. The Fe peak is present in the cytosol of the red cells but vanishingly small in parasite cytoplasm. The P and S elemental peaks are also shown, but were not investigated further here. The Si signal corresponds to desiccant contamination.

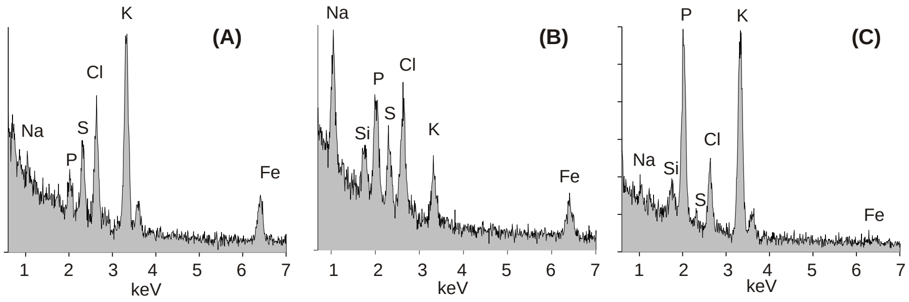

Figure 21: ***X-ray spectra of IRBCs in different stages****. The element label in each panel is directly above the respective* $K_{\alpha 1}$*-transition peak.* ***Panel A****: Uninfected RBC cytosol, high in K and low in Na;* ***Panel B****: RBC host cytosol (from trophozoite IRBC), high in Na and low in K.* ***Panel C****: Trophozoite cytosol. The Na/K composition is similar to the uninfected RBC, but in contrast the high P dominates the spectrum, indicating metabolic activity. The present Ni peak of the EM grid and the C, O and N peaks of the sample are beyond the shown energetic range. The Si-peaks are an artifact stemming from the dessicant.*

Elemental X-ray maps.

Representative EM images of IRBC thin sections are shown with their corresponding X-ray maps in Figure 22. The maps represent the elemental distribution of Na, K and Fe in a colour coded red-green-blue overlay. The algorithm used for visualisation renders the colours resulting from mixing red (for K), green (for Na) and blue (for Fe) according to their relative intensities in each pixel, so that e.g. a violet colour in the map corresponds to a region high in both Fe and K. Additional elemental maps, including Cl distributions, are shown in Figures 45- 47 in Appendix C.

Figure 22A shows an electronmicrograph of an uninfected RBC section. Adjacent to the cell the salt contents of the (freeze-dried) cell suspension medium can be seen as transparent matrix. In the corresponding X-ray map (Figure 22B) the extracellular region presents a strong Na signal and is low in Fe and K. At the cell boundary, the sharp transition of the dominant element from Na to K can be clearly seen, with the cytosol high in K (red) and low in Na (green). The Fe signal (blue) is homogeneous throughout the cell.

Figure 22C. shows an electronmicrograph of an IRBC with a mature trophozoite. The host cytosol appears uniformly dark and clearly distinguishable from the brighter parasite region. In the food vacuole, the haemozoin crystals can be seen as dark spots. The corresponding X-ray map (Figure 22D), displays a stark contrast between parasite (high K) and host cytosol (high Na). The dominant iron signals in Figs 22D and 22F co-localize with the iron-rich haemozoin crystal images in the corresponding micrographs (Figs 22C and 22E). Note the remarkable similarity between the green-red transitions across the medium-cell boundary in Figure 22B and across the host-parasite boundaries in Figures 22D and 22F, illustrating visually the extracellular-like high-Na, low-K environment surrounding the parasite within the host red cell.

Figure 22E depicts two IRBCs with mature trophozites and two adjacent RBC fragments. The cells in this image, from a trophozite-enriched sample with no ring-stage parasites, had been washed in isotonic $MgCl_2$ before freezing, thus removing X-ray signals from the extracellular medium. In the electron micrograph (Figure 22E) it is impossible to tell whether or not the adjacent cell fragments correspond to uninfected cells. But the X-ray map in Figure 22F reveals the high-K content of the cell fragments, indicating that they correspond to uninfected RBCs.

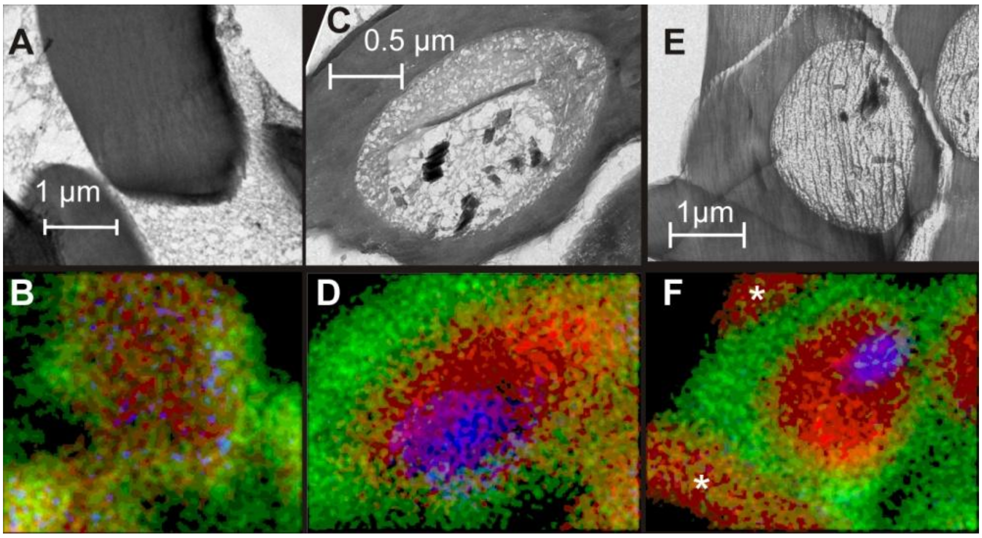

Figure 22: ***Comparison of TEM and corresponding EPXMA images****. The EPXMA maps are assembled as a red-green-blue overlay of the Na (green), K (red) and Fe (blue) X-ray raw peak count. Panels A and B: uninfected RBC surrounded by salt crust from the dried extracellular medium, Panel C and D: trophozoite IRBC with parasite and food vacuole. The black spots are haemozoin crystals responsible for the high Fe signal. Panel E and F: Trophozoite IRBC surrounded by two uninfected RBCs. The X-ray image renders very clear contrast between the different cells. Separate maps for each cell and each element can be found in Appendix C.*

Sodium, potassium and iron (haemoglobin) concentrations within host-cell and parasite domains.

Figure 23A shows a representative sample of electron probe measured elemental Na, K and Fe composition obtained from the cytoplasm of uninfected control RBCs and from cohort RBCs separated from a live Pf culture. The results show the typical low-Na, high-K pattern of normal, uninfected RBCs. The estimated cytoplasmic concentrations of Na, K and Hb derived from these measurements, using $[Na] = cNa/f$, $[K] = cK/f$, and $[Hb] = cFe/4f$ (see Methods), are shown in Figure 23B and report values well within the variation range found in RBCs from healthy human adults. The estimated mean Hb concentration in all RBC samples analysed was was 6.5 ± 0.2 mM (n=33).

Nystatin (see Methods) was used to generate RBCs with inverted Na/K contents to test the reliability of the electron probe to accurately report such variations. The measurements obtained are shown in Figure 23C, and the derived concentrations in Figure 23D. It can be seen that the inverted Na/K ratio (Figure 23E) was accurately reproduced, establishing the validity of electron probe measurements of Na/K concentration ratios within the cytoplasm of infected RBCs as an approximate indicator of parasite developmental state.

Figure 24 shows a comparison between electron probe derived concentrations of Na, K and Fe in the cytoplasms of host and parasite, obtained from an IRBC with a mature trophozoite. Parasite cytoplasm data was acquired as far away from the food vacuole as was possible, to avoid signal contribution from the high Fe content of the haemozoin crystals.

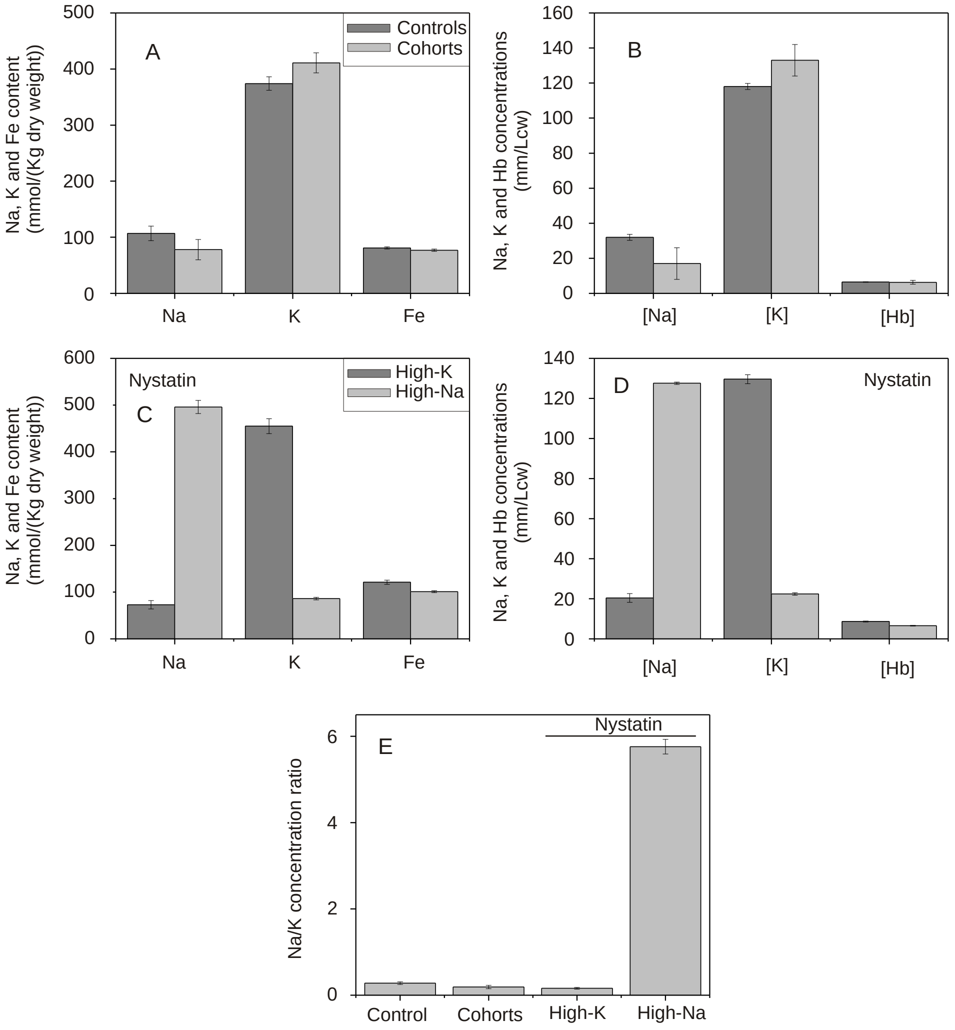

***Figure 23: EPXMA measurements of uninfected RBCs**. The bar plots indicate the measured average values with their standard error of the mean. Panel A shows the cytosol composition of Na, K and Fe for a control RBC sample (n=33) and cohorts RBCs from a mature trophozoite sample (n=5) as reported by the EPXMA method. Panel B scales the same data to water concentration of [Na], [K] and [Hb] as outlined in the Methods section. Panel C reports the cytosol composition for Na, K and Fe of the nystatin treated RBCs, prepared high in K^+ (n=20) and high in Na^+ (n=25). Panel D shows the nystatin treated RBC data converted to water*

concentration for [Na], [K] and [Hb]. Panel E compares the Na/K concentration ratio for the four above samples. The efficacy of the nystatin method to prepare high K^+ RBC can clearly be seen.

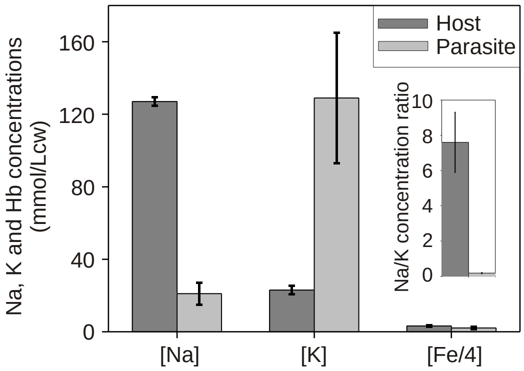

Figure 24: Cytosol composition of representative host and parasite IRBCs. *The bar plots indicate the measured average values with their standard error of the mean. The Na, K and Fe/4 concentrations were derived from the EPXMA data as described in Methods and are compared for the parasite (n=14) and host cytosol (n=15) from mature trophozoite samples. The inset shows the Na/K concentration ratio, which underlines the very different electrolyte composition. These data indicate the dissipation of the extracellular Na^+ and K^+ gradients at the RBC membrane and their re-occurence at the parasitophorous vacuolar membrane.*

At this developmental stage, the probe detected a high-Na, low-K pattern in the host cytoplasm, and the opposite pattern within the parasite cytoplasm (Figure 24 inset) confirming earlier measurements in host cells and parasites (Overman, 1947; Dunn, 1969; Ginsburg et al., 1986; Lee et al., 1988; Wunsch et al., 1998; Staines et al., 2001). The Hb concentration of 2.8 mmol/Lcw in the host corresponds to a reduction of over 50% from mean normal levels.

The origin of the Fe signal and of the Fe/4 value of 1.6 mmol/Lcw within the parasite cytosol may be attributed to endostomal Hb or haeme proximity, but cannot be identified from these measurements.

The results of 155 electron probe Na, K and Fe measurements in the cytoplasm of IRBCs with parasites in different developmental stages are shown in Figure 25. The haemoglobin concentration is plotted as a function of the Na/K concentration ratio, higher ratio values suggesting more advanced developmental stages. The results expose a clear trend of decreasing haemoglobin concentration with increasing Na/K ratio, but the rate of decline with Na/K ratio shows two distinct patterns, of sharp and gentle decline, in IRBCs from different cultures.

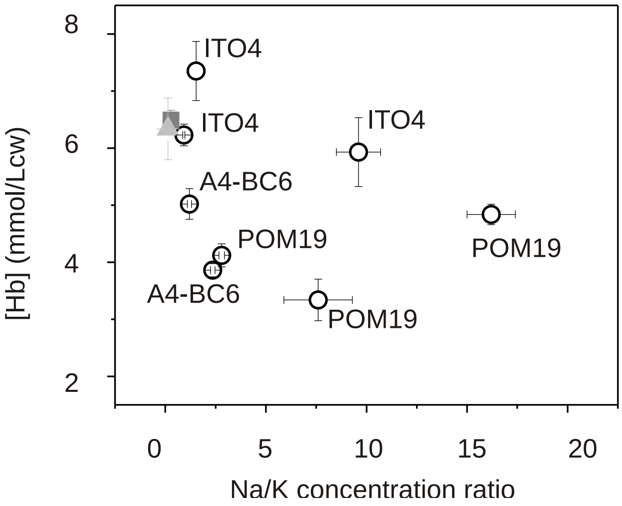

Figure 25: Quantification of the (I)RBC cytosol for different parasite stages. *The ordinate represents the Na/K ratio as parasite stage marker, while the abscissa reports [Hb]. The IRBC samples (from 8 different samples; 155 host cells analysed in total) are depicted as open circles, the uninfected control sample (n=33) as square and the cohort cytosol (n=5) measurement as triangle. The standard errors of the mean are represented as cross-hairs. All IRBC samples with a high Na/K have a reduced [Hb]. One ring stage sample can be seen that has a larger [Hb] than the uninfected control sample. This can be caused by a transient IRBC dehydration upon the onset of the NPP.*

Discussion

EPXMA imaging has been used here to document the distribution of Na, K and Fe in *P. falciparum* infected red blood cells. The X-ray maps shown in Figure 22 illustrate this distribution in the different subcellular domains of IRBCs. The maps confirm that during *P. falciparum* infection, the cation composition of the host cell cytoplasm changes dramatically, with dissipation of the normal Na/K gradients across the RBC membrane, whereas the parasite cytoplasm retains a typical high-K, low-Na intracellular environment.

The maps also show the distribution of iron containing molecules, haemoglobin and haemozoin. The more quantitative estimates derived from the electron probe measurements of Na, K and Fe (Figs 24 and 25) confirm the overall qualitative description provided by the X-ray maps, and provide independent evidence of a decline in haemoglobin concentration associated with elevated Na/K concentration ratios within the host cell cytoplasm.

These results then confirm previous observations of stage-related decline in Hb concentration obtained with different optical methods (Chapter 3) and (Park et al., 2008) and add support to the view that excess Hb consumption contributes to retain the integrity of the osmotically fragile IRBCs (Chapter 2) and (Lew et al., 2003; Lew et al., 2004) by reducing the colloidosmotic pressure within the host cell.

The origin of the two distinct patterns of decline in Hb concentration with Na/K ratio shown in Figure 25 deserve further consideration. The mathematical-computational model of IRBC homeostasis (Lew et al., 2003; Lew et al., 2004; Mauritz et al., 2009) was applied for fitting these data, to search for clues about possible biological variations that may explain the steep and gentle [Hb] decline pattens observed. The search was on for the minimal set of parameter values that could provide adequate fits of the experimental points in Figure 25. The approximate fits for both [Hb] decline modalities shown in Figure 26A were obtained by varying a single critical parameter, the PK/PNa ratio, representing the Na-K selectivity attributed to NPPs. Additional fine-tuning was possible by minor adjustments in other parameters, but PK/PNa remained the only critical parameter, irreplaceable for the fit. Mean values of PK/PNa of 2.3 reported by Staines et al (Staines et al., 2001) rendered a decline curve that approximated well the gentle decline pattern. To fit the sharp decline pattern it was necessary to abolish the cation selectivity of the NPP pathway with PK/PNa values near 1 (Figs 25A).

To understand how this relatively minor parameter adjustment in the residual cation selectivity of a major anion-selective pathway (Kirk) can produce such a marked difference in the pattern of [Hb] decline, it is necessary to analyse the associated time–dependent changes in [Na], [K] and [Hb], the relevant model variables in the plot of Figure 25.

Figures 26B and 26C show the patterns of Na-K gradient dissipation and of [Hb] decline as a function of time post-invasion predicted by model simulations with (filled symbols) and without (open symbols) PK/PNa selectivity. It can be seen that whereas the [Na], [K] and [Na]/[K] ratio changes are almost identical in both conditions, the time-course and pattern of the [Hb] changes are markedly different.

Since the extent and timing of Hb consumption was set identical for both conditions in the modelled simulations, any changes in [Hb] could only result from host-cell water-volume variations induced by the different NPP selectivities. The predicted time-course of host-cell water-volume changes is shown in Figure 26D.

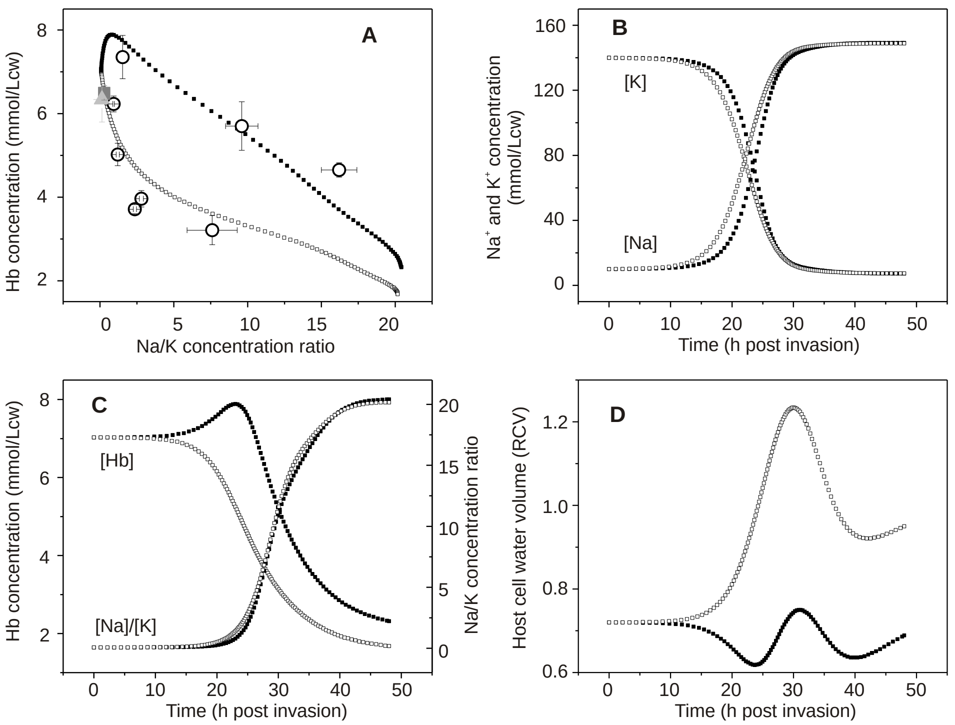

Figure 26: Quantitative microanalysis data and their implications for modeling the IRBC homeostasis. *Panel A: Comparing the EPXMA measurements and two different model simulations to fit the data. Experimental data are plotted as in Figure 25. The upper fitting curve (closed squares) assumes a* K^+ *specific NPP with* $P_K/P_{Na}=2.3$*, whereas the lower curve (open squares) was modeled with* $P_K/P_{Na}=0.9$*. All other parameters were the same in both simulations (CF=0.3,* $Hb_{max}=0.7$*,* $t_{1/2}(NPP)=27$ *h and* $t_{1/2}(Hb)=32$ *h* $s_{NPP}=s_{Hb}=3\ h^{-1}$*) (Mauritz et al., 2009). Panel B-F show only simulated variables of the two different fits. For consistency the open symbols represent the unspecific NPP (lower curve of Panel A), the closed symbols stand for the* K^+*-selective NPP (upper curve of Panel A).* ***Panel B: Na and K concentrations. Panel C: Hb concentration (left ordinate) and Na/K concentration ratio (right ordinate)****, The most notable qualitative difference between the two simulations is the transient increase [Hb] directly after the onset of the* K^+*-*

specific NPPs. For the unspecific NPPs this transient perturbations is not expected, because the K^+ outflow is matched by an equal inflow of Na^+, and no accompanying transient osmotic water outflow is theorized. The time course of the Na/K concentration ratio rises after NPP activation and increases monotoneously. ***Panel D: Host cell water volume.***

The mechanisms responsible for these changes when PK/PNa is set to 2.3 (Staines et al., 2001) have been reported and analysed before (Mauritz et al., 2009; Esposito et al., 2010). Briefly, with PK > PNa, the onset of NPP permeabilization causes transient dehydration because initially KCl loss exceeds NaCl gain for a brief period of time.

As the K-gradient dissipates, NaCl influx soon exceeds KCl efflux causing delayed but sustained osmotic water gain. Without cation selectivity, on the other hand, the initial dehydration is absent (Figure 26D) because NaCl gain exceeds KCl loss all along. The ensuing sustained swelling from the start of NPP permeabilization (Figure 26D), which lasts for most of the intense Hb consumption period, causes a fall in Hb concentration much earlier than when PK > PNa (Figure 26C). The initial [Hb] peak, responsible for the biphasic pattern predicted for the condition with PK > PNa, is thus absent when selectivity is removed (Figs 26A and 26C).

The model-derived explanation of the gentle and steep [Hb] decline patterns when [Hb] is plotted as a function of the electron probe measured cNa/cK ratio (equal to the [Na]/[K] ratio) can be followed from the curves in Figure 26C. Comparison of the temporal courses of the [Hb] and [Na]/[K] curves shows that with no cation selectivity the [Hb] fall starts when the [Na]/[K] ratios are still very low, while [Hb] is increasing towards a peak value in the condition with PK > PNa. In this condition, [Hb] decline starts by the time Na-K gradient dissipation is already well advanced. Thus, when plotted as a function of the [Na]/[K] ratio, the [Hb] decline patterns return the steep-gentle modalities observed.

The model analysis then allows for an interpretation of the observed [Hb] decline patterns consistent with IRBC viability for both modalities, provided we accept the notion that the Na-K selectivity of the NPP pathway can vary in cultures of the same *falciparum* strains initiated from different stabilates. Small variations in NPP-mediated cation selectivity can thus generate the marked differences in pattern of [Hb] decline documented here in Figs 25 and 26A. However, this explanation cannot be independently ascertained at this stage.

Chapter 5 : Measurement of stage-related volume changes of infected cells using fluorescence confocal microscopy

Introduction

After experimentally confirming the predicted reduction in haemoglobin concentration by two independent methods, this chapter is concerned with the other homeostatic variable that was yet to be characterized experimentally. In the initial IRBC model, the volume gain of the parasite was equal to the amount of haemoglobin ingested and digested by the parasite (Lew et al., 2003; Lew et al., 2004). Furthermore, it was thought that directly after onset of the NPP permeability a transient and uncompensated outflow of K^+ and host cell water would briefly reduce the total IRBC volume (see Figure 4A). However, on dissipation of initial Na^+/K^+ membrane gradients, the combined effect of parasite growth and water inflow due to the Hb colloid-osmotic pressure was thought to result in steady and sustained IRBC volume growth. This hypothesis was supported by osmotic fragility (OF) measurements of IRBCs (Lew et al., 2003; Lew et al., 2004). Osmotic fragility curves record the fraction of lysed cells at varying tonicities of the surrounding medium. They showed a progressive increase in IRBCs with late-stage parasites, suggesting a gradual proximity of the IRBCs to their maximal critical spherical volume (CHV) (Lew et al., 2003; Lew et al., 2004). Typically, variations in osmotic fragilities are attributed to RBC volume changes; therefore, OF curves as in Figure 27 appeared to confirm the model predictions of a transient IRBC volume decrease followed by a sustained increase. However, estimates of the IRBC water content which showed little or no increase in IRBC volume late in the parasite cycle (Zanner et al., 1990; Saliba et al., 1998; Elliott et al., 2001; Allen and Kirk, 2004; Elliott et al., 2008; Park et al., 2008) seemed to contradict the volume predictions.

Moreover, studies on the egress process of merozoites suggested a pre-rupture terminal state of the infected cell with a near spherical configuration (Glushakova et al., 2005).

Together, these data posed an apparent conflict between volume measurements suggesting little change, osmotic fragility measurements suggesting progressive proximity of IRBCs to their critical haemolytic volume and a pre-lytic spherical IRBC shape. How could these apparent contradictory findings be reconciled?

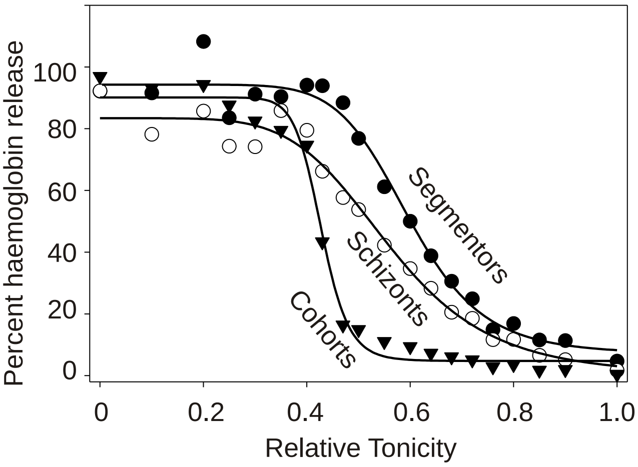

Figure 27: Osmotic fragility curves of IRBCs in various stages. *The graph plots haemoglobin release versus relative tonicity of the extracellular medium. Cohort RBCs are shown as closed triangles, schizonts as open circles and segmentors as closed circles. When lowering the relative tonicity of the medium, a higher fraction of infected cells lyses and releases haemoglobin. This increase in osmotic fragility was initially attributed to IRBC swelling during parasite maturation. Data from unsynchronized parasite cultures showed both a fraction of cells that are further away from haemolysis than uninfected RBCs* and *a fraction of cells that are in close proximity to it (not shown). Data kindly provided by Dr Lew, see also (Lew et al., 2003; Lew et al., 2004).*

One possibility is that the membrane area of IRBCs with late-stage parasites is progressively reduced with a concomitant reduction in critical haemolytic volume. But here again, the evidence for loss of membrane area is inconsistent (Nash et al., 1989; Zanner et al., 1990; Omodeo-Sale et al., 2003). There is a need to clarify this situation, and this provides the motivation for the following chapter to deliver reliable volume/area estimates of live cells from *P. falciparum* cultures.

Technique: Optical Microscopy in malaria research

Wide-field differential interference contrast (DIC) and fluorescence microscopy are the classical "workhorses" used for studying live IRBCs. Optical microscopy permits the non invasive imaging of IRBCs, the study of parasite development (Glushakova et al., 2007), mapping the localization of proteins (Tokumasu et al., 2005) or characterizing alterations of host cell morphology (Esposito et al., 2010). Chemical and laser-light toxicity is known to occur, but protocols for minimizing these problems have been characterized (Tokumasu and Dvorak, 2003; Glushakova et al., 2005). Wide-field imaging of IRBC has been extraordinarily successful in investigating RBC invasion and merozoite release processes. Glushakova et al. used time-lapsed imaging for recording RBC membrane transformations during merozoite egress (Tokumasu and Dvorak, 2003; Glushakova et al., 2005; Glushakova et al., 2007). Their results showed that immediately prior to rupture IRBC morphology changes into a near-spherical configuration and helped distinguish between different hypothetical models of merozoite egress. Imaging at higher three-dimensional resolution can be achieved by employing a confocal laser scanning microscope (CLSM) combined with fluorescence techniques and fluorophore-loaded cells.

This allows non invasive volumetric imaging of biological samples. A confocal microscope produces sharp optical sections by removing out-of-focus image blur through the use of a pinhole positioned in front of the detector. The resolution of a typical CLSM equipped with a high numerical aperture objective is about 200-250 nm laterally and 500-700 nm along the optical axis for a green fluorophore. Each optical section is acquired by scanning the laser in the sample plane with galvanometric mirrors; a number of optical sections are then acquired by sweeping the focal plane of the microscope through the sample. The image stacks are subsequently deconvolved to further improve resolution (Boutet de Monvel et al., 2001) and this can be applied to measure cell volumes and surface areas (Mauritz et al., 2010).

A variation to this setup is the use of an array of pinholes rapidly scanned in front of a wide field detector such as in Nipkov-disk based confocal microscopes. Tokumasu and Dvorak combined the high 3D resolution of a Nipkov-disk confocal with labeling fixed IRBCs with quantum dots, fluorophores that circumvent the common problem of rapid photobleaching observed with classical fluorophores (Tokumasu and Dvorak, 2003; Tokumasu et al., 2005). In their study, the quantum dots were used to immuno-label the membrane protein band 3 and image the host cell membrane deformations during merozoite invasion. They were also able to map the distribution of Band 3 which surprisingly occurred inhomogeneously clustered on the erythrocyte membrane (Tokumasu et al., 2005).

This chapter is concerned with volumetric measurements of IRBCs. This analysis required the development of a novel processing algorithm specifically designed to meet the challenges posed by the complex and continuously evolving shapes of infected RBCs. The emphasis is to provide measurement data from single, live cells, investigated under optimal physiological conditions which are precise and statistically significant. The algorithm generates three-dimensional isosurfaces (surfaces of constant fluorescence intensity) from the deconvolved image stacks, which are then elastically deformed until an optimal fit is found for the cell-to-background transition in the images. The object contours generated from the isosurface (fit assisted isosurfacing algorithm) has sub-pixel resolution and permits robust volume-area estimations. Application of this algorithm to IRBC imaging showed that the volume of infected red cells varied little during the parasite reproductive cycle, but in turn membrane area loss was significant.

As mentioned before (p. 36), most of the actual experiments described here and in Chapter 3 were performed in several parallel sessions (measuring [Hb] and volumes on two different microscopes) by Dr Alessandro Esposito and the author, as to make the most economic use of the parasite cultures, which are time and cost intensive to grow and sustain. The author conducted the actual measurement at the confocal microscope, deconvolved the image stacks, applied the volume rendering algorithm and compared the final results with the volume predictions of the model, whereas Dr Esposito designed the experiment, developed the imaging algorithm and prepared the published journal article that also describes the new algorithm in detail (Esposito et al., 2010).

Materials and Methods

Chemicals and solutions.

All chemicals were analytical reagent quality. Calcein-AM was from Invitrogen Ltd., Paisley, UK. Plasmagel was from Bellon, Neuilly Sur Seine, France. EGTA, Hepes, glucose, inosine, pyruvate, DMSO, RPMI 1640 medium, gentamicin sulphate, glutamine, bovine serum albumin (BSA), ultra low gelling temperature agarose (Sigma Type IX) and all common salts were from Sigma-Aldrich Company Ltd., Gillingham, UK. Human blood and serum used in cultures were from the National Blood Service (UK). Solution A contained (in mM): NaCl, 145; KCl, 3; Na-HEPES (pH 7.5 at 37$_o$C), 10; MgCl2, 0.15. Solution AE: as A plus 0.1 mM Na-EGTA. Solution AIP: as A plus 5 mM inosine and 5 mM pyruvate. Calcein-AM was used as a stock solution of 0.7 mM in DMSO. The stock solution of free calcein was 10 mM in DMSO. Agarose was dissolved at 2% (w/v) in solution AE on the day of use.

Cultures.

Two *P. falciparum* clones (ITO4 and A4BC6, kindly provided by B.C. Elford, Institute of Molecular Medicine, Oxford, UK) (Berendt et al., 1989) were cultured separately in human erythrocytes under a low-oxygen atmosphere by standard methods (Trager and Jensen, 1976). The culture medium was RPMI 1640 supplemented with 40 mM HEPES, 25 mg/l gentamicin sulphate, 10 mM D-glucose, 2 mM glutamine and 8.5 % (vol/vol) pooled human serum. Parasite development and replication were assessed in cultures by microscopic examination of Giemsa-stained thin blood smears, as reported before (Tiffert et al., 2000). Parasitized RBCs were harvested from asynchronous cultures immediately prior to experimentation. Because the aim of the study was to measure the volume of the cells as similar as possible to their original conditions in culture, it was important to establish which procedure would ensure such outcome best. Therefore, preliminary experiments were performed to establish that the used protocols did not significantly altered parasite viability (see also calcein loading and microscopy).

Calcein loading.

Cells from a *P. falciparum* culture sample were washed once by centrifugation (400 *g* x 5 min) and resuspension in 10-20 volumes of solution AIP and the washed cells suspended at ~2% hematocrit (Hct) in the same solution. A 1-2 ml aliquot of this cell suspension was mixed with calcein-AM stock to a final concentration of ~120 μM in the suspension and incubated at 37 °C for 20 min. Inosine in the medium was used as a glycolytic substrate and pyruvate to bypass the glycolytic block generated by the release of formaldehyde during the breakdown of the acetoxymethyl ester that remains fully retained by the cells (Tiffert et al., 1984; Garcia-Sancho, 1985). After incubation, the cells were washed twice with solution AIP and the final pellet diluted ten-fold in AIP medium. One microliter of this cell suspension was gently mixed with 50 μl of the agarose solution (see Chemicals and Solutions) on the surface of a glass culture dish (#1.0, MatTek Corp., Ashland, MA, USA). The culture dish was incubated for 3 min at 4° C to allow gelling, and immediately thereafter covered with 100 μl of solution AE with 1 % BSA, at room temperature, to prevent dehydration of the IRBC-gel mixture during imaging. Preliminary trials showed that gel hydration was essential to prevent cell dehydration, and BSA presence was necessary to prevent large scale crenation of both normal and infected cells. The immobilized cells were allowed to settle for about 10-15 min on the microscopy stage and subsequently imaged for a maximum of 30 min at room temperature (~ 20°C), allowing imaging of 4-6 fields per sample. Repeated volume measurements over the same cell showed no detectable changes in volume during this period. Beyond 30 min, both uninfected and infected cells showed progressive signs of deterioration such as increased frequency of spontaneous lysis and shape changes.

The images obtained following these procedures systematically rendered normal cell shapes, areas and volumes for uninfected RBCs and ring-stage-infected RBCs. Bright field images of calcein-loaded IRBCs with late-stage parasites obtained from within the agarose gel were consistent with the variety of IRBC shapes reported before for *falciparum* cultures. The protocol applied was therefore considered to cause minimal perturbation and to be best suited for 3D imaging of living IRBCs. A critical point in the early stages of this investigation was to set clear selection criteria for trophozoite and schizont stages. Trophozoite-stage IRBCs were selected as those showing a clear food vacuole with visible haemozoin crystals in Brownian motion; these structures were clearly identified both in fluorescence and transmission images (Figure 31C). Mature trophozoite-schizontstage IRBCs were those with haemozoin crystals compacted into a residual body configuration, with clear evidence of incipient or advanced parasite division within a highly deformed host cell (Figure 31D-E). Preliminary experiments showed that IRBCs exposed to the procedures outlined above for calcein loading and imaging were able to sustain parasitemias near control levels on further culture, indicating that a substantial fraction of the imaged cells were viable. No differences could be detected between the microscopic appearance of unfixed cells immediately out of the culture and those embedded in the agarose gel. Preliminary experiments showed that membrane staining with biotinylated RBC membrane and streptavidine coated quantum dots or with the membrane probe FM4-64 did not provide as good a signal-to-noise ratio for volume measurements as calcein, for different reasons. Membrane labelling by sub-lytic concentrations of quantum dots proved deficient and FM4-64 photobleached within the acquisition time required for 3D imaging.

Microscopy.

Images were acquired with a Leica SP5 AOBS confocal microscope (Leica UK Ltd., Milton Keynes, UK) using a HCX PL APO 63.0x1.20 WATER UV water immersion objective (Leica UK). Calcein was excited with the 488 nm laser line and fluorescence was collected over the 500 – 560 nm band. Bright field images were collected with the transmission detector. Typically, images were acquired with a x-y pixel resolution of 50 nm, with a separation between optical sactions of 150 nm and with a 1 Airy-disk pinhole. Images were then restored (Difato et al., 2004) with Huygens (SVI, Hilversum, NL) and analysed with a Matlab routine (The MathWorks Inc., Novi, MI, USA) developed by Dr Alessandro Esposito. The code for volume estimation of convex polyhedra was adapted from code distributed by Dr John Burkardt under the GNU LGPL license. Diffusion filtering was performed with the Matlab toolbox "Nonlinear Diffusion Toolbox" developed by Dr Federico D'Almeida and distributed under BSD licence.

Rendering and quantification of volumes.

Quantitative evaluation of cell volume from fluorescence images depends critically on a correct estimate of the background-to-object transition along the surface of the object whose volume is being measured. The usual assignation of arbitrary threshold isovalues for the transition is prone to error. In order to eliminate the dependence of the volume estimate on the isovalue, the isosurface was used only as an initial guess for an iterative algorithm (fit-assisted iso-surface, FAIS) that elastically deformed the iso-surface according to locally normalized thresholds. At a number of randomly selected vertices of the iso-surface, a fluorescence profile was computed along the normal to the object. The curve describing the transition profile along each normal direction was fitted by an error function. For the data shown in this work, the background-to-object transition was set at the inflexion point of the fitted sigmoid. The entire initial surface is deformed by interpolation moving the analysed vertices to their respective inflexion points. With confocal images of RBCs, best results were obtained with a first cycle of optimization selecting 2^5 vertices and a second iteration cycle using 2^7 vertices. See (Esposito et al., 2010) for additional details on the algorithm.

Results

Confocal microscopy.

Infected and uninfected RBCs from the same culture were loaded with calcein and imaged with confocal laser scanning microscopy. Serial sections of live cells embedded in low-gelling temperature agarose are shown in Figure 28. Deconvolved images are shown with no image enhancements other than colour-coding of fluorescence intensities for easing visualization. Figure 28A shows an uninfected RBC. The normal biconcave shape is apparent from the smooth boundaries of the image and from the doughnut-shaped lower and higher optical slices. Figure 28B shows a RBC containing a ring-stage parasite, and Figure 28C-D shows IRBCs with trophozoite-stage and schizont-stage parasites, respectively. The distribution of calcein in the infected cells (Figure 28B-D) is markedly heterogeneous, with intense staining of parasite structures. Calcein appears strongly associated with parasite membranes and also with parasite-derived material incorporated in the host cell membrane, as can be seen by the peripheral dotted pattern in Figure 28C-D. At this stage, the IRBC has lost its original biconcave shape and presents an irregular surface contour. Figure 48 in Appendix D shows a merozoite attached to a healthy RBC before invasion.

In Figure 28D, calcein fluorescence appears associated with parasite structures that clearly identify a mature parasite stage such as parasitophorous membrane clefts within the host cytosol. The parasite size appears small and compact, perhaps at a very early stage of schizogony. To interpret this and similar rendered images of IRBCs with mature parasites it is important to bear in mind the following points.

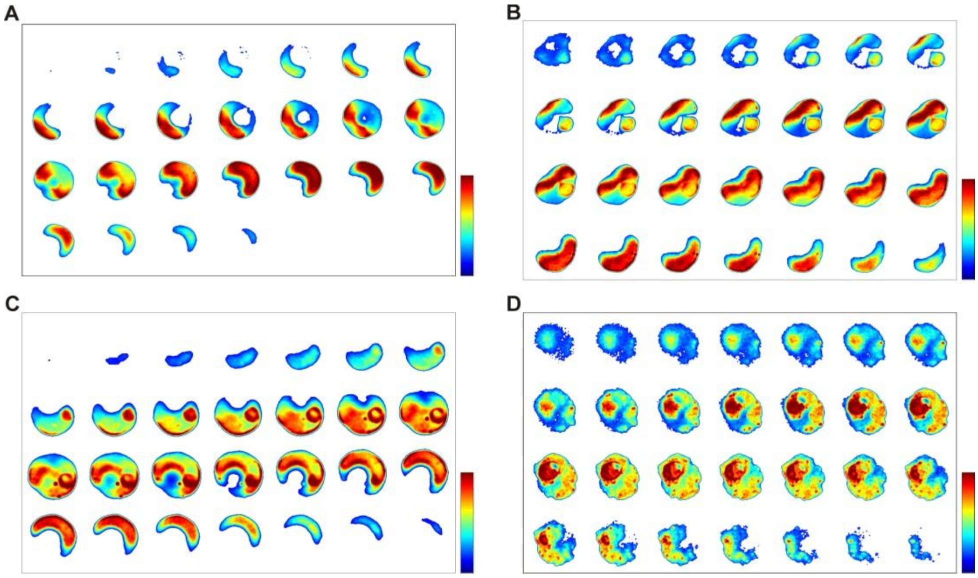

***Figure 28 : Confocal imaging of calcein-loaded infected and uninfected (cohorts) RBCs from the same culture**. A) cohort RBC, B) IRBC with ring-stage parasite, C) IRBC with trophozoite stage parasite, and D) IRBC with schizont-stage parasite. Images are representative of 119 cells analysed. Scales are shown in the right panel.*

Unlike with the calcein contained within the host cell compartment, the calcein associated with non-membranous parasite structures tended to photobleach fast during the acquisition of the 3D image stacks, with fast recovery thereafter, making the parasite appear less bright in the stacked images than when observed under the ocular before or after the dataacquisition interval. Calcein fluorescence was elicited by excitation at 488 nm, and emission was recorded between 500 and 560 nm. In the experimental conditions applied here, haemozoin autofluorescence when excited at 488 nm was largely masked by the bulk fluorescence of calcein so that the position of the food vacuole – clearly visible in transmission images (i.e. Figure 50A in Appendix D) – remained hardly detectable in the stacked images. A general caveat in the analysis of images composed over brief data-acquisition times, is that the viability of any particular IRBC cannot be fully ascertained. The normal continuity of cultures from calcein-loaded cells established before (Esposito et al., 2008) is a statistical measure and cannot be interpreted to mean that every cell under observation will experience normal merozoite egress and deliver a full complement of infective merozoites.

Volume reconstruction.

A number of stereological techniques are available for estimating cell volumes from optical sections, all of which, to a variable degree, depend on a threshold-decision process to define the contour of the object (Kubinova et al., 1999; Fang et al., 2000). Iso-surfacing, for instance, depends on the arbitrary selection of a threshold value for the contour of the surfaces to be visualized, causing significant variations in the volume estimates. On the other hand, iso-surfacing based techniques are very useful to represent the three-dimensional *morphology* of the object. To retain this advantage, and also to be able to apply iso-surfacing for estimation of both area and volume of IRBCs, it was necessary to apply a new algorithm for surface rendering which circumvents threshold derived artefacts arising from the large intensity heterogeneities from IRBCs imaged with fluorescent stains. Figure 29 illustrates the effects of noise and of the point spread function (PSF) of the microscope on the localization of a one-dimensional boundary. Different algorithms were tested on computer generated data (Figure 29, B and D, *grey circles*) using a segment of known length (Figure 29B, *d*) after applying a Gaussian PSF to a step function in the absence or presence of noise (Figure 29C-D, respectively). It can be seen that the length of the segment can be approximated by the distance between the inflexion points of the sigmoid functions used to fit the transition from background to the fluorescent object.

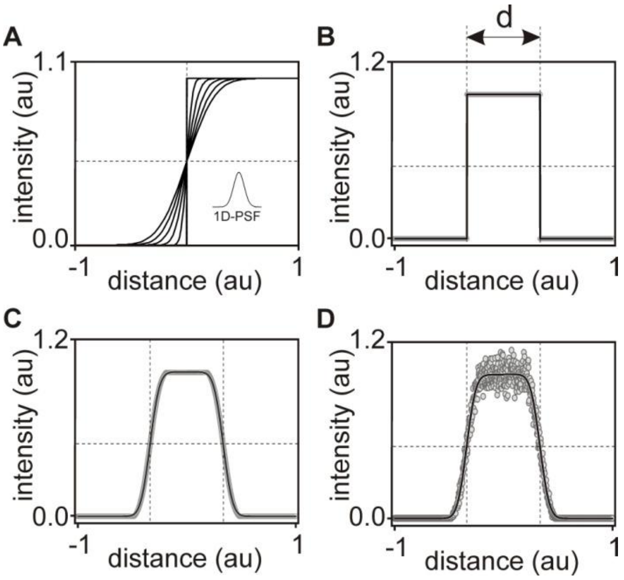

Figure 29 : Background to object transition and length estimates with the fit-assisted algorithm*. The procedure is illustrated with a one-dimensional example using simulated Fluorescent intensity versus distance diagrams; intensity and distance are expressed in arbitrary normalized units (au). A) Background to object transition: The PSF of the microscope smoothes the sharp simulated background-object transition to an extent determined by the standard deviation of the error function, illustrated here for values between 0 (steepest slope) and 1 (shallowest slope), in arbitrary normalized units. In panels B-D, boundary transitions to an object of length d are generated from computer simulations and are represented by grey circles; in panels B and C, grey circles are overlapping and result into a grey outline. The continuous curves represent the fit obtained with the fitting algorithm. B) Sharp transition; C) with blurring; D) with blurring and noise.*

Figure 30 illustrates the comparison between the fit-assisted (FA) algorithm used here and the gradient-based (GB) methods for estimating the object-to-background transition.

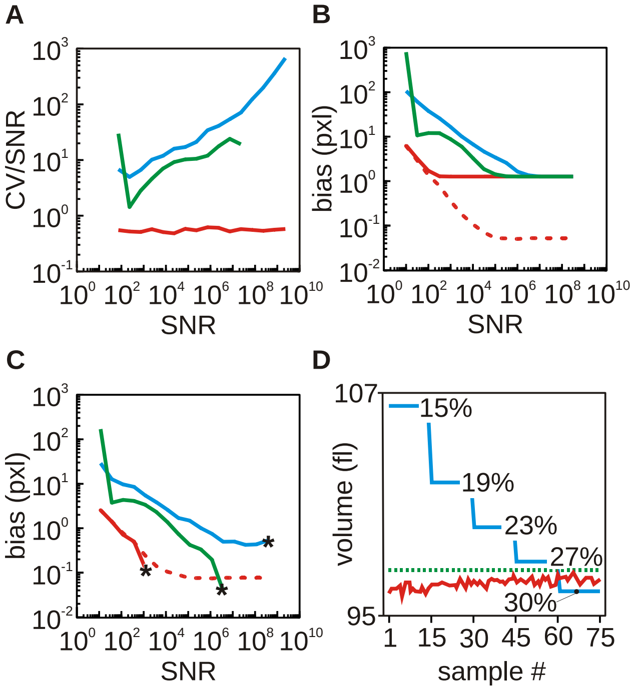

Figure 30 : Comparison between the fit-assisted (FA) algorithm and gradient-based (GB) methods for estimating object-to-background transition and object volume. *Panels A-C compare efficiencies in boundary estimates as a function of the signal-to-noise ratio (SNR) of the data set; efficiency is reported as the ratio of the coefficient of variation (CV) to the SNR. Note that lower values equal better performance. In panel D, estimated volumes (in fl) are reported as a function of the number of synthetic objects simulated (sample number). Colour codes: red, fit assisted algorithm; blue, gradient filtering; green, diffusional filtering. Dashed segments stress the superior precision of the FA algorithm for sub-pixel resolution. A) Statistical error in length estimation normalized by Poissonian noise. B) Bias in the estimate of the absolute position of the boundary. C) Bias in the estimate of the length of the simulated segment.*

D) Comparison of volume estimates on 75 different simulated three-dimensional samples by the FA algorithm (red) and by GB iso-surface rendering (blue), at different isovalues from 15 % to 30 % of the maximal intensity. The dashed green line indicates the actual volume of the simulated object. Note that the FA algorithm approximates the simulated volume better than the GB methods at all initial threshold values.

The traditional GB techniques rely on the analysis of gradients after smoothing with a Gaussian kernel ("MAXD1" technique in (Sieracki et al., 1989), *blue curves*) or after diffusion filtering (*green curves* ((Malm et al., 2000; Tabik et al., 2007), adaptive)). The signal-to-noise ratio (*x-axis*, SNR) is the total number of photons generated in a computer-simulated data-set like the one used for Figure 29. The lines in Figure 30A compare the precision with which the FA and GB methods estimate the length of an object. The coefficient of variation (CV) of the segment length was normalized with Poissonian noise (*i.e.*, the inverse of the square root of the number of collected photons). It can be seen that the normalized CV of the FA-computed algorithm remains optimized at all SNR whereas that of the GB algorithms increase with SNR, therefore decreasing in relative efficiency at higher SNR values. The improved efficiency of the FA method results from the use of the full information content of the data-set whereas GB methods use only the photons in the neighbourhood of the boundary.

Optimal precision for segment length is approached at sufficiently high SNR (Figure 30, B and C). Given the pixelated nature of the images, optimal resolution with the FA method is achieved with ~ 10^3 photons whereas the GB methods require >106 photons for an equivalent resolution of object length (Figure 30C, see "★"). Moreover, the FA algorithm can deliver sub-pixel resolution for both absolute position of the object boundaries and for measurement of object length (Figure 30, B and C respectively, *dashed red lines*); this was tested by positioning the object transition in the middle of two sample pixels and by plotting the FA results without rounding up the values to the nearest pixel.

Figure 30D shows numerical volume estimates on synthetic data as a function of sample number. Seventy five synthetic objects generated by simulations in the presence of noise were analysed by applying an increasing threshold for isosurfacing (from 15 % to 30 % of the maximum intensity value), which resulted in a decrease of the volume estimates (Figure 30D, *blue curve*). On the other hand, the fit assisted iso-surfacing (FAIS) algorithm (*red curve*) rendered values close to the set “true” value (*green dotted curve*) at all initial thresholds. Figure 49 in Appendix D illustrates the robustness of this approach in three-dimensional rendering of highly irregular objects.

Morphology, volume and area estimates of infected RBCs.

Cohort RBCs (healthy RBCs from same culture than IRBCs) and cells infected with parasites at different stages of development were imaged and analyzed using the FAIS algorithm. The results of representative transmission and fluorescence confocal images, together with the treedimensional images reconstructed using the FAIS algorithm, are shown in Figure 31. Cohort RBCs exhibited the typical biconcave shape (Figure 4A), not much perturbed at the ring-stage (Figure 31B).

At the trophozoite and schizont stages (Figure 31, C-E) IRBCs show progressive surface deformations with irregular bulges.

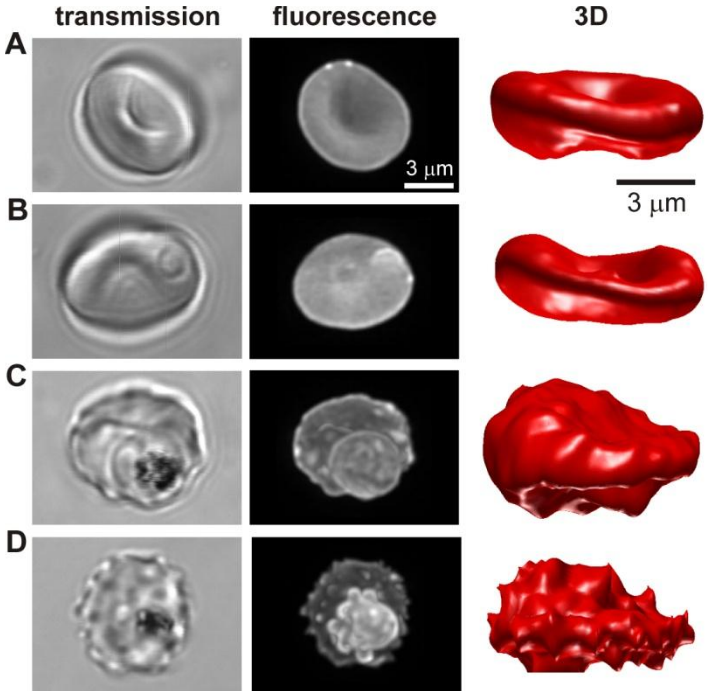

Figure 31 : Transmission, confocal and 3D images of a cohort cell (A), ring-stage IRBC (B), trophozoite-stage IRBC (C) and schizont-stage IRBC (D and E). *Fluorescence images are maximum intensity projections of the deconvolved confocal 3D image stacks. The selected images are representative of a total of 119 cells analysed. Panels D and E show typical phenotypes exhibited by schizont-infected RBCs.*

The spiky appearance of the surface (Figure 31D) in about 60% of the calcein-reconstructed images is a software-rendered 3D interpretation of the membrane bulges and irregularities clearly visible in the corresponding transmission images and fluorescence projections (Figure 50A in Appendix D). At the optical resolution of the confocal microscope the fine structure of the bulges is not resolved. Those that appear like spikes may correspond to the membrane projections more clearly seen in serial sections obtained at electron-microscopical resolution (illustrated in Figure 50B (Lew et al., 1988; Lew and Hockaday, 1999)). A fraction of such membrane projections and folds may represent a small reservoir of membrane area undetectable at optical microscopy resolution. What is clear is that the spikes do not reflect classic surface crenations and cannot be described as such. Volume estimates were obtained from a total of 119 cells (44 cohorts and 75 IRBCs) and the results, normalized to the mean of the uninfected cohorts, are shown in Figure 32A. In this figure, the volume histogram is superimposed on model simulations for comparisons between measured values and model predictions, analysed in the Discussion section of this chapter. The variation in normalized results is reported as standard deviation instead of standard error of means, because the statistical variation encompasses some asynchrony in the choice of imaged cells representing each developmental stage and natural phenotypic polymorphisms, as well as measurement noise. Any difference of minor statistical significance has therefore no value in such a sample. The actual volume of the uninfected cohort RBCs was 88 ± 20 fl (mean ± SD), well within the range for normal human RBCs. The volume of all cells relative to the cohort mean was (mean ± SD, n = number of cells): cohorts, 1.00 ± 0.22, $n = 44$); ring stage IRBCs, 0.94 ± 0.14, $n = 19$; trophozoite-stage IRBCs, 1.17 ± 0.29, $n = 42$; schizont-stage IRBCs, 0.92 ± 0.09, $n = 14$. The statistical significant differences were a 17 % increase in volume between uninfected RBCs and trophozoites ($p < 0.01$, t-test) and a 22 % volume reduction between trophozoite- and schizontstage parasites ($p < 0.001$). The surface area of cohort RBCs was 120 ± 15 μm2. The relative area estimates on all cell samples were (mean ± SD, relative to cohorts) 1.00 ± 0.12 for cohorts, 0.92 ± 0.07 for ring-stage IRBCs, 0.99 ± 0.12 for trophozoite-stage, and 0.82 ± 0.11 for schizont-stage IRBCs; the difference between the last two, of about 18%, was statistically significant ($p < 0.001$).

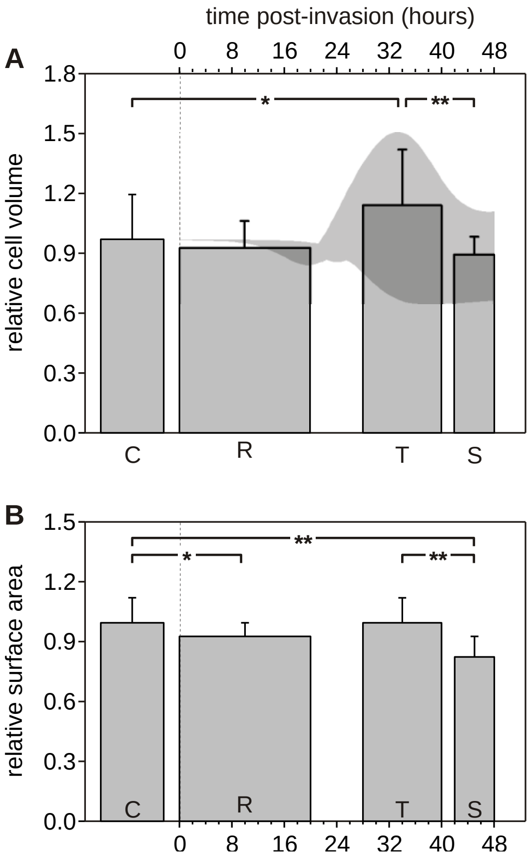

Figure 32 : Volume and area estimates of infected-red blood cells with parasites at different stages of development. *Volume (panel A) and area (panel B) values are normalized to the corresponding means in the uninfected cohort RBCs (column C). The columns report mean ± SD. Column width reflects the probable time interval for each parasite developmental stage as selected by the criteria described in Methods. R: rings; T: trophozoites; S: schizonts. Horizontal lines above columns report statistical significance of differences between indicated groups; *:* $p < 0.01$*; **:* $p < 0.001$*. The shadowed area in the top graph reports a subset of data from the malaria model (Chapter 2) and (Mauritz et al., 2009). Its significance is analysed in the Discussion section of this chapter.*

Discussion

The aim of this study was to provide a reliable quantitative estimate of the volume and area of red blood cells infected with single *P. falciparum* parasites at different developmental stages. The results showed that the volume of IRBCs remains within a narrow margin of variation relative to that of uninfected cohorts throughout the reproduction cycle of the parasite, confirming earlier results by Allen and Kirk (Allen and Kirk, 2004), Saliba et al. (Saliba et al., 1998), Elliot et al. (Elliott et al., 2001) and of Park et al. (Park et al., 2008). The main statistically significant differences were found between trophozoite and schizont stages (Figure 32) amounting to a volume reduction of about 22 % and an area reduction of about 18 %.

The fit-assisted iso-surfacing algorithm applied here allowed volume and surface area quantification eliminating user- and threshold-dependent biases present in the analysis of heterogeneous irregular objects with other methodologies. Furthermore, the algorithm enabled fitting object boundaries at sub-pixel resolution (Figure 30, B and C). With this level of precision (Figure 30), the observed variations in volume and surface area can confidently be attributed to genuine variations in phenotype and developmental stage. These variations are relatively large, with coefficients of variation ranging from 10 to 25 % for volumes, and from 8 to 13 % for areas (Figure 32). How do these results contribute to clarify the volume-area controversies in relation to the colloidosmotic hypothesis?

As previously analysed (Lew et al., 2003; Lew et al., 2004), the increasing osmotic fragility of IRBCs with late-stage parasites reflects a predisposition of IRBCs to lyse on rapid volume expansion. If, as confirmed by the present results, the volume of IRBCs within the range of observed variation remains confined well below the critical haemolytic volume of uninfected cells, then either the membrane area is reduced or the membrane structure is altered so that, on volume expansion during osmotic fragility measurements, the membrane permeability barrier becomes disrupted before the cell attains its maximal spherical configuration, or both. The present results suggest that there is a significant loss in membrane area, averaging 18 %, between schizont and trophozoite stages (Figure 32B), supporting earlier estimates of late membrane area losses (Zanner et al., 1990). It is worth pointing out, however, that our estimate represents an upper limit by this method because the measurements cannot detect submicroscopic membrane folds constituting a potential reservoir of membrane area.

To what extent could the maximal estimated area loss account for the observed increase in osmotic fragility? A fractional reduction f in the membrane area of a cell will reduce its maximal spherical volume by $(1 - f)^{3/2}$ amounting to a mean reduction in critical haemolytic volume of about 26 % for $f = 0.18$. Could membrane area loss fully account for the large increase in osmotic fragility of IRBCs with late-stage parasites? Approximate estimates (see Appendix D) suggest that 18% area loss may account for osmotic fragility shifts of up to about 0.7 relative tonicity, a substantial increase over the 0.45-0.50 mean value for uninfected RBCs. However, significant fractions of late-stage IRBCs lyse at relative tonicities of 0.8-0.9 (Lew et al., 2004). Therefore, although membrane area loss may be an important contributor to the observed increase in osmotic fragility, it is very likely that structural membrane alterations also play an important role. One could therefore conclude that the increased proximity of IRBCs to a critical haemolytic volume exposes a progressive vulnerability to lysis by volume expansion; this is then counteracted by the reduction in osmolyte concentration within the host cell cytosol resulting from excess haemoglobin consumption. Proximity to the CHV, rather than the actual volume of the IRBCs, is thus the critical condition for the validity of the colloidosmotic hypothesis.

What relevance do the present results have for our understanding of IRBC homeostasis? The shaded area in Figure 32A frames the results of simulations using the IRBC homeostasis model with a subset of parameters selected to fit best the observed volume variability. This subset constrains the range of likely homeostatic parameter values during the asexual reproduction cycle of IRBCs with single parasites. The defining parameter of this subset, with a value of 0.3, is the coupling factor that relates parasite volume growth to haemoglobin consumption (Mauritz et al., 2009), and which renders mature parasites volumes in the 30-50 fl range in agreement with previous results (Saliba et al., 1998; Elliott et al., 2001; Park et al., 2008). With this value for the coupling factor, the shaded area in Figure 32A covers variations in the half-times for NPP development and haemoglobin consumption of 27 ± 5 and 32 ± 6 h, respectively, corresponding to the experimentally reported values for a ±1SD statistical variation in these parameters (Mauritz et al., 2009). These variations may be reinterpreted as reflecting genuine heterogeneity in parasite development in the culture conditions from which the analysed samples were harvested. A salient feature of the shaded profile in Figure 32A is the biphasic volume pattern apparent in the top outline. The results support a statistically significant reduction in IRBC volume of about 22% between trophozoite and schizont stages. The model parameters that conform with that profile generate a sequence in which the large early NaCl and water gains by the host after NPP development are followed by volume decrease due to late haemoglobin consumption exceeding late NaCl and water gains at a stage when sodium gradient dissipation has minimized the driving force for further net NaCl influx (For the documented K^+-selective new permeation pathway (NPP) with permeability ratio $P_K/P_{Na} = 2.3$ (Staines et al., 2001)). In conclusion, the results presented here, using a new algorithm for the quantitative measurement of volume and surface area of irregularly shaped cells, show that the volume of *P. falciparum* parasitized RBCs varies little from that of uninfected red cells (Saliba et al., 1998; Elliott et al., 2001; Park et al., 2008). The direct non-invasive volume measurements of IRBCs agree well with the volume predictions of the IRBC homeostasis model corrected down for realistic parasite volumes (Elliott et al., 2008). This work resolves the conflict between earlier volume estimates (Allen and Kirk, 2004; Lew et al., 2004) and adds further support to the view that the increase in osmotic fragility of IRBCs with late-stage parasites can be attributed to both a reduction in host-cell membrane area and an increased vulnerability to pre-spherical lysis on volume expansion. The next chapter is therefore concerned with the investigation of the changed cytomechanical properties of IRBCs.

Chapter 6: Detection of *Plasmodium falciparum*-infected red blood cells by optical stretching

Introduction

Malaria infection is accompanied by severe changes in the mechanical properties of the infected host RBCs, leading to a reduced capability of blood to circulate through narrow capillaries, which in turn can lead to lethal complications (Miller et al., 1971; Miller et al., 1972; Cranston et al., 1984; Nash et al., 1989; Miller et al., 1994). It is not yet fully understood how the change of cell elasticity occurs, but it is attributed to the integration of parasite proteins to the erythrocyte membrane such as KAHRP and *Pf*EMP3 and to conformational changes in the cytoskeleton of the RBC (Glenister et al., 2002). A precise assessment of the mechanical properties of infected red blood cells (IRBCs) is thus essential for an improved understanding of the disease, for the assessment of potential treatments, and for improved diagnostic purposes. At the single-cell level, optical tweezers and magnetic traps offer powerful tools for precise measurements of cell compliance (Suresh et al., 2005; Marinkovic et al., 2009). Passive methods include the observation of cell membrane fluctuations or the passage of individual cells through constricting flow channels (Shelby et al., 2003; Park et al., 2008). These methods have either low throughput efficiencies or are limited in the information they yield. They are also difficult to be implemented into online diagnostic tools. Bulk methods such as ektacytometers have a fast acquisition, but deliver only ensemble measurements (Cranston et al., 1984). In addition, where one deals with small subpopulations of IRBCs amongst many uninfected cells, ensemble measurements are liable to false negative results. This chapter reports on the development and use of a novel haematological tool for the detection of IRBCs, a microfluidic optical stretcher, tested in *Plasmodium falciparum* (*Pf)* cultures. It is shown that the technique is well-suited for the quantification of alterations in the mechanical properties of RBCs during early stages of infection. The method combines the sensitivity of traditional single-cell measurement techniques with the potential for high throughput analysis.

The optical stretcher can determine IRBC compliance in a non-contact mode and with high throughput (Guck et al., 2001; Lincoln et al., 2007). Rather than attaching dielectric beads as handles to the cells of interest and moving them apart with two parallel and tightly focused laser beams, as used in optical tweezers experiments, the optical stretcher traps cells directly between two divergent counter-propagating laser beams (Ashkin, 1970; Constable et al., 1993). Figure 33 illustrates the schematics of an optical stretcher. It consists of a capillary into which light is delivered via two opposing optical fibres.

It is possible to stretch a trapped cell along the axis of the laser beams by simply modulating the light intensity (Guck et al., 2001). The stretching forces are generated by the momentum transfer that occurs at the interface between the sample cell and the surrounding medium due to a change in refractive index (Guck et al., 2000). These surface forces pull the cell apart, analogous to a tug-of-war situation. The resulting stretching force can be 1-2 orders of magnitude larger than the net trapping forces, the latter arising from the asymmetric force field for cells positioned slightly off the centre in the trap (Guck et al., 2001). Spheroidal cell shapes greatly facilitate theoretical modelling (Guck et al., 2000; Wei et al., 2006; Boyde et al., 2009; Ekpenyong et al., 2009; Xu et al., 2009), and consequently the only quantitative measurements of erythrocyte mechanical properties with the optical stretcher have been performed on osmotically swollen erythrocytes (Guck et al., 2001; Liu et al., 2006).

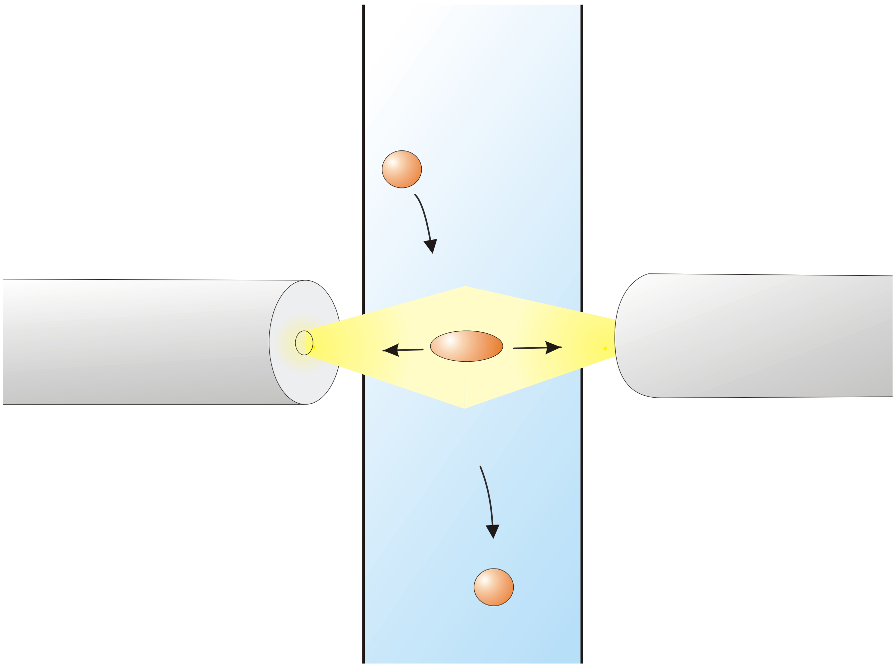

Figure 33 : Schematics of an optical stretcher. *Two opposing divergent light beams create an optical trap, which can stretch dielectric specimens such as biological cells. A capillary delivers the cell suspension into the trapping region.*

For the present problem of determining erythrocyte compliance in a physiological state, i.e. in a variant of a biconcave-disc-like shape, the analysis of surface forces becomes more involved, but is tractable in principle using finite element method (FEM) calculations (Yu et al., 2005). An alternative approach, taken here, is to employ a simplified phenomenological model to quantify the cell compliance. Here the simple Kelvin-Voigt model is used, assuming only a global viscosity η and elasticity constant E for the whole cell. According to this model, the strain $\varepsilon(t)$ following an instantaneous constant stress σ can be described as:

$$\varepsilon(t) = a \cdot [1 - \exp(-\lambda t)], \tag{7}$$

where $\lambda = E \cdot \eta^{-1}$ is the characteristic deformation rate and $a = \sigma \cdot E^{-1}$ the relative amplitude of the stretch. In the literature, values of λ in the range of 5 – 16 s^{-1} have been reported for uninfected RBCs (Hochmuth and Waugh, 1987; Liu et al., 2007).

Optical stretching is used to observe the mechanical alterations in RBCs upon malaria infection, comparing them to uninfected cells of the same culture (cohort cells) and control cells that have never been exposed to *Pf*. Optical stretching delivers the sensitivity and selectivity of single-cell compliance measurements in a contact-free fashion that is suitable for future high-throughput applications, thus combining both advantages in one technique.

An ancillary advantage is that the layout of the optical stretcher allows future combination with other multiparametric imaging approaches performed simultaneously and can thus link mechanical information with subcellular phenomena (Elder et al., 2006; Elder et al., 2006; Frank et al., 2007; Kaminski et al., 2008; Elder et al., 2009; van Ham et al., 2010).

Optical Forces: Historical and Theoretical Background

Light forces have been discussed in the sciences for a long time: Johannes Kepler expressed the concept of light exerting force on matter as early as 1619 (De Mairan, 1754). He observed that the illuminated tails of comets, consisting of fine dust and gases always pointed away from the sun and deduced that a radiation pressure must be exerted upon them by the incident light. It was not possible until much later to produce laboratory conditions to test this hypothesis, the main problem being thermal interactions with ambient gases. In 1873, after Maxwell had quantified electromagnetic waves, he was able to theoretically deduce a radiation pressure that should be perpendicular to the wave (Maxwell, 1873). Bartoli arrived independently to the same conclusion in 1876, only considering the second law of thermodynamics (Bartoli, 1884). Peter Lebedev has measured this radiation pressure for the first time in 1900 (Lebedev, 1901), although only the 1901 experimental confirmation of Nichols and Hull became famous: a torsion balance, where two mirrors (vanes) are hung on a fibre in a vacuum chamber (Nichols radiometer). They observed the fibre twisting upon illumination and derived the size of the radiation pressure from that angle (Nichols and Hull, 1901; Bell and Green, 1933). The thermal interactions with the gas molecules were reduced by performing the experiment in a 21 mBar vacuum and also taking into account the non-reflecting sides of the mirror: The momentum transferred to the surface of the vanes from a perfectly reflected light beam should be two times than that of a completely absorbed beam. Nicholas and Hull also showed that rotation of the classical light mill (Crookes radiometer from 1873 (Crookes, 1874)), where several vanes with a black and a bright surface mounted on a spindle is mainly due to the heating of gas molecules and not by the radiation pressure, although it is still today used as an example for optical momentum transfer in undergraduate lectures. The advances in vacuum and illumination technology have greatly increased the quality of modern experimental setups: in 1970, after the invention of the laser which delivered much higher energy densities, Arthur Ashkin managed to trap and accelerate micron sized particles (Ashkin, 1970). His discovery was made by observing accidentally trapped bacteria in a focused laser beam that had developed in the water over the time course of his experiments. His scientific vision of that time was to develop single atom light traps (with an illumination arrangement termed “optical molasses”) which was a prerequisite to develop the magneto-optical atomic trap (by H. Dehmelt and W. Paul, Nobel Prize in Physics, 1989) for extreme ion cooling.

The use of radiation pressure in biophysical applications only developed later and is still a very active research area. Optical manipulation of single cells has been demonstrated for the first time in 1987 (Ashkin and Dziedzic, 1987). The most widespread use nowadays certainly is the optical tweezer, a single beam gradient trap, for translating cells and other micron sized objects under a microscope. The tweezer consists of a single (focused) beam trap, but by fast multiplexing (directing the laser focus to several positions, one light source is time-shared for several traps) it is possible to receive multiple traps from one light source. Combined with laser ablation (optical scissors) these already provide powerful tools for studying living cells such as measuring forces exerted by molecular motors such as myosin or kinesin (Block et al., 1990), or the swimming forces of sperm (Tadir et al., 1990), and for studying the polymeric properties of single DNA strands (Chu, 1991).

The optical stretcher constructed here consists of two opposing, divergent laser-beams, a configuration similar to what Ashkin implemented in the first optical trap (Ashkin, 1970). The stretching properties of the two-beam trap were only later noticed (Guck et al., 2001). Nowadays the light delivery is usually implemented in fibre optics which allows the whole setup to be integrated into a microcapillary (Lincoln et al., 2007). Mechanical measurements on other nucleated cells for detection of malignant transformation (Guck et al., 2005; Remmerbach et al., 2009) and differentiation (Lautenschlager et al., 2009) using the optical stretcher have been demonstrated previously.

The theoretical effort of explaining trapping and stretching can be done in two ways, equivalent to the different regimes in wave optics and ray optics: The Rayleigh regime is used when the object is much smaller than the wavelength of the trapping light, such as atoms and molecules. The optical forces can than shown to be (Ashkin and Dziedzic, 1987; Ashkin, 1992):

$$< |\boldsymbol{F}| >= \frac{\alpha}{2} \nabla < E^2 >. \qquad (8)$$

When the object is bigger than the wavelength used (Mie regime) it is sufficient to use ray optics when calculating optical forces (Ashkin and Dziedzic, 1987). Light waves or photons carry angular and linear momentum, of which only the latter is of interest here. The (relativistic, linear) momentum is dependent on the index of refraction of the medium in which the light travels. One can trap and stretch a micron-sized object, if its index of refraction is higher than that of the surrounding medium. In this case the linear momentum of the light is increased in the object: $|\boldsymbol{p}| = n \cdot E \cdot c^{-1}$, where n is the index of refraction of the medium, p the linear momentum, E the energy of the incident ray and c the speed of light in vacuum (Ashkin and Dziedzic, 1973).

This momentum change is conserved by the object, which in turn induces an equal momentum opposite in direction on it and exerts a force upon it (Newton‘s laws):

$$|\boldsymbol{F}| = |\dot{\boldsymbol{p}}| = P \cdot \Delta n \cdot Q \cdot c^{-1}, \qquad (9)$$

where Δn is the difference of the refractive indices at the interface and P the light power. Q is a factor that is unity for absorption and two for reflection of the light. The reflectivity of cells is usually quite low, $R \approx 10^{-3}$, while the refractive index for a RBC is n_{RBC}=1.378 (Evans and Fung, 1972; Park et al., 2008) and thus higher than that of water, n_{water}=1.33 (both values measured at $\lambda \approx 550$ nm (Jackson, 1975; Guck et al., 2001).

Ray optics has the advantage of being intuitively accessible, Figure 34A and 34B illustrate the trapping in a single-beam gradient trap by the momentum change of the scattered rays.

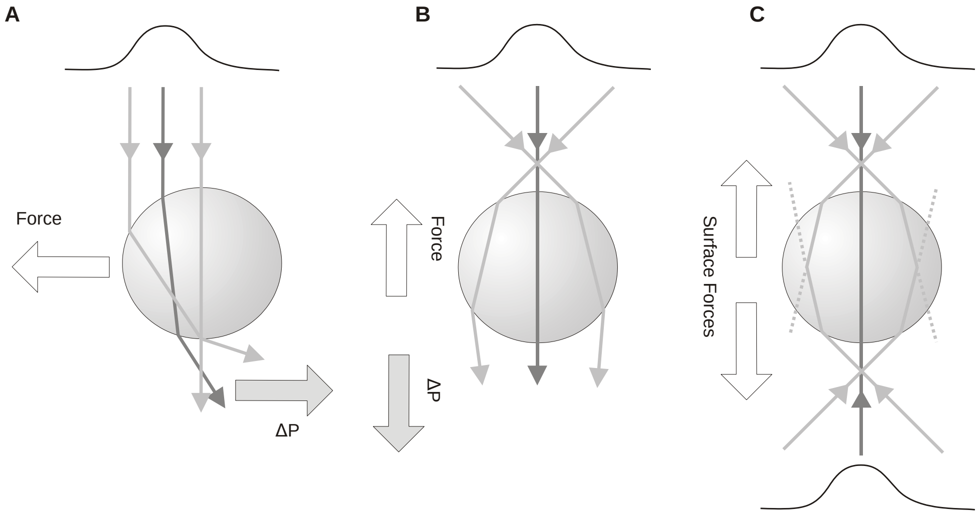

Figure 34: Working principle of optical trapping and stretching. *The relative intensity of incident light rays is indicated by the curves above the panels.* ***Panel A*** *shows a cell slightly off-centre horizontally from the highest intensity of the light beam. The refraction of the rays changes their momentum and induces an opposite force on the cell, pulling it back into the higher intensity region.* ***Panel B*** *sketches a similar situation, now the cell is vertically out of the focused beam. The refracted rays induce a net momentum change pointing away from the focus, which induces an opposite force, again towards the focus.* ***Panel C*** *outlines the concept of the optical stretcher as a dual beam trap. Two focused beams create traps slightly above and below the cell. As a result of both attractive forces, the cell surface stretches in this "tug-of-war" like situations. The implementation of the optical stretcher in fibre optics uses divergent beams, the two "virtual" trap foci are effectively within the fibre.*

The dielectric sphere acts itself like a small lens, and pulls itself back into the focus of the incident beam due to the momentum transfer. The actual calculation of force profiles has to integrate over all incident angles. In a setup with two opposing beams, the cell is attracted to both focal traps.

Eventually it is trapped at the equilibrium point, in the middle between the two focal spots. This results in a tug-of-war like situation between the two traps, illustrated in Figure 34C, which creates surfaces stretch forces on the steadily trapped cell proportional to the intensity of the incident light beam. The stretching forces are in the range of up to several hundred pico-Newton and fill the gap of applicable forces between the force range of optical tweezers and atomic force microscopes. Optical stretching of osmotically swollen RBCs was performed at laser powers up to 800 mW, while trapping could already be achieved at 10mW. A stress of up to $\sigma_0 = 2Nm^{-2}$ (P~500 mW) invokes a linear response in these swollen RBCs, beyond which the cells can be irreversibly deformed (Guck et al., 2001). As mentioned earlier, IRBC stiffness is greatly increased compared to healthy RBC and detecting these differences should be accessible by the optical stretcher.

Materials and Methods

Development of the experimental setup.

Cell viability is of concern in any optical trapping experiment. Optical damage has been shown to greatly depend on the wavelength of the used light, with a minimum of biological damage found at a wavelength of 930nm and above (Liang et al., 1996; Neuman et al., 1999). Hence modern optical traps typically employ near infrared light. The 1064 nm line of Nd:YAG proved to be a compromise between apparatus cost and cell viability and is widely used in biological applications.

In this project a polarised, continuous wave Yb-doped fibre laser was selected that delivers up to 5 W peak power at a wavelength of 1070 nm (YLR-LP-5 from IPG Photonics, Oxford, MA, USA). A polarisation mainaining laser was selected to prevent drift of spontaneous light polarisation, which could disturb trapping stability. The optical fibres used were PANDA polarization-maintaining single-mode fibres (PM980-XP, Nufern Ltd., East Granby, CT, USA). The laser light was split 50/50 in a polarization-maintaining Y-fibre beam splitter (Gould Fiber Optics, Millersville, MD, USA). As standard mechanical fibre connectors do not allow for the delivery of high laser powers (at $P_{cw} > 500mW$ the heating of the connector due to dissipated energy from coupling losses becomes problematic) the optical fibres were fused where necessary. Fusion splicing for connecting the laser, beam splitter and the delivery fibres (illustrated in Figure 35) was performed in a four dimensional (x, y, z, θ) fibre-splicer (FSM-20PMII, Fujikura Ltd., Japan) for polarisation maintaining fibres.

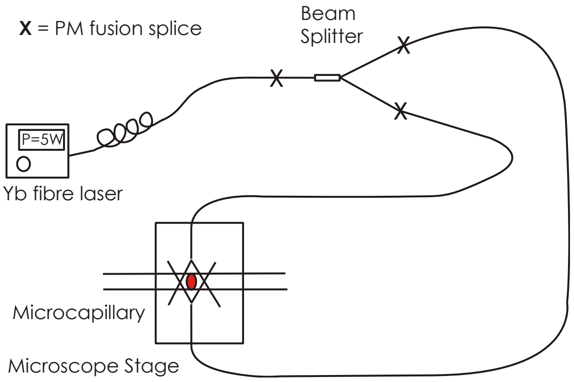

Figure 35 : Optical wiring of the stretcher*, indicating the fusion splices (crosses) for the delivery of the high laser power through the optical fibres.*

Two different approaches for the mechanical integration of the stretcher into a conventional microscope were tested. The initial idea was to build a versatile setup, employing mechanical translation stages for holding the fibres. The two fibres could then be spatially aligned before each use. A special mounting stage would hold the capillary and give access to the fibre on the translation stages horizontally and the microscope objective and illumination light source vertically. Figure 36A shows the construction plan of a mounting stage that enables these features, together with a photo of the final setup (Figure 4B).

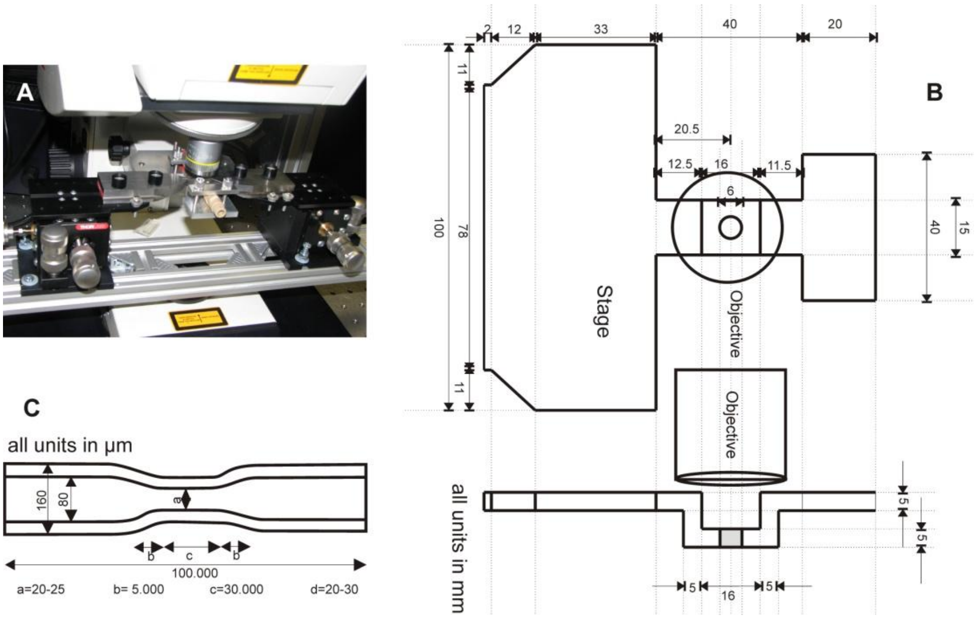

***Figure 36 : The adjustable optical stretcher. Panel A** shows the system integrated into an upright microscope (Leica Microsystem GmbH, Wetzlar, Germany) where the optical fibres are held and aligned by three-dimensional translation stages (MBT616, Thorlabs Ltd., Ely, UK). **Panel B** shows the construction plan for the microscope stage (top and side view), allowing access for the microscope objective (top) and illumination (bottom), the capillary and the two optical fibres (access from all four sides, which restricts the design severely). **Panel C:** Sketch of custom pulled capillaries allowing flow-focusing of cells.*

Tapered capillaries were custom made (by heating and pulling, courtesy of Marta Ziemienczuk, Max Planck Institute for the Physics of Light, Erlangen, Germany), enabling the focusing of the cells in the middle of the flow (Figure 4C). After initial testing of this setup, it was noticed that this design was quite impracticable: after numerous attempts to mount the (very fragile) capillary, it usually was too dirty (dusts and fingerprints) for imaging or broke when changing the tubing/flanging for attaching the cell reservoirs. A more robust setup is described in the literature and this was adapted for the malaria experiments (Lincoln et al., 2007; Lincoln et al., 2007). The drawback of this construction is that the alignment of the fibres and the capillary is fixed and cannot be changed ad-hoc. The fibres and the capillary are supported and aligned by a cross-shaped photolithographic pattern on a glass slide (illustrated in Figure 37A).

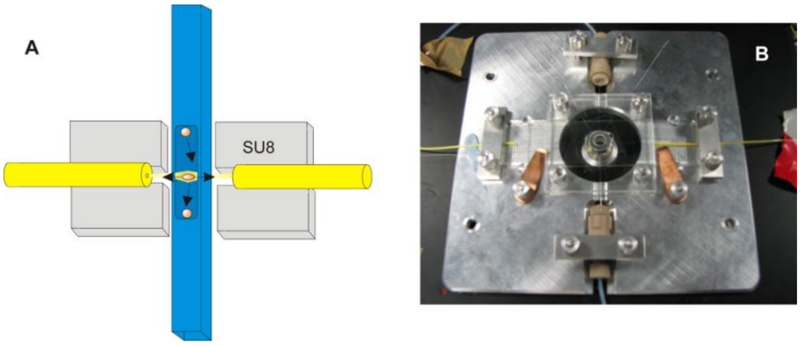

Figure 37: The static optical stretcher. *Panel A shows the schematics of the relevant structure. It consists of a SU-8 polymer layer adhering to a microscope glass slide. This structure clamps the optical fibres precisely aligned in grooves that are smaller in diameter than the optical fibres. It also holds the capillary loosely. Panel B: Photograph of the fully mounted stretcher apparatus. The brown flanges hold the 200 µm capillary. The optical fibres can be seen protected in yellow plastic before entering the apparatus from the sides. The microscope objective can be seen below the Perspex cover in the imaging hole of the metal stage.*

This is clamped down after covering it with a layer of transparent silicone, a microscope cover glass and a perspex (PMMA) cover with a hole for imaging. The layers were optically homogenised by spreading index-matching gel between the interfaces, in order to reduce reflections or aberrations of air gaps. For this second setup, the flow capillary was purchased (Vitrocom Ltd., Mountain Lakes, NJ, USA), to ensure a more accurate fitting within the integrated device. It had a square profile with an inner diameter of 100x100 µm^2 and a wall thickness of 50 µm. The flow capillary was connected with tubing and fittings (Upchurch Scientific, Oak Harbour, WA, USA) to two Eppendorf reservoirs that hold the cells and a four-way valve between the two reservoirs to inject new cell suspension. The fully mounted device on the custom made microscope stage is pictured in Figure 37B.

The laser beams were arranged to enter and cross the capillary 15 µm above its bottom wall. This off-centre arrangement, which is lower than in designs described before (Lincoln et al., 2007; Lincoln et al., 2007), became necessary due to the rapid sedimentation of the uninfected RBCs to the capillary bottom, where they lay flat (1.5 µm height), and would otherwise not have been picked up by the optical trap. (This became only clear after several unsuccessful attempts with an arrangement where the light beams entered the capillary at the centre of the capillary wall).

The fibre and capillary support was made from SU-8 2025 negative photoresist (MicroChem Corp., Newton, MA, USA). SU-8 is an epoxy-based polymer that can be spin-coated and then patterned by standard photolithographical methods (see Figure 38). Polymerized SU-8 (Figure 38D) forms mechanically durable and optically transparent structures.

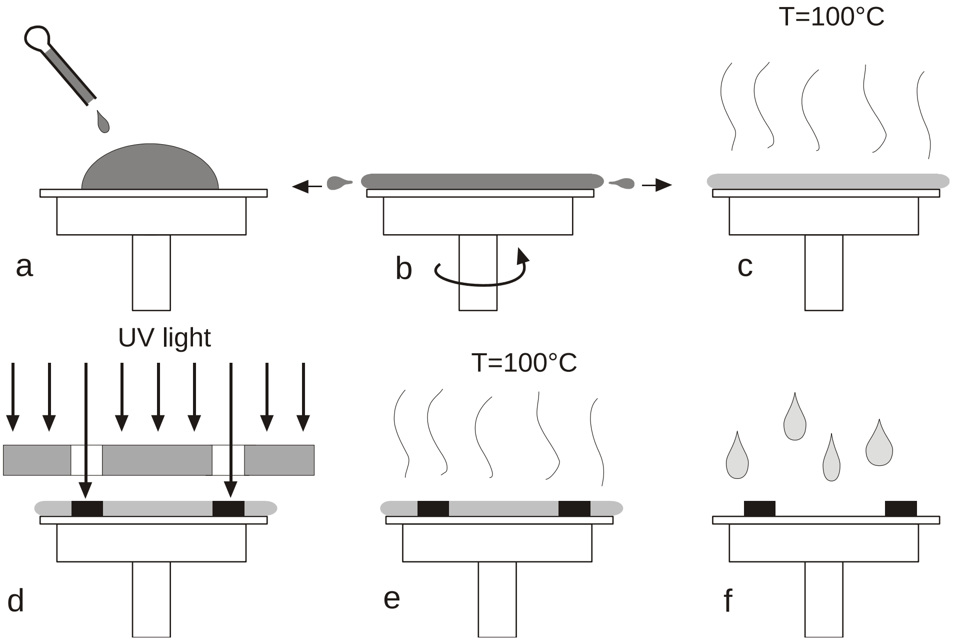

Figure 38: SU-8 Photolithography. *The experimental procedure for producing an SU-8 structure begins with* ***(a)*** *applying the resist to the substrate (here a microscope glass slide).* ***(b)*** *The resist is spread thinly on the substrate by spin-coating. The layer height is determined by the spinning speed, duration and viscosity of the resist.* ***(c)*** *The solvents in the resist are removed by baking.* ***(d)*** *The photoresist layer is partly exposed to UV light through a masc. The exposed parts cross-link and form the desired structure.* ***(e)*** *Baking the specimen after exposure ensures that feature edges will be fully developed, as the cross-linking reaction can now diffuse into regions where destructive interference of the UV light did not fully expose the resist.* ***(f)*** *The unexposed photoresist is removed by a wash in ethyl lactate.*

The SU-8 structure is produced on top of a standard microscope glass slide. Figure 39 shows one of the mask patterns used for the UV treatment of the photoresist following the design used by Bryan Lincoln for his PhD thesis at the University of Leipzig (Lincoln, 2006). This pattern consists of four transparent rectangles (drawn with AutoCAD, AutoDesk Inc., San Rafael, USA and printed on a transparency at Circuit Graphics Ltd., Southend on Sea, UK). The distance between the rectangles defines the channel width. The channel height is determined by the type (viscosity) of SU8 photoresist and the preparation protocol (spinning speed, baking and exposure times).

The shorter, vertical channel is meant to straighten and limit the movement of the rectangular glass capillary that is to be inserted, so the final width of it should be approximately 20% bigger than the mean outer capillary diameter. The longer, horizontal channel is meant to support the two optical fibres that oppose each other (compare also Figure 37A).

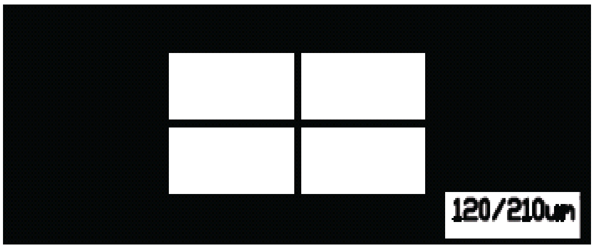

Figure 39 : Photolithographic Mask *used for irradiating the SU-8 structures. Several masks with different channel widths have been tested, as their nominal widths did not always coincide with the real ones (high precision printing was performed at Circuit Graphics Ltd., Southend-on-Sea, UK). N.B.: The text on the mask is not a scale bar, but a label of the channel widths for distinguishing samples.*

In contrast to the glass capillary which rests on the glass slide, the optical fibres should be merely supported and locked by both edges of the channel, such that the optical fibre bottom does not touch the glass slide. The size of the trapping region can be calculated with geometrical optics by using the translating and refraction matrices method (Meschede, 2005). For the desired configuration a beam waist radius of 14 µm is estimated, when the fibres are 20 µm away from the capillary wall (calculations in the appendix). The lithographic template developed for these experiments was designed to set the laser beam axes close to the capillary base (the design approached the spatially-limited height of 12.5 µm, when both capillary and optical fibre lay flat on the glass). The square capillary has an outer diameter of 200 µm ± 10% which is why the SU8 patterns are envisaged with a capillary channel width around 220 µm to ensure fitting. From geometric considerations (see also Figure 40A) the fibre channel height h to width w relates as:

$$h = d + c - \sqrt{r^2 - (w/2)^2}, \tag{10}$$

where r is the fibre radius (62.5 µm), d the laser beam centre to capillary bottom distance and c is the capillary wall width. This relation and the condition of a low beam height, $12.5\ \mu m \leq d \leq 18\ \mu m$ define the acceptable range of parameters for the dimensions of the fibre supporting channels.

Manufacturing the photolithographic stretcher templates.

For the fabrication of the pattern, a microscope glass slides was cleaned thrice with analytical reagent grade propanol, ethyl lactate and acetone and subsequently heated to 150°C for 10 min. The glass slide was cooled to ambient temperature in a dry nitrogen atmosphere. Photoresist was then applied by spin-coating.

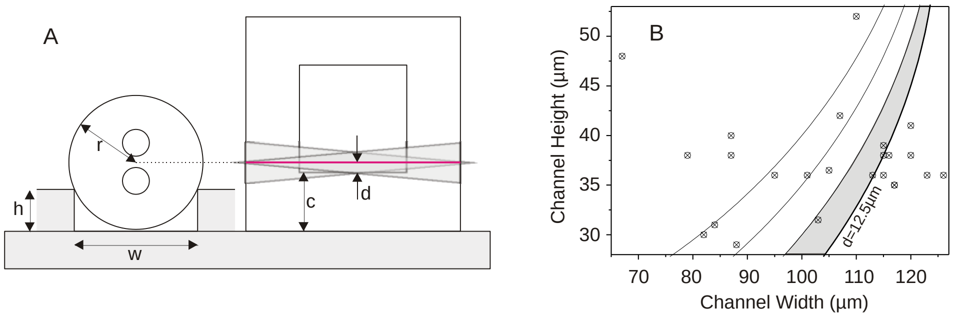

Figure 40 : Geometry and Dimensions of the Optical Stretcher. *Panel A illustrates the alignment of the fibre with respect to the capillary. At the left a cross-section of the fibre is held in the fibre channel. The fibre can be raised by fabricating a narrower channel. At the right is a cross-section of the square glass capillary, which rests on the glass slide. The two light cones, drawn as shaded regions, enter the capillary at the height of the fibre. Equation 10 is derived from this sketch. Panel B plots the dimensions of the fibre channels of several produced photolithographic structures and compares them with the desired target range (shaded region, where the beam centre height d is from 12.5 to 20 µm, see also Equation 10 and Panel A). These data were acquired with a DekTak profilometer. Only structures in the target range were subsequently used.*

Coating parameters were as follows, with minor modifications made on occasions when poor coverage was obtained (due to variations in resist viscosity): spin times of 60 s with an initial acceleration of 500 rpm/s and a final velocity of 1250 rpm.

Following this step, the solvents in the photoresist were removed by baking the slide at 60°C for 2 min and than at 100°C for an additional 5 min. The slide and the photolithographic mask were stacked in a photolithographic mask aligner (MJB4, Süss MicroTec AG, Germany) and exposed for 3 s to UV radiation. After exposure, the template was baked at 60°C for 1 min and then for 3 min at 100°C. Unexposed photoresist was removed by washing the (cooled down) sample in ethyl lactate for about 2 min and a final rinse with isopropanol.

The quality of the fabricated device was assessed by optical microscopy and feature sizes of the structure were quantified with a surface profilometer (DekTak, Veeco Instruments Inc., Plainview, USA). Figure 40B plots the height and widths of the manufactured fibre channels of numerous SU-8 patterns and compares them to the targeted values, showing only the patterns that had a capillary channel width of >200 μm).

Cultures and preparation of cells.

Red cells infected with *Pf* A4-BC6 clone (courtesy of B.C. Elford, Institute of Molecular Medicine, Oxford, UK), derived from clone A4 (Roberts et al., 1992), were cultured under a low-oxygen atmosphere by standard methods (Trager and Jensen, 1976). The culture medium (changed daily), was RPMI 1640 supplemented with 40 mM HEPES, 25 mg/l gentamicin sulphate, 10 mM D-glucose, 2 mM glutamine and 0.5% albumax. Parasite development and replication were assessed in cultures by microscopic inspection of Giemsa-stained thin blood smears and parasite count, as reported before (Tiffert et al., 2000). When the *Pf* parasites reached the late-trophozoite stage, IRBCs containing these parasites were concentrated from culture samples by gelatine flotation (Jensen, 1978; Pasvol et al., 1978) immediately prior to experimentation. The yield of trophozoite-containing IRBCs obtained by this procedure was about 45%; the remaining 55% were mostly uninfected red cells from the culture ("cohorts"). Both, IRBCs and cohorts were used for measurements. In addition, a "control" sample of normal, uninfected red cells never exposed to a *Pf* culture was also tested. RBCs used as controls were obtained from a healthy volunteer by venipuncture into a syringe with heparin after informed, written consent.

The RBCs were washed thrice by centrifugation and resuspension in over 10 volumes of serum-free medium. The buffy coat (platelets and white cells) was removed after each wash. After the last wash the RBCs were suspended in the same medium at 50% haematocrit and stored at 4 ^{o}C until use. Immediately prior to measurements of cell compliance both the sample containing IRBCs and cohorts, and the control sample were separately suspended in isotonic medium *AX* at a concentration of 10^5 cells·ml^{-1}. Solution *AX* contained (in mM): NaCl, 145; KCl, 3; Na-HEPES (pH 7.5 at 37°C), 10; $MgCl_2$, 0.15, and 0.5% albumax. All chemicals were analytical reagent quality. With the exception of albumax (Gibco, Invitrogen Ltd., UK) and the gelatine solution (“Plasmagel”; Bellon, Neuilly Sur Seine, France), all other chemicals were from Sigma-Aldrich Ltd., UK.

Stretching Procedure.

The cell compliance measurements were performed following previous protocols for cell compliance measurements (Lincoln et al., 2007; Lincoln et al., 2007). Paired Eppendorf reservoirs, containing the cell suspension and waste, were used as communicating vessels, inducing flow of cell suspension through the capillary when the waste reservoir was lowered slightly with respect to the cell reservoir. When a cell was in the trapping region, flow was stopped for the time of the measurement by levelling both reservoirs. The laser emission was then switched on and set to a low trapping power density (calculated to be $8.4 \cdot 10^5$ W/cm^2 in the centre of the trapping region for 40 mW power in each beam). The power density was then instantly increased (t_{rise} ~ $50\ \mu s$) to $53.4 \cdot 10^5$ W/cm^2 (laser power of 2 x 250 mW) for one second and then switched back to the previous lower trapping power, as sketched in Figure 41.

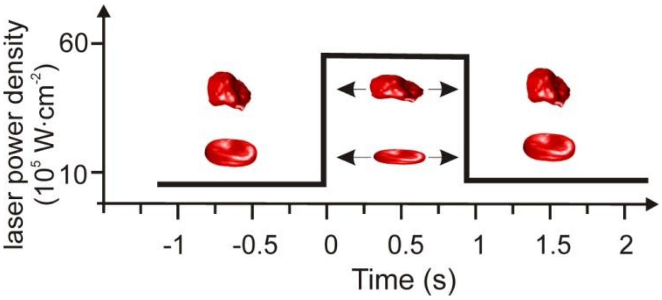

Figure 41 : Sequence of operation during experiment. *Plot of experimental time vs. laser intensity at first incidence to the trapped cell. After a cell is positioned in the trap, the capillary flow is halted. The image acquisition is started and after one second the stretcher light intensity is instantaneously stepped up for approximately one second. The cells stretch and relax according to the light intensity.*

In the malaria-infected sample, cohort cells were visually distinguishable from trophozoite-containing IRBCs as the latter contain dark haemozoin crystals and have irregular shape.

Imaging and Image Analysis.

The microfluidic optical stretcher was mounted on a Leica DM IRBE inverted microscope with a 63x long working distance objective (HCX-PL-FLL 63x, Leica Microsystems GmbH, Wetzlar, Germany) in phase-contrast mode. The stretching sequences were recorded with a microscope camera PL-A662 (Pixelink, Ottawa, ON, Canada) at ~12 frames per second. Laser and cameras were driven and synchronised with Labview 8.0 and a PC interface card USB-6212 (both National Instruments, Austin, TX, USA). Image analysis and edge detection were performed with custom-written software (courtesy of Jochen Gucks lab, Cavendish Laboratory, Cambridge) in Labview Vision (National Instruments, Austin, TX, USA).

The cell elongation was measured by performing an ellipse fit (see appendix for details) of the digitally recognised cell edge pixels, reporting the axis length that is parallel to the optical fibres (Matlab Image Processing Toolbox (The MathWorks Inc., Natick, MA, USA). Figure 42 shows two phase-contrast images of a stretching sequence. They show an example for detecting the cell edges in the trapped (Fig 42A) and stretched (Fig. 42B) state. Figure 42C shows an overlay of the two ellipses fitted to the cell edges, highlighting the differences between them.

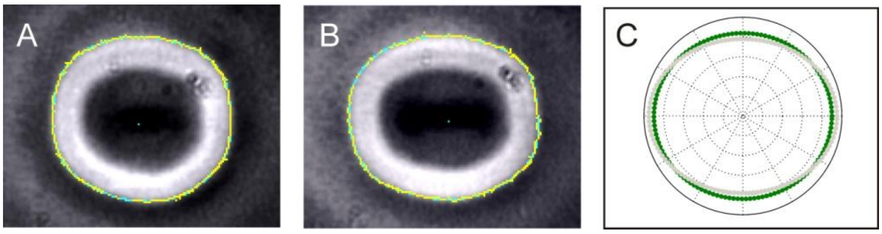

Figure 42 : Imaging a cell stretch. *The microscope was operated in phase contrast mode and images were captured with a digital camera. The image analysis routine (software from the Biological and Soft Systems group at the Cavendish laboratory) automatically locates the cell boundaries and displays corresponding cell edge pixels.* ***Panel A*** *shows an uninfected RBC in the trap at low light power, whereas* ***Panel B*** *is of the same cell at a higher laser power. The cell edge pixels are then processed with an ellipse-fitting routine.* ***Panel C:*** *Overlay of the fitted ellipses of the cell edges of panels A and B. The elongation of the cell during the high laser power is quantified as the ratio of lengths of the ellipse axes parallel to the laser fibres (horizontally in this plot).*

Results / Discussion

The compliance of three types of cells were analysed with the optical stretcher: i) trophozoite-containing IRBCs, ii) cohorts and iii) controls. A reduced compliance was observed for the IRBCs, which confirms previous results obtained with optical tweezers (Suresh et al., 2005; Suresh, 2006). Both cohorts and controls retained their normal biconcave disc-like shape. Figure 43 shows a comparison between the stretch-responses of controls ($n = 46$), cohorts ($n = 32$) and IRBCs ($n = 24$) as a scatterplot with error bars (standard error of the mean, SEM). Both uninfected samples display homogeneous behaviour in the optical stretcher, as evident also by the relatively small standard error (Figure 43). Furthermore, their compliance was very similar. In contrast, the IRBCs are less compliant, with a relative stretch amplitude, a, reduced to almost a half. The stretch-response of IRBCs was much more variable than that of uninfected cohorts and controls, as reflected in the much larger error bars. The fitted curves shown in Figure 43 represent the exponential strain-time relation from the Kelvin-Voigt model (Equation 7). The parameters for these fits are shown in Table 1.

Optical stretching of infected and uninfected red blood cells confirms results obtained with other single-cell mechanics-measurement techniques (Shelby et al., 2003; Suresh et al., 2005; Park et al., 2008; Marinkovic et al., 2009).

Measurements with optical tweezers had found IRBCs to stiffen significantly during parasite maturation, with shear moduli increasing up to 10-fold in the late schizont stage (Suresh et al., 2005).

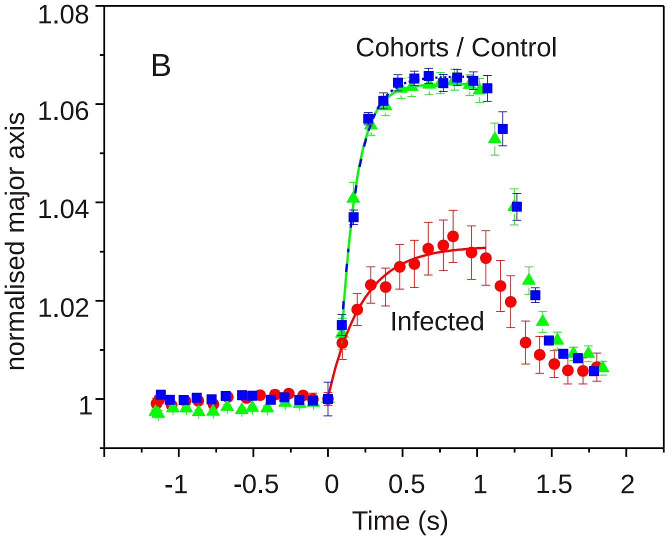

***Figure 43 : Deformation behaviour of uninfected RBCs compared to IRBCs**. Cohorts (blue squares, n=32) and controls (green triangles, n=46) behave similarly and exhibit small standard errors, whereas the IRBCs (red circles, n=24) show a greatly reduced compliance and larger standard errors. The scatter plot of the experimental data is fitted with an exponential function (Equation 7), extracting the characteristic deformation rate λ and the relative amplitude of the stretch a (see also Table 1)*

Here it has been demonstrated that even at an early trophozoite stage, when the increase in apparent stiffness (the relative stretching amplitude *a*) by a factor of ~2 is relatively modest, IRBCs can be easily detected with the optical stretcher (significance level $p < 0.001$ for the changes in both parameters *a* and λ). Also, the values found for the elasticity-viscosity ratio (the deformation rate λ) for uninfected RBCs are in good agreement with literature values reporting λ in the range of $5 - 16\ s^{-1}$ (Hochmuth and Waugh, 1987; Liu et al., 2007). This ratio decreases by a factor of ~3 for the infected cells in our experiment.

Our study suggests that uninfected cohort cells from a *Pf* culture and control RBCs do not have significantly different mechanical properties *in vitro*. This is in contrast to one clinical study (Dondorp et al., 1997) performed with ektacytometry. An ektacytometer usually applies a shear stress to the cells and measures the mean sphericity of a cell population by laser scattering.

Cell type	n	a	λ (s^{-1})	χ^2	D (μm)
Infected	24	$(36 \pm 3) \cdot 10^{-3}$	2.5 ± 0.7	$8 \cdot 10^{-6}$	4.2
Controls	46	$(64 \pm 1) \cdot 10^{-3}$	9.6 ± 0.4	$2 \cdot 10^{-6}$	4.6
Cohort	32	$(66 \pm 1) \cdot 10^{-3}$	8.6 ± 0.7	$8 \cdot 10^{-6}$	4.6

Table 1: Fitting parameters describing the cell deformations*. The table shows the number of stretch-responses, n, in each experiment, the two fitting parameters a and λ (Equation 10), the goodness of the fit (chi-square) and the average cell diameter in the trap before stretching, D.*

Dondorp et al. attribute the reduced deformability of red blood cells from patients with severe malaria also to alterations in the *uninfected* RBCs. The ekacytometer however, cannot distinguish between infected and uninfected RBCs. The extension to uninfected RBCs is made in that study because of the low fraction of parasitised cells present (<20%) and the finding that the measured deformability did not correlate with different parasitaemia levels. It was hypothesised that this increased rigidity in uninfected RBCs is caused by oxidative stress on the uninfected RBC membrane by the presence of parasitic haemozoin in the blood (Dondorp et al., 2000; Dondorp et al., 2000; Griffiths et al., 2001; Omodeo-Sale et al., 2003; Dondorp et al., 2004). The cohort cells in our culture were exposed to the

IRBCs for only a few parasite generations and the culturing medium was changed regularly.

In combination, this could result in reduced oxidative stress and thus in unaltered deformability of the cohort cells (although the oxidative stress under culturing conditions is typically higher than *in-vivo*). It remains to be elucidated, whether a reduced compliance can be observed with the optical stretcher in *ex vivo* RBC samples, collected from blood of malaria patients.

Quantifying the absolute elasticity modulus of the cells remains an open task. It is solvable in principle and has been demonstrated for spherical shapes (Guck et al., 2001). But the biconcave disc-like shape of uninfected RBCs, and the irregular shape of infected RBCs require theoretical modelling and FEM simulations to extract absolute numbers for forces and elasticity moduli (Yu et al., 2005; Liu et al., 2006). In the current experiments, it is unclear to what extent the reduced deformation a of the infected cells is due to increased stiffness or reduced optical forces, as haemoglobin concentration and shape changes during parasite maturation will affect the size of the opto-mechanical stress on the cell surface (Equation 9 and Chapter 2-5). However, the simplified phenomenological model used for analysis here proves to be sufficient for detecting the mechanical differences in diseased cells and thus the stretcher is a valuable diagnostic tool to detect and monitor early stages of infection. The characteristic deformation rate λ is independent of the actual magnitude of stress on the cell (within the range of reversible cell deformations). It represents the cell response to an unknown, but constant stress. Both parameters a and λ change significantly ($p < 0.001$) during infection and establish the use of this optofluidic device in applications that involve automatic cell sorting, early stage diagnostics or screening for active ingredients that reduce cell stiffening.

In summary, optical stretching is a promising novel technique to measure red blood cell mechanical properties and their changes during disease. Its main advantage is that it operates entirely in a non-contact manner and can thus render results that are free from artefacts induced by adhesion to surfaces or physical contact required in other single-cell mechanical-measurement techniques. In addition, by incorporation into a suitable microfluidic environment and automation, throughput rates approaching one cell per second can in principle be achieved, which compares favourably with other single-cell mechanical-measurement techniques (Lincoln et al., 2007; Lincoln et al., 2007).

Chapter 7: Conclusions

The colloid-osmotic hypothesis revisited

Hb concentration. The most critical condition for the validity of the colloidosmotic hypothesis (Chapter 2) is the prediction of a fall in Hb concentration in the IRBC host cytosol. The parasite induced new permeability pathways disrupt the homeostatic equilibrium of the RBC. The osmotic pressure exercised by Hb upon the cell, π_{Hb} is proportional to the product of its osmotic coefficient, f_{Hb}, and the Hb concentration in cell water, [Hb]: $\pi_{\mathrm{Hb}} = RT \cdot f_{\mathrm{Hb}} \cdot [\mathrm{Hb}]$ (Adair, 1929; McConaghey and Maizels, 1961; Savitz et al., 1964), where R is the gas constant and T the absolute temperature. Water inflow due to this osmotic pressure tends to swell the cell, a process normally counterbalanced by net salt extrusion in uninfected RBCs. Model simulations showed that the increased permeability of the infected host cell membrane puts the cell at risk of premature lysis, because the larger osmotic water inflow cannot be fully compensated anymore (Lew et al., 2003; Mauritz et al., 2010). To avoid critical cell swelling in the simulations a reduction in host Hb concentration was necessary, lowering the osmotic pressure on the cell. This model prediction remained controversial (Lew and Hockaday, 1999; Naughton et al., 2010) and was the main focus of the investigations reported here.

Before the time of these studies, no quantitative data on [Hb] in IRBCs was available. This thesis has presented results from quantifying [Hb] with two independent methods, fluorescence lifetime microscopy (Chapter 3) and electron probe X-ray microanalysis (Chapter 4). These investigations have confirmed a reduced [Hb] in the host cytosol and have found, as a by-product, additional noteworthy features of IRBCs. The FLIM method has documented a compartmentalisation of the host cell in the late trophozoite / early schizont stage, with an additional cluster from which haemoglobin appears to be largely excluded. The EPXMA data allowed deduction of the ion selectivity of the parasite induced new permeation pathway (NPP). This data showed that the K^+/Na^+ selectivity of the pathway may vary slightly, and is not always at the 2.3 value as was previously assumed based on a single experimental result (Staines et al., 2001). However, this result is not independently ascertained yet.

At the time when the FLIM [Hb] measurements were published, Park and colleagues (Park et al., 2008) also documented an overall decline in host haemoglobin concentration with parasite maturation similar to the one reported here. They had applied optical tomographic phase microscopy (TPM) for their study. This interferometric technique sweeps the illumination angle of the sample, similar to computer assisted X-ray tomography, and collects images of the optical phase information. Multiple acquisitions from different angles can then be used to calculate a refractive index map of the sample with the filtered back-projection method (inverse Radon transform). The transversal/longitudinal spatial resolution of the technique is limited to 0.5 µm and 0.75 µm (Choi et al., 2007), respectively. The refractive index was used to estimate the prevailing Hb concentration, on the assumption that Hb is the main contributor to the refractive index change. Their results rendered Hb concentrations of 7.0 ±0.5 mM, 6.5 ±0.4 mM, 4.9 ±0.4 mM, and 3.8 ±0.5 mM for uninfected, ring stage, trophozoite stage and schizont stage IRBCs in live cell samples, in good agreement with the results obtained by the FLIM/FRET and the EPXMA method. TPM is an elegant non-invasive *in-vivo* technique that does not rely on cytosol staining. However the relatively large voxel volume (roughly $0.5 \times 0.5 \times 0.75\ \mu m^3$) may cause the measurements to be affected by the presence of Hb-free domains within the host cytosol, such as vesicles surrounded by parasitophorous vacuolar membrane, which could generate bias towards lower concentrations of Hb in the host cytosol.

A comparison of the different [Hb] measurements with the model predictions is shown in Figure 44. The three independent techniques (FLIM, EPXMA, TPM) confirm the declining pattern suggested by the model, thus lending strong support to its most relevant prediction. The main tenet of the colloidosmotic hypothesis is thus supported by three independent observations obtained with different methods, both on live and sectioned cell samples.

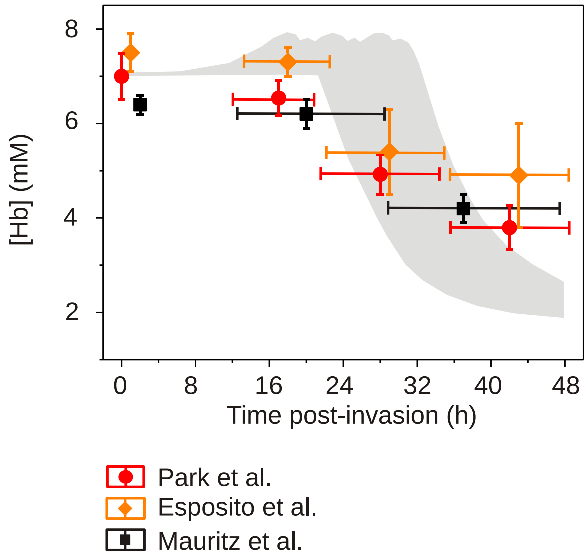

Figure 44: Comparison between predicted and measured variable values - the Hb concentration in host cell water, mM. *Averages of the measurements are drawn with their standard errors of the mean. The symbols indicate the source of the data, as follows: closed circles – Park et al. (Park et al., 2008); closed diamonds – Esposito et al. (Esposito et al., 2008), closed squares – Mauritz et al. (Mauritz et al., 2010). Data of Park et al. were modified from the original reference to fit the units used in the model. From this reference, [Hb] was obtained by dividing the Hb content of the cytosol by the water content of the cytosol after subtracting the volume occupied by the Hb molecules. The data was then normalized to the initial value of [Hb] used for the model simulations.*

Cell Volumes. In the literature, all claims on IRBC volume changes during parasite maturation were based on indirect observations. An increase in osmotic fragility (Lew et al., 2003) was interpreted as evidence for a volume increase during parasite maturation. But there was little or no increase in cell water volume, which lead to the assumption that IRBC swelling may not occur (Zanner et al., 1990; Saliba et al., 1998). Furthermore, pre-rupture terminal IRBC were found to have a near-spherical shape (Glushakova et al., 2005). One possible explanation for these findings is a reduction of cell membrane area during parasite maturation. This would reduce the critical haemolytic volume and render the cell osmotically fragile. While the cell assumed a terminal near-spherical shape due to the membrane area reduction, it would not be swollen significantly. This hypothesis motivated the direct investigations of IRBC volumes and membrane area with confocal microscopy. The data presented in Chapter 5 confirmed little change in cell volumes and a reduction in cell membrane area, resolving the apparent conflict of the earlier volume estimates (Allen and Kirk, 2004; Lew et al., 2004).

The IRBC numerical model can account for these discrepancies if for any volume unit of ingested cytoplasm the parasite grows only by about 30% of the ingested volume. The simulations with a growth/digestion coupling factor of 0.3 (Chapter 2) show that homeostatic IRBC stability is compatible with the measured [Hb] decline and with measured volumes hardly different from those of uninfected RBCs. A reduction of surface area was estimated by the 3D volume reconstructions, but simulations of osmotic fragility curves revealed that the measured surface area loss was not sufficient to account for the large increase in osmotic fragility (Esposito et al., 2010), suggesting also altered mechanical properties of the host cell membrane.

Cell Stretching

Because *Pf*-IRBCs are sequestered in the microcirculation and are exposed to variable shear stresses, it was important to investigate how infection alters the stretch and compliance properties of the cells.

While shear-rheometers and optical tweezers both usually require contact with the cells for quantitative mechanical measurement and are low-throughput, another optical trap can determine IRBC elasticity in a non-contact mode and with high throughput – an optical stretcher (Guck et al., 2001). Rather than trapping dielectric particles in the focus of one strongly focused laser beam, as is usually done in optical tweezers, in an optical stretcher objects are trapped between two non-focused counter-propagating laser beams. The author has constructed such an optical stretcher suitable for assessing the elasticity of red blood cells (Chapter 6). A reduced compliance of *Pf*-IRBCs was observed, which reproduces previous results obtained with optical tweezers (Suresh, 2006). The instrument provides a reliable platform for future investigations that intend to alter IRBC elasticity or observe cell-stretch related events such as the opening of ion channels (Egee et al., 2002; Dyrda et al., 2010).

Outlook

In addition to verifying predictions from the malaria infected red blood cell model, the author has engaged in various side projects. One of them deserves mentioning in this context, concerning the role of RBC volume as an important potential modulator of intracellular pH (pH_i) in uninfected RBCs. Direct measurements of pH_i were performed to test key predictions from a mathematical model of (uninfected) RBC volume homeostasis (Lew and Bookchin, 1986; Lew et al., 1991). The model predicts that changes of extracellular pH (pH_o) will modulate cell-volume and pH_i by influencing the activity of AE1. Similarly, RBC dehydration, induced by the opening of Ca^{2+}-activated Kcnn4 (KCa3.1) channels in the cell membrane, is predicted to cause a pH_i change, again through recruitment of AE1 activity. This latter volume/pH_i link has been suggested to occur in clinical episodes of sickle-cell anaemia (Bookchin et al., 1991; Lew and Bookchin, 2005), an inherited disease associated with the polymerisation of mutant haemoglobin (Hb S), leading to RBC dehydration. Activity of AE1 in the RBC is thus likely to be closely integrated into the mechanism of cell-volume homeostasis.

The link between volume and pH_i may also be relevant to other cell-types that express an anion exchanger at the cell membrane. In such cases, volume changes driven by net ionic gain or loss would be coupled to pH_i changes, the magnitude of which would depend on the fraction of H^+-equivalent traffic mediated by the anion exchanger. The subsequent study (Swietach et al., 2011) therefore explored the effect on RBC pH_i by inducing a net KCl loss from the cell. This was achieved by triggering the opening of Gardos-type K^+-conductance channels (Kcnn4, KCa3.1) in the plasma membrane (Gardos, 1958; Vandorpe et al., 1998; Begenisich et al., 2004). The experiments simultaneously recorded the cell diameter and pH_i by ratiometric imaging. With this technique it was demonstrated, for the first time in isolated RBCs, that an AE1-dependent intracellular acidosis is associated with dehydration. A major problem for ratiometric imaging in RBCs that had to be overcome was the powerful fluoerescence quenching by haemoglobin. This issue has been resolved by the use and careful calibration of the fluorescence dye carboxy-SNARF-1, which was shown to be compatible with confocal imaging under superfusion and flow cytometry. Intracellular pH is a major regulator of cell physiology, therefore measurements using SNARF-1 can help in the future by probing RBC function more directly in health and disease, and it may also serve as a diagnostic tool.

This thesis has covered the homeostasis and volume regulation of IRBCs. Open question for future research could lead to analysing the nature of the NPPs in more depth. The discrepancy of their documented specificity for K^+ (Staines et al., 2001) and measuring unspecific NPPs with the EPXMA method deserves a more detailed investigation. Furthermore, very little is currently known about the origins or structure of the NPP. There is interest in future research collaborations to investigate a hypothesised similarity of the NPPs with the membrane protein VDAC (voltage-dependent anion channel) (Kirk, 2001). It is still an open question whether the NPPs represent parasitic insertions or upregulated ion channels that are silent in mature erythrocytes.

Publications

During the time of the doctoral training, the author has contributed to the following journal articles:

Thomas S, Mauritz JMA, Egée S and Lew VL, *Could a VBR-VDAC channel be responsible for increasing intracellular free Ca^{2+} concentrations during red blood cell aging?*, manuscript in preparation. Roscoff/Cambridge 2011.

Mauritz JMA, Seear R, Esposito A, Kaminski CF, Skepper J, Warley A, Lew VL and T Tiffert, *X-Ray Microanalysis Investigation of the Changes in Na, K, and Hemoglobin Concentration in Plasmodium falciparum-Infected Red Blood Cells*, Biophys J, 2011. 100(6): p. 1438.

Swietach P, Tiffert T, Mauritz JMA, Seear R, Esposito A, Kaminski CF, Lew VL and RD Vaughan-Jones, *Hydrogen ion dynamics in human red blood cells.*, J Physiol 2011. 588(24): p. 4995.

Mauritz JMA, Esposito A, Tiffert T, Skepper J, Warley A, Yoon YZ, Cicuta P, Lew VL, Guck J and CF Kaminski, *Biophotonic techniques for the study of malaria-infected red blood cells*, Medical & Biological Engineering & Computing, 2010. 48(10): p. 1055.

Esposito A, Choimet JB, Skepper J, Mauritz JMA, Lew VL, Kaminski CF and T Tiffert, *Quantitative imaging of human red blood cells infected with Plasmodium falciparum.* Biophys J, 2010. 99(3): p. 953.

Mauritz JMA, Tiffert T, Seear R, Lautenschlager F, Esposito A, Lew VL, Guck J and CF Kaminski, *Detection of Plasmodium falciparum-infected red blood cells by optical stretching.* J Biomed Opt, 2010. 15(3): p. 030517.

Mauritz JMA, Esposito A, Ginsburg H, Kaminski CF, Tiffert T and VL Lew, *The homeostasis of Plasmodium falciparum-infected red blood cells.* PLoS Comput Biol, 2009. 5(4): p. e1000339.

Mauritz JMA, Morrisby R, Hutton R, Legge C and CF Kaminski, *Imaging pharmaceutical tablets with optical coherence tomography*. J Pharm Sci, 2009. 98(7): p. 385.

Esposito A, Tiffert T, Mauritz JMA, Schlachter S, Bannister L, Kaminski CF and VL Lew, *FRET Imaging of Hemoglobin Concentration in Plasmodium falciparum-Infected Red Cells.* PLoS ONE, 2008. 3(11): p. e3780.

Appendix A: Modelling the changes in host red cell homeostasis during the asexual reproduction cycle of plasmodium falciparum

Software.

The mathematical-computational model of the homeostasis of *Plasmodium falciparum*-infected red blood cells (IRCM) was derived as an extension of the original Lew-Bookchin red cell model (RCM) (Lew and Bookchin, 1986). Both models are available as free-standing executable files from http://www.physiol.cam.ac.uk/staff/lew/index.htm. The IRCM first computes a "Reference" steady-state (RS) meant to represent the initial condition of a human red blood cell just invaded by a *falciparum* merozoite generating a ring-stage internalized parasite occupying 4 % of the red cell volume. In the formulation of the RS the programme offers a large variety of options for the user to change constitutive properties of the IRBC such as the value of all the parameters tested in the simulations reported in this paper. For the simulations reported here the medium was assumed to be an infinite reservoir (vanishingly low hematocrit condition). With the RS defined, the programme is set to follow the dynamic evolution of the IRBC system (Dynamic state, DS) for 48 hours with a data output frequency chosen by the user. To enable realistic comparisons with experimental results, experimental conditions can be simulated to explore the modified dynamic behaviour of the system. All referenced model equations with prefix S can be found in appendix A.

The algorithm

Computation of the Reference State.

The constitutive properties of IRBCs defined in the RS comprise:

1. The detailed initial composition of intra and extracellular fluids complying with electroneutrality and osmotic equilibrium (eqs S11 and S12)
2. The identity, concentration, and protonized state of medium H^+ buffers (HEPES-like in the current simulations (eq S13)
3. The identity, concentration and mean charge of the impermeant cell solutes (eqs S14 and S15)
4. The cytoplasmic H^+ buffering behaviour of Hb (eq S15) (Cass and Dalmark, 1973)
5. The power function describing the non-ideal osmotic behaviour of Hb (eq S6) (McConaghey and Maizels, 1961; Freedman and Hoffman, 1979)
6. The initial fraction of IRBC volume occupied by Hb molecules (25%) (Bureau and Banerjee, 1976; Lew et al., 1991)
7. The magnitude and kinetics of active Na^+ and K^+ transport through the sodium pump (eqs S17-S20) (Garrahan and Garay, 1974; Lew et al., 1991)
8. The magnitude and kinetics of all unidirectional and net passive fluxes of Na^+, K^+, A^- and H^+ through each of the endogenous passive transporters expressed in the cell (eqs S21-S29) (Lew and Bookchin, 1986)
9. The electrical potential potential difference across the RBC membrane (eqs S30,S31)
10. The stage-dependent changes in NPP-mediated permeabilities (Figure **3**, eq S32) (Kirk, 2001; Staines et al., 2001; Lew et al., 2003)
11. The maximal magnitude and kinetics of Na^+, K^+ and A^- fluxes through NPPs (eq S24) (Kirk, 2001)
12. The Hb consumption function (Figure **3**, eq S33) (Lew et al., 2003)
13. Cell volume normalized to 1 at t = 0 (Garrahan and Garay, 1974)
14. Area-volume ratio of RBC encoded in critical haemolytic volume set at 1.7 times the initial cell volume (volume of sphere contained within original RBC membrane area) (Ponder, 1948)

All functions were defined with a default set of parameter values, open to change by the modeller. The default values are displayed at the prompts in the running of the model. The initial values of most system parameters and variables were listed following a hierarchical order of reliability for the information available so as to enable derivation of lesser known from better known values in the equations of the Reference State (Lew and Bookchin, 1986; Lew and Bookchin, 2005). The kinetic equations were defined with minimal sets of parameters to avoid unnecessary complexity.

Computation of the Dynamic State.

Three main processes determine the overall dynamic behaviour of IRBCs: NPP-mediated traffic, Hb consumption and parasite volume growth. The potential osmotic stress generated by the amino acids produced during Hb digestion was neglected in the model because the amino acid composition of the effluent from infected RBCs was indistinguishable from that of globin, indicating that NPP permeability was high enough not to limit the rate of exit of the lesser permeable amino acids (Zarchin et al., 1986; Kirk, 2001; Krugliak et al., 2002).

Parasite volume growth was linked to Hb ingestion as follows. For any infinitesimal time interval, represented by the integration interval $\mathrm{D}t$ in the numerical computations, the parasite ingests a volume of red cell cytoplasm, DV_w (eqs S26, S27) containing the amount of Hb prescribed by the Hb consumption function for that time interval (eq S22). This reduces the host cell volume by $\mathrm{D}V_w$ and increases parasite volume by $cf \cdot \mathrm{D}V_w$ in each $\mathrm{D}t$. cf represents a coupling coefficient which converts $\mathrm{D}V_w$ to a quantum of parasite volume-growth within $\mathrm{D}t$, proportional to $\mathrm{D}V_w$, to enable the modeller to explore the effect of broad parasite volume-growth variations, and also the volume-effects of single and multiple invasions.

Global volume changes within the host compartment are determined by parasite ingestion of host cytosol and by fluid transfers across the host cell plasma membrane resulting from changes in membrane permeability (NPP development), ionic gradients and colloid osmosis. Ingestion, parasite volume growth and homeostasis are therefore closely interdependent processes because ingestion affects host Hb content on which colloid osmosis largely depends and homeostasis affects the size of each $\mathrm{D}V_w$ on which parasite volume growth depends. At each time, t, parasite volume, V_P, and host cell volume, V_H, result from the cumulative changes generated by host cytosol transfers to parasite and by all the ion and water fluxes through endogenous and parasite-generated pathways up to t. Thus, $V_P = V_P^o + cf\Sigma\ \mathrm{D}V_w$ and $V_H = V_H^o + \Sigma DV' - \Sigma\ \mathrm{D}V_w$, respectively, where V_P^o represents the initial ring-stage parasite volume, V_H^o represents the initial host cell volume, normalized to 1, and DV' represents the homeostasis-induced infinitesimal change in host cell volume within each $\mathrm{D}t$. In the running of the model, V_H at each t is computed from equation S41, as detailed in Appendix A. IRBC volume at each t, V_{IRBC}, is thus defined by $V_{IRBC} = V_H + V_P$. Solute exchanges between parasite and host, as well as possible homeostatic effects resulting from host cell membrane alterations were not considered in the model because their relevance remains uncertain and precise information, with the detail required for useful modelling is lacking.

The following sequence was applied in the computation of the transient behaviour of the IRCM for each Dt interval.

1. RS defined
2. If simulating experiments, enter changes in medium composition and system parameter values
3. Compute membrane potential from equation S31, implicit in E_m
4. With E_m defined, compute net fluxes through all transporters, Φ_i (eqs S17-S28)

5. With Φ_i defined, compute the change in cell amount of each solute, DQ_i (eqs S34 and S35) and the new amount of solute i, Q_i^t (eq S36)
6. Compute the volume of RBC cytosol, DV_W (eq S37), to be ingested during *Dt* to provide the amount of Hb to the parasite specified by equations S33 and S38 for each *t*
7. Compute parasite volume, V_P (eq S39)
8. Compute the new concentrations of each cell solute C_i (eq S40)
9. Compute the water flux, Φ_W (eq S29)
10. Compute the new volume of host cell water, V_w (eq S38)
11. Compute the new host cell volume, V_H (eq S41, S42)
12. Compute the new value of the iteration interval, *Dt* (eq S43)
13. Convert the new C_H to pH^c (eq S44), compute the new charge on Hb, n_{Hb} (eq S14), and the new anion and proton concentration ratios (eqs S45 and S46, respectively)
14. Compute the new f_{Hb} from the new C_{Hb} (eq S16)
15. Test for *t* assigned to output results (if no, continue; if yes, output results)
16. Test for IRBC volume exceeding set value of critical haemolytic volume (if no, continue; if yes, terminate programme and output final results)
17. Test for t = 48 h (if no, continue; if yes, terminate programme and output final results)
18. Test for further input of experimental conditions (if no, continue; if yes, stop, input further changes, continue)
19. Go to step 3

Glossary of symbols and equations for the homeostatic model of malaria-infected red blood cells

The nomenclature follows that applied in earlier models of the homeostasis of erythroid cells (Lew and Bookchin, 1986; Lew et al., 1991). No distinctions are made between Cl^- and other highly permeable anions (i.e. HCO_3^-), globally labelled A. Parameters of the Na:Cl and K:Cl cotransports are indexed NaA, KA, respectively, in the understanding that only Cl^- is meant here, whereas for the Cl:H cotransport representing the operation of the Jacobs-Stewart mechanism (Lew et al., 1991), the A in AH represents any anion that is a substrate of the anion exchanger.

Q_i	Amount of solute *i* per 10^{13} cells
$Q_\pm$	Net charge on impermeant cell ion (mEq(10^{13}cells)$^{-1}$))
C_i^c, C_j^m	Concentration of solute i in cell water (^{c}) or of solute j in extra-cellular medium (^{m}) (molar, M, for H^+ ions; millimolar, mM for all other solutes
Subscript i,j	All solutes or any subset of solutes among Na, K, Mg, A, Hb, X, Y, B, HB and H (i=j for all permeant solutes: Na, K, A, H)
Hb	Haemoglobin
A	Permeant anion
X	Global impermeant intracellular anion, assumed to be non-protonizable
$Y_\pm$	Impermeant extracellular monovalent ion (gluconate, N-methylglucamine or choline, for instance
B	Impermeant extracellular H^+ buffer (Hepes-like, in present simulation)
HB	Protonized form of extracellular H^+ buffer
K_B	Dissociation constant of extracellular H^+ buffer (M)

pH^c,pH^m	Cell and medium pH, respectively
n_x,n_{Hb}	Mean net charge on X and Hb, respectively (Eq(mol)$^{-1}$).
pI	Isoelectric pH of Hb
a	Slope of the proton titration curve of Hb (Eq(mol)$^{-1}$) (Cass and Dalmark, 1973; Dalmark, 1975)
f_{Hb}	Osmotic coefficient of Hb (osmol(mol)$^{-1}$)
b,c	Virial coefficients of linear and quadratic terms, in f_{Hb} equation (Freedman and Hoffman, 1979)
z_i, F, R, T, E_m	Valence of ion *i*, Faraday constant, gas constant, absolute temperature and membrane potential (mV), respectively
E_i	Equilibrium potential of ion i (mV)
I_i	Electrodiffusional current across cell membrane (μA(10^{13}cells)$^{-1}$)
Φ_i	Total flux of permeant solute i (mmol(10^{13}cells)$^{-1}$))
$Y^{Hb}(\mathrm{t})$	Hb consumption
$\mathrm{Y}^{\mathrm{Hb}}_{\mathrm{max}}$	Maximal Hb consumption (relative to initial Hb content of IRBC)
$\mathrm{t}^{\mathrm{NPP}}_{1/2}$	Half-time of NPP induction curve (*h*)
$\mathrm{t}^{\mathrm{Hb}}_{1/2}$	Half-time of Hb consumption curve (*h*)
s^{Hb}	Slope-parameter of the Hb-digestion curve (*h*)
s^{NPP}	Slope-parameter of the NPP induction curve (*h*)
cf	Coupling factor, determines parasite volume

	growth as fraction of cumulative cytostomal ingestions
p,q	Scaling factors of integration interval
V_W	Volume of cell water ($l(10^{13}\text{cells})^{-1}$))
V_{P}	Parasite Volume at time t
V_{P}^{0}	Initial ring-stage parasite volume, assumed to occupy 4% of IRBC volume
V_H	Host cell volume at time t
V_{H}^{0}	Initial host cell volume normalized to 1
V_{IRBC}	Volume of infected cell at time t, relative to V_H^0

Partial flux components of solute i (mmol(10^{13}cells)$^{-1}$)h^{-1})

Φ_i^P	The Na^+ pump
Φ_i^G	Electrodiffusional constant-field channels (G)
Φ_i^{HA}	H:A (HA) cotransport (represents the Jacobs-Stewart mechanism, (Lew and Bookchin, 1986))
Φ_i^{KA}	K:Cl (KA) cotransport
Φ_i^{NaA}	Na:Cl (NaA) cotransport
Φ_i^{NaH}	Na:H (NaH) countertransport
$\Phi_{Na}^{F_{max}}, \Phi_{Na}^{R_{max}}$	Saturated forward (F) and reverse (R) Na^+ fluxes through the Na^+ pump
Φ_i^{NPP}	Flux of ion *i* through *P. falciparum*-induced new permeation pathway (NPP)
$P_{\mathrm{i}}^{\mathrm{G}}$	Permeability constant of solute *i* through electrodiffusional

	pathways (h^{-1})
$P_{\mathrm{i}}^{\mathrm{NPP}}(\mathrm{t})$	Time dependant permeability for ion *i* through the NPP
$P_{\mathrm{i,max}}^{\mathrm{NPP}}$	Maximum permeability for the ion *i* through the NPP (h^{-1})
k_{HA}	Rate constants for the H:A (HA) cotransport
k_{KA}	Rate constant of K:A cotransport
k_{NaA}	Rate constant for Na:A cotransport
Φ_{W}	water flux across cell membrane ($l(10^{13}\mathrm{cells})^{-1}\ h^{-1})$)
$\mathrm{D}t$	Integration interval
$\mathrm{D}V_W$	Hb consumption-induced change in the volume of cell water per unit original volume of cells during one integration interval ($l(10^{13}\mathrm{cells})^{-1})$)
$\mathrm{D}V'$	Homeostasis-induced change in host cell volume per unit original volume of cells during one integration interval ($l(10^{13}\mathrm{cells})^{-1})$)
$\mathrm{D}Q_i$	Change in the intracellular amount of solute *i* during one integration interval ($\mathrm{mmol}(10^{13}\mathrm{cells})^{-1})$)
r_A,r_H	Ratio between external and internal permeant anion concentrations (r_A) or between internal and external hydrogen ion concentrations (r_H)

Superscripts (*o*,*t* and $t–\mathrm{D}t$ on a variable indicate the value of that variable in the original reference steady state (*o*), at any subsequent time (*t*), or at the preceding integration interval ($t–\mathrm{D}t$). The absence of a time-indicating superscript on any variable is equivalent to the superscript *t*. t_n is the n-th iteration in the numerical computation such that $t_{n+1}=t_n+\mathrm{D}t$.

Model equations

Reference State isotonicity

$$f_{Hb} \cdot C^{c}_{Hb} + C^{c}_{Na} + C^{c}_{K} + C^{c}_{Mg} + C^{c}_{X} + C^{c}_{A} = C^{m}_{Na} + C^{m}_{A} + C^{m}_{B} + C^{m}_{Y} \qquad \text{(S11)}$$

Reference State electroneutrality

$$Q^{0}_{Na} + Q^{0}_{K} + Q^{0}_{Mg} - Q^{0}_{A} - Q^{0}_{-} = 0 \qquad \text{(S12)}$$

$$C^{m}_{HB} = B \cdot \frac{C^{m}_{H}}{K_B + C^{m}_{H}} \qquad \text{(S13)}$$

H^{+} buffer behavior of Hb (Cass and Dalmark, 1973; Dalmark, 1975; Freedman and Hoffman, 1979)

$$n_{Hb} = a(pH^{c} - pI) \qquad \text{(S14)}$$

$$Q_{-} = n_{Hb} \cdot Q_{Hb} + n_{X} \cdot Q_{X} + 2Q_{Mg} \qquad \text{(S15)}$$

Nonideal osmotic behavior of Hb (Cass and Dalmark, 1973; Dalmark, 1975; Freedman and Hoffman, 1979)

$$f_{Hb} = 1 + b \cdot \frac{Q_{Hb}}{V_W} + c \cdot \left(\frac{Q_{Hb}}{V_W}\right)^{2} \qquad \text{(S16)}$$

Flux equations.

Na^{+} pump-mediated fluxes (dissociation constant values from reference (Garrahan and Garay, 1974; Lew and Bookchin, 1986))

Forwards:

$$\Phi^{PF}_{Na} = -\Phi^{F_{max}}_{Na}\left(\frac{\mathrm{C}^{\mathrm{C}}_{\mathrm{Na}}}{\mathrm{C}^{\mathrm{C}}_{\mathrm{Na}} + 0.2(1 + \mathrm{C}^{\mathrm{C}}_{\mathrm{K}}/8.3)}\right)^{3}\left(\frac{\mathrm{C}^{\mathrm{m}}_{\mathrm{K}}}{\mathrm{C}^{\mathrm{m}}_{\mathrm{K}} + 0.1(1 + \mathrm{C}^{\mathrm{m}}_{\mathrm{Na}}/18)}\right)^{2} \qquad \text{(S17)}$$

Reverse:

$$\Phi^{PR}_{Na} = \Phi^{R_{max}}_{Na}\left(\frac{\mathrm{C}^{\mathrm{C}}_{\mathrm{K}}}{\mathrm{C}^{\mathrm{C}}_{\mathrm{K}} + 8.3(1 + \mathrm{C}^{\mathrm{C}}_{\mathrm{Na}}/0.2)}\right)^{2}\left(\frac{\mathrm{C}^{\mathrm{m}}_{\mathrm{Na}}}{\mathrm{C}^{\mathrm{m}}_{\mathrm{Na}} + 18(1 + \mathrm{C}^{\mathrm{m}}_{\mathrm{K}}/0.1)}\right)^{3} \qquad \text{(S18)}$$

Net:

$$\Phi^{P}_{Na} = \Phi^{PF}_{Na} + \Phi^{PR}_{Na} \qquad \text{(S19)}$$

$$\Phi_K^P = -\frac{\Phi_{Na}^P}{1.5} \quad \text{(S20)}$$

Carrier-mediated cotransport (low-saturation kinetics)

$$\Phi_{Na,A}^{NaA} = -k_{NaA}(C_{Na}^c C_A^c - C_{Na}^m C_A^m) \quad \text{(S21)}$$

$$\Phi_{K,A}^{KA} = -k_{KA}(C_K^c C_A^c - C_K^m C_A^m) \quad \text{(S22)}$$

Jacobs-Stewart flux

$$\Phi_H^{HA} = \Phi_A^{HA} = -\mathrm{k_{HA}}(\mathrm{C_A^c C_H^c} - \mathrm{C_A^m C_H^m}) \quad \text{(S23)}$$

Electrodiffusional fluxes, including NPP-mediated fluxes

$$\Phi_i^G = -\mathrm{P_i^G} \cdot \left(\frac{z_i F E_m}{RT}\right) \cdot \left[\mathrm{C_i^c} - \mathrm{C_i^m} \cdot \exp\left(-\frac{z_i F E_m}{RT}\right)\right] \cdot \left(1 - \exp\left(-\frac{z_i F E_m}{RT}\right)\right)^{-1} \quad \text{(S24)}$$

$$\Phi_{Na} = \Phi_{Na}^P + \Phi_{Na}^G + \Phi_A^{NaA} + \Phi_{Na}^{NPP} \quad \text{(S25)}$$

$$\Phi_K = \Phi_K^P + \Phi_K^G + \Phi_K^{KA} + \Phi_K^{NPP} \quad \text{(S26)}$$

$$\Phi_A = \Phi_A^G + \Phi_A^{NaA} + \Phi_A^{KA} + \Phi_A^{HA} + \Phi_A^{NPP} \quad \text{(S27)}$$

$$\Phi_A = \Phi_A^G + \Phi_A^{HA} + \Phi_A^{NPP} \quad \text{(S28)}$$

$$\Phi_W = P_W \cdot \left[f_{Hb} \cdot Q_{Hb} + \textstyle\sum_i C_i^c - \sum_j C_j^m\right] \quad \text{(S29)}$$

$$I_i = z_i \cdot F \cdot \Phi_i \quad \text{(S30)}$$

Maintenance of electroneutrality (neglecting capacitative transients)

$$\textstyle\sum_i I_i = 0 \quad \text{(S31)}$$

Time-dependent NPP permeability

$$P_i^{NPP,G}(t) = P_{i,max}^{NPP,G} \cdot \left(1 + \exp\left[\frac{t_{1/2}^{NPP} - t}{s^{NPP}}\right]\right)^{-1} \quad \text{(S32)}$$

Hb consumption function

$$Y^{Hb}(t) = Y_{max}^{Hb} \cdot (1 + \exp\left[\frac{t_{1/2}^{Hb} - t}{s^{Hb}}\right])^{-1} \quad \text{(S33)}$$

$$\Phi_i = \frac{\mathrm{DQ_i}}{\mathrm{Dt}} \tag{S34}$$

$$\mathrm{D}Q_i = \Phi_i \cdot \mathrm{D}t \tag{S35}$$

$$Q_i^t = Q_i^{t-Dt} + \mathrm{D}Q_i \tag{S36}$$

$$\mathrm{D}V_W = V_W^t - V_W^{(t-\mathrm{D}t)} \tag{S37}$$

Host cytosol volume ingestion function:

$$V_W(t_{n+1}) = V_W(t_n) \cdot \frac{1-Y^{Hb}(t_{n+1})}{1-Y^{Hb}(t_n)} \tag{S38}$$

Cumulative parasite volume growth

$$V_P = V_P^0 + cf \cdot \sum_{t_n} \mathrm{D}V_W \tag{S39}$$

$$C_i^{c,t} = \frac{Q_i^t}{V_W^t} \tag{S40}$$

Host cell volume at t=t_n

$$V_H = V_H^0 + \sum_{t_n} \mathrm{D}V' - \sum_{t_n} \mathrm{D}V_W \tag{S41}$$

$$\mathrm{D}V' = \Phi_W \cdot \mathrm{D}t \tag{S42}$$

$$\mathrm{D}t = \frac{p}{q+\sum|\Phi_\mathrm{i}|} \tag{S43}$$

$$pH^{c,m} = -\log C^{c,m} \tag{S44}$$

$$r_A = \frac{C_A^m}{C_A^c} \tag{S45}$$

$$r_H = \frac{C_H^c}{C_H^m} = \exp_{10}(pH^m - pH^c) \tag{S46}$$

Appendix B: Fluorescence Lifetime Imaging

FRET and molecular crowding

Förster resonance energy transfer is the non-radiative transfer of energy from a donor fluorophore to an acceptor chromophore mediated by a long-range dipole-dipole interaction (Förster, 1948; Lakowicz, 1999). Figure **11**A shows that the fraction of quanta transferred from a donor to an acceptor – the FRET efficiency (E) – drastically depends on the inter-chromophore distance (R):

$$E = [1 + (R/R_0)^6]^{-1} \tag{S47}$$

R_0 – the Förster distance - is the distance at which 50 % of quanta are transferred. Typical fluorophores used as FRET pairs (*e.g.*, cyan- and yellow- fluorescent proteins or green fluorescent protein and Cy3) exhibit Förster distances around 5 nm. Because of the strong dependence on intra-molecular distances within the 10 nm range, i.e., the range of protein dimensions, FRET is often used in biology to quantify protein-protein interactions (Wouters et al., 2001).

Fluorescence emission is a stochastic process that follows an exponential decay distribution (see Fig. **11**C), characterized by a mean time constant usually described as the fluorescence lifetime (τ) (Lakowicz, 1999; Esposito et al., 2004). The fluorescence lifetime is a molecular characteristic of a fluorophore that is considered comparatively insensitive to concentration over the physiological concentration ranges of typical biomolecules. The fluorescence lifetime is also independent from the geometrical characteristics of the detection system. FLIM is thus a robust technique for the quantitative mapping of biophysical properties of the fluorophore environment through changes in fluorescence lifetime. For instance, FRET shortens the fluorescence lifetime of a donor fluorophore (see Fig. **11**C, *dashed lines*) and, indeed, FRET imaged by FLIM is one of the most robust techniques to detect protein-protein interaction with comparatively high spatial resolution (Pelet et al., 2006).

At high concentrations (millimolar range) of acceptor fluorophore, a freely diffusing acceptor has a significant probability to be in close proximity to a donor fluorophore (within twice the Förster distance). Therefore, energy transfer can occur also in the absence of specific direct interaction of the two molecules; in this case, the fluorescence decay of the donor follows a stretched exponential decay (Förster, 1948; Lakowicz, 1999):

$$I(t) = exp\left\{-\frac{t}{\tau_0} - 2\frac{A}{A_0}\sqrt{\frac{t}{\tau_0}}\right\} \tag{S48}$$

where A is the concentration of the acceptor and A_0 is the critical concentration, defined as the concentration at which 76 % of energy is transferred. Eq. S48 is valid if there is no resonance energy transfer between donor molecules, as expected at low donor concentrations. It is important to stress that there are two different definitions of critical concentration conventionally referred to as A_0 and C_0 (Lakowicz, 1999).

The critical concentration A_0 is related to the Förster distance by the following relation, where N is the Avogadro number:

$$A_0 = 1500\pi^{-3/2}N^{-1}R_0^{-3} \approx 447R_0^{-3} \tag{S49}$$

For A_0 to be derived in millimolar units R_0 has to be expressed in nanometres. The Förster distance depends on the donor-acceptor spectral overlap integral (J) that is defined as (Lakowicz, 1999):

$$J(\lambda) = \left(\int_0^\infty \mathrm{d}\lambda\, F_D(\lambda)\varepsilon_A(\lambda)\lambda^4\right) / \left(\int_0^\infty \mathrm{d}\lambda\, F_D(\lambda)\right) \tag{S50}$$

where F_D is the emission spectrum of the donor and ε_A is the molar extinction coefficient of the acceptor. When the wavelength is expressed in nanometres, the Förster distance is obtained in nanometres from the following equation:

$$R_0 = 0.0211(\kappa^2 Q J n^{-4})^{1/6} \qquad \text{(S51)}$$

κ^2 is an orientation factor equal to 2/3 assuming rotational freedom of the molecules, Q is the quantum yield of the donor fluorophore and n (~1.4) is the refractive index of a red blood cell cytoplasm.

Because of the high molar extinction coefficient of Hb that extend to the visible region (Horecker, 1943), the spectral overlap between any donor fluorophore emitting below 600 nm and Hb is not negligible (Fig. **11** B). Calcein was the donor chosen for the present experiments because its emission peak is distant to the Hb absorption peaks. It provides a quantum yield of ~0.38 (Beghetto et al., 2000) in sodium phosphate buffer (pH = 7.4) and its fluorescence lifetime is about 4 ns. For lower quantum yields – likely to happen in cell cytosol - R_0 and A_0 will be lower and higher, respectively, of the values computed by numerical estimation.

The Förster distance for the haeme-calcein pair was estimated to be about 4.1 nm by numerical integration of eq. S50 and substituting in eq. S51. The critical concentration of the haemoglobin tetramer ($[\mathrm{Hb}]_0$) can thus be estimated to be about 1.7 mM.

Data analysis

Assuming the variations of quantum yield of the fluorophore proportional to the variations in the average fluorescence lifetime, the average fluorescence lifetime of calcein in the presence of haemoglobin can be predicted by the following equation (Bennett, 1964; Lakowicz, 1999):

$$\langle \tau[Hb] \rangle \approx \tau_0 \left\{ 1 - \sqrt{\pi} \frac{[Hb]}{[Hb]_0} e^{\left(\frac{[Hb]}{[Hb]_0}\right)^2} \left[1 - erf\left(\frac{[Hb]}{[Hb]_0} \right) \right] \right\} \qquad \text{(S52)}$$

Therefore, fluorescence lifetime imaging of calcein can provide a direct estimation of [Hb]. The average lifetime was obtained by fitting scatter, IRF, background and a three exponential function with SPCImage in order to reliably fit the experimental data. At the typical photon counts obtained (~300 count per pixel), high spatial binning (5x5) was required. Furthermore, when Eq. S52 was fitted to the calibration data shown in Figure **12**A-B, an apparent critical concentration of 2.9 ± 0.1 mM was estimated. This was assumed to depend on the very high quenching of calcein in the RBC, that cause the measured fluorescence lifetime in physiological condition (~ 250 ps) to be in the same order of magnitude of the instrument response function (IRF, ~ 170 ps). Therefore, eq. S48 was fitted by iterative reconvolution to regions segmented by the phasor approach (Digman et al., 2007) including in the data fitting the presence of scatter (arbitrarily set as a 10 ps decay), background, unquenched calcein variable offset and IRF broadness.

A synthetic IRF was generated by the following equation:

$$IRF(t,w) = k\begin{bmatrix} \frac{1}{w\sqrt{\pi}} exp\left[-2\left(\frac{t-t_0}{w}\right)^2\right] + \\ 0.09 exp\left(\frac{t_0-t-0.4ns}{1.35ns}\right) + \\ 0.05 exp\left(\frac{t_0-t-1.05ns}{1.35ns}\right) \end{bmatrix} \tag{S53}$$

were all parameters were determined fitting an experimental IRF that was generated imaging light scattered by a microscopy glass-slide; the broadness of the Gaussian component (w) was fitted to the TCSPC data and k is a normalization factor.

Iterative reconvolution provided a more realistic critical concentration value of 1.68 ± 0.05 mM and an optimal balance between spatial resolution and robust quantification.

We note that a fluorophore with a larger Förster distance with the haeme chromophore compared with calcein could be beneficial in order to shift the critical concentration at higher values. However, it was not possible to find a fluorophore that could combine the advantages of an acetoxymethyl derivative (for non-invasive staining of living cells) providing the adequate spectral properties and availability of the non AM variant for in vitro calibration.

Molecular fractions.

Let us consider the fluorescence decay of calcein in the presence of molecular crowding and in the presence of an amount of non-quenched calcein molecules ($c \neq 0$):

$$I(t) = a \exp\left(-\frac{\mathrm{t}}{\mathrm{\tau}}\right)\left[C + \exp\left(-2\frac{[Hb]}{[Hb]_0}\sqrt{t/\tau}\right)\right] \tag{S54}$$

The equation above is eq. 47 when scatter and IRF are neglected. The weight of the fluorescence decay for the non-quenched calcein is equal to:

$$w_{CA} = ca\tau \tag{S55}$$

The weight of the fluorescence decay for the quenched calcein is equal to:

$$w_{CA-Hb} = a\tau\left\{1 - \sqrt{\pi}\frac{[Hb]}{[Hb]_0}\exp\left(\frac{[Hb]^2}{[Hb]_0^2}\right)\mathrm{erfc}\left(\frac{[Hb]}{[Hb]_0}\right)\right\} \tag{S56}$$

Therefore eq. 48 can be inferred by computing $f_{\mathrm{Ca\text{-}Hb}} = w_{\mathrm{CA\text{-}Hb}} / (w_{\mathrm{CA\text{-}Hb}} + w_{\mathrm{CA\text{-}Hb}})$.

Appendix C: EXPMA – Quantifications and separate elemental Maps of Na, K, Cl, Fe and Mg

***Table S1 (overleaf): Results for the nystatin control experiment.** The EPXMA data is reported in the upper half of the table with two samples. The first one was frozen in the high-Na containing medium A, whereas the second sample was frozen after the $MgCl_2$ washes, preparing the cells for the selective electrode measurements (but before dilution and lysis in distilled water). The table reports the dry mass concentrations of Na, K and Fe as measured by EPXMA and gives the standard error of the mean. Additionally the number of cells analysed and the calculated Na/K ratio are shown. The lower half of the table reports the results for the selective ion electrode measurements, where estimates of the [Na] and [K] water concentrations are given. For comparison with the EPXMA data also the [Na]/[K] ratio is given.*

EPXMA	**n**	**C_{dry}(Na) (mmol/kg)**	**C_{dry}(K) (mmol/kg)**	**C_{dry}(Fe) (mmol/kg)**	**[Na]/[K]**	**Hb (mM)**
high K in solution A	30	166 ± 14	306 ± 3	66 ± 1	0.50 ± 0.04	5.4 ± 0.2
high Na in solution A	30	417 ± 9	63 ± 1	64 ± 1	6.6 ± 0.1	5.0 ± 0.3
high K in 110mM $MgCl_2$	20	73 ± 9	455 ± 16	121± 5	0.16 ± 0.02	8.7 ±0.3
high Na in 110mM $MgCl_2$	25	496 ± 14	86 ± 3	101 ± 2	5.8 ± 0.2	6.6 ± 0.2
Ion selective electrodes	**n**	**[Na] (mM)**	**[K] (mM)**		**[Na]/[K]**	
high K in 11mM $MgCl_2$	~10^9	<50	79		<0.6	
high Na in 11mM $MgCl_2$	~10^9	130	17		7.6	

Table S1

Sample	**n**	**C_{dry}(Na) (mmol/kg)**	**C_{dry}(K) (mmol/kg)**	**C_{dry}(Fe) (mmol/kg)**	**C_{dry}(P) (mmol/kg)**	**C_{dry}(S) (mmol/kg)**	**C_{dry}(Mg) (mmol/kg)**	**[Na]/[K]**	**[Hb] (mM)**
Controls	33	107 ± 13	374 ± 12	81 ± 2	91 ± 5	109 ± 7	47± 3	0.28 ± 0.03	6.5 ± 0.2
Cohorts of #4	5	78 ± 17	411 ± 18	77 ± 2	110±13	111±12	58 ±16	0.19 ±0.04	6.0 ± 0.5

Table S2: EPXMA data for uninfected RBCs. *The table reports the dry mass concentrations of Na, K, Fe, P, S and Mg as measured by EPXMA and gives the standard error of the mean. Additionally the number of cells analysed, the calculated Na/K ratio and the* $[Hb] = 150\cdot(c_{dry,Fe}/4)\cdot(c_{dry,Na}+c_{dry,K})^{-1}$ *are reported. The two samples were an uninfected control RBC sample and cohort RBCs from a mature trophozoite sample (sample #4 in table S3). While the existence of a parasite cannot be excluded in the latter sample (as the section was only 180 nm thick and the parasite could have resided above or below the visible section) the Fe, Na and K dry mass concentrations are very different from the infected cells from the same sample (compare Table S3 #4).*

Sample #	**n**	**C_{dry}(Na) (mmol/kg)**	**C_{dry}(K) (mmol/kg)**	**C_{dry}(Fe) (mmol/kg)**	**[Na]/[K]**	**Hb factor (mM)**	**Hb (mM)**
1 (17 Nov 08)	22	251 ± 78	273 ± 52	86 ± 16	0.92 ± 0.05	150	6.3 ± 0.2
2 (13 Oct 08)	9	204 ± 100	173 ±75	72 ± 12	1.53 ± 0.42	148	7.3 ± 0.5
3 1 Oct 08)	15	720 ± 348	96 ± 74	110 ± 34	9.6 ± 1.1	156.5	5.9 ± 0.6
4 (29 Jan 09)	40	634 ± 28	48 ± 4	81 ± 2	16.2 ± 1.2	156.5	4.9 ± 0.2
5 (23. June 09 #4)	15	592 ± 90	255 ± 42	83 ± 10	2.4 ± 0.4	156	3.9 ± 0.1
6 (23.06.09 #3)	11	379 ± 191	360 ± 130	90 ± 23	1.2 ± 0.1	153	5.0 ± 0.3
7 (23.06.09 #1)	28	924 ± 127	357 ± 68	124 ± 77	2.8 ± 0.1	156	4.1 ± 0.2
8 (23.06.09 #8)	15	996 ± 513	159 ± 70	88 ± 40	7.6 ± 1.7	156.5	3.3 ± 0.3

Table S3: EPXMA data for the IRBC host cytosol. *The table reports the dry mass concentrations of Fe, Na, K as measured by EPXMA, and gives the standard error of the mean. Additionally the number of cells analysed, the calculated Na/K ratio, reflecting the parasite stage, and the [Hb] are reported (graphed in Figure 4 and 5 A).*

Sample # (as in table 3)	**n**	**C_{dry}(Na) (mmol/kg)**	**C_{dry}(K) (mmol/kg)**	**C_{dry}(Fe) (mmol/kg)**	**C_{dry}(P) (mmol/kg)**	**C_{dry}(S) (mmol/kg)**	**[Na]/[K]**	**[Fe]/[K]**	**[P]/[K]**	**[S]/[K]**
1	11	255 ± 32	274 ± 21	85 ± 5	196 ± 12	218 ± 7	0.94 ± 0.09	**0.32 ± 0.01**	0.73 ± 0.04	0.83 ± 0.07
2	9	153 ± 35	483 ± 25	76 ± 16	515 ± 52	83 ± 10	0.34 ± 0.10	**0.17 ± 0.04**	1.08 ± 0.07	0.17 ± 0.02
3	14	269 ± 75	1640 ± 460	83 ± 23	1975 ± 550	167 ± 46	0.18 ± 0.03	**0.07 ± 0.02**	1.2 ± 0.3	0.10 ±0.03
4	10	216 ± 34	754 ± 51	34 ± 9	957 ± 78	106 ± 9	0.30 ± 0.05	**0.05 ± 0.01**	1.27 ± 0.10	0.14 ± 0.02
5	7	607 ± 22	261 ± 9	77 ± 4	248 ± 9	169 ± 56	2.3 ± 0.3	**0.30 ± 0.01**	0.95 ± 0.02	0.65 ± 0.22

Table S4: EPXMA data for the parasite cytosol. *The table reports the dry mass concentrations of Na, K, Fe, P, S as measured by EPXMA, and gives the standard error of the mean. Additionally the number of cells analysed and the calculated ratios of all elements with respect to* $C_{dry,Fe}$ *are reported. The sample numbering corresponds to the ones in Table S3. The Na/K ratio is similarly low as in uninfected RBC and is maintained at a gradient with respect to the host cytosol (compare Table S3).*

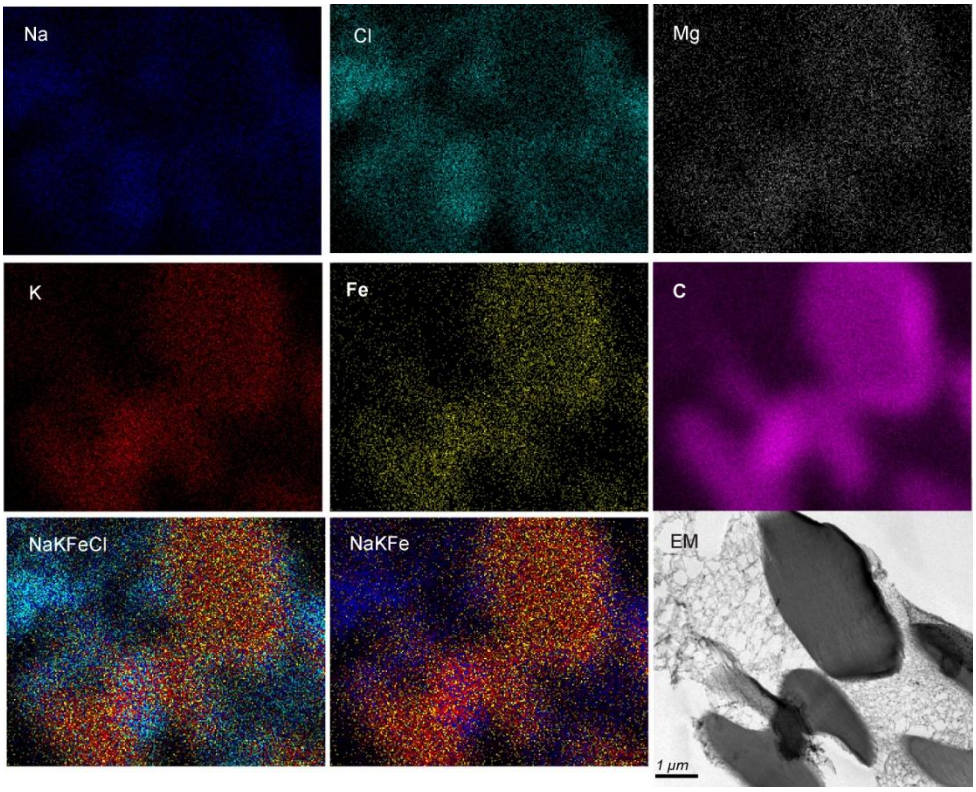

Figure 45: Separate elemental X-ray maps and electronmicrograph from which Figure 2A and 2B were derived. *The upper six panels represent the distribution of Na, Cl, Mg, K, Fe and C in the uninfected control RBC sample. The lower left panel is an overlay of the Na, K, Fe and Cl distribution, where the strongest elemental pixel sets the pixel colour for the overlay image. The lower middle panel was derived with the same method, but includes only Na, K and Fe. The lower right panel shows the corresponding electron micrograph.*

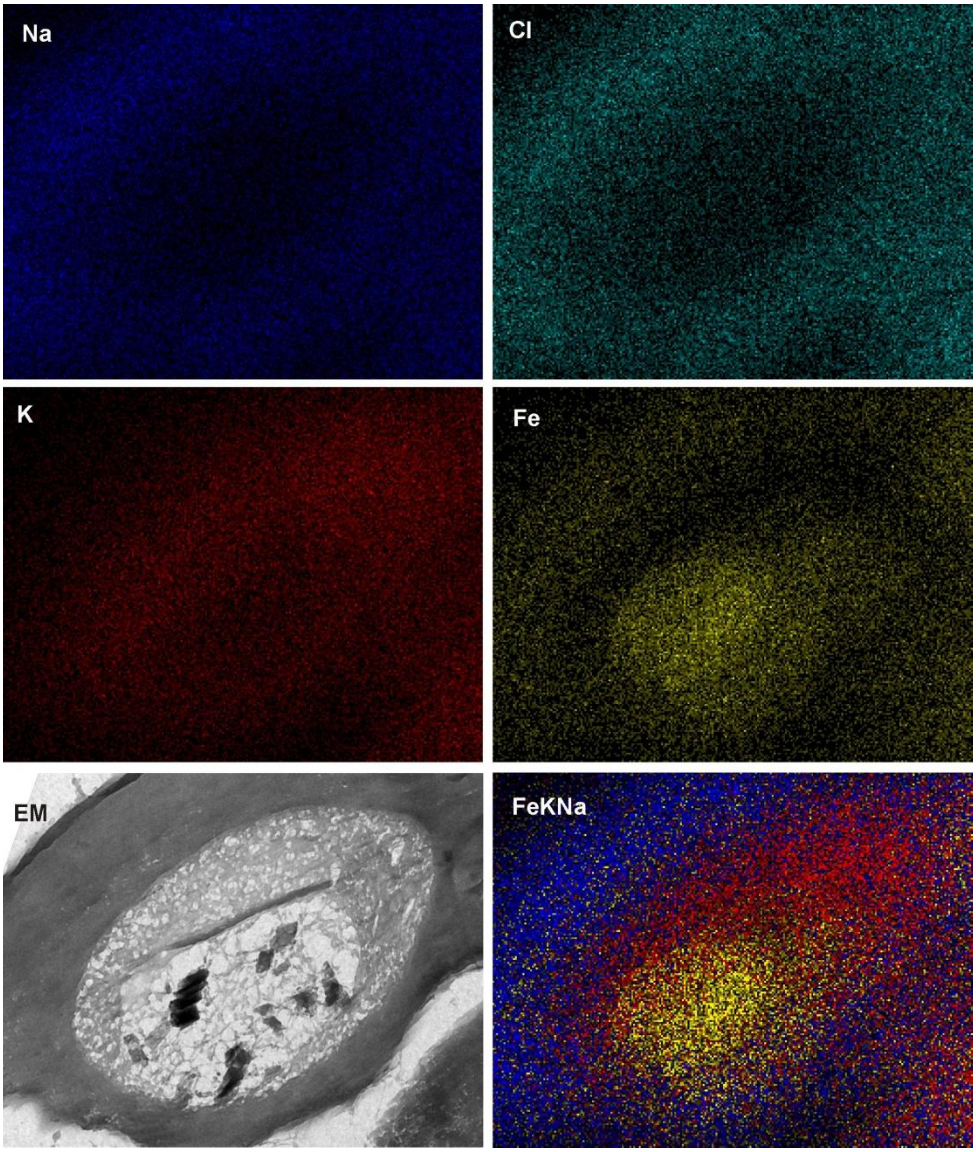

Figure 46: Separate elemental X-ray maps and electronmicrograph from which Figure 2C and 2D were derived. *The upper four panels represent the distribution of Na, Cl, K and Fe of a mature trophozoite IRBC (Sample 4 from Table S3). The lower left panel shows the corresponding electronmicrograph. The lower right panel is an overlay of the Na, K and Fe distribution, where the strongest elemental pixel sets the pixel colour for the overlay image.*

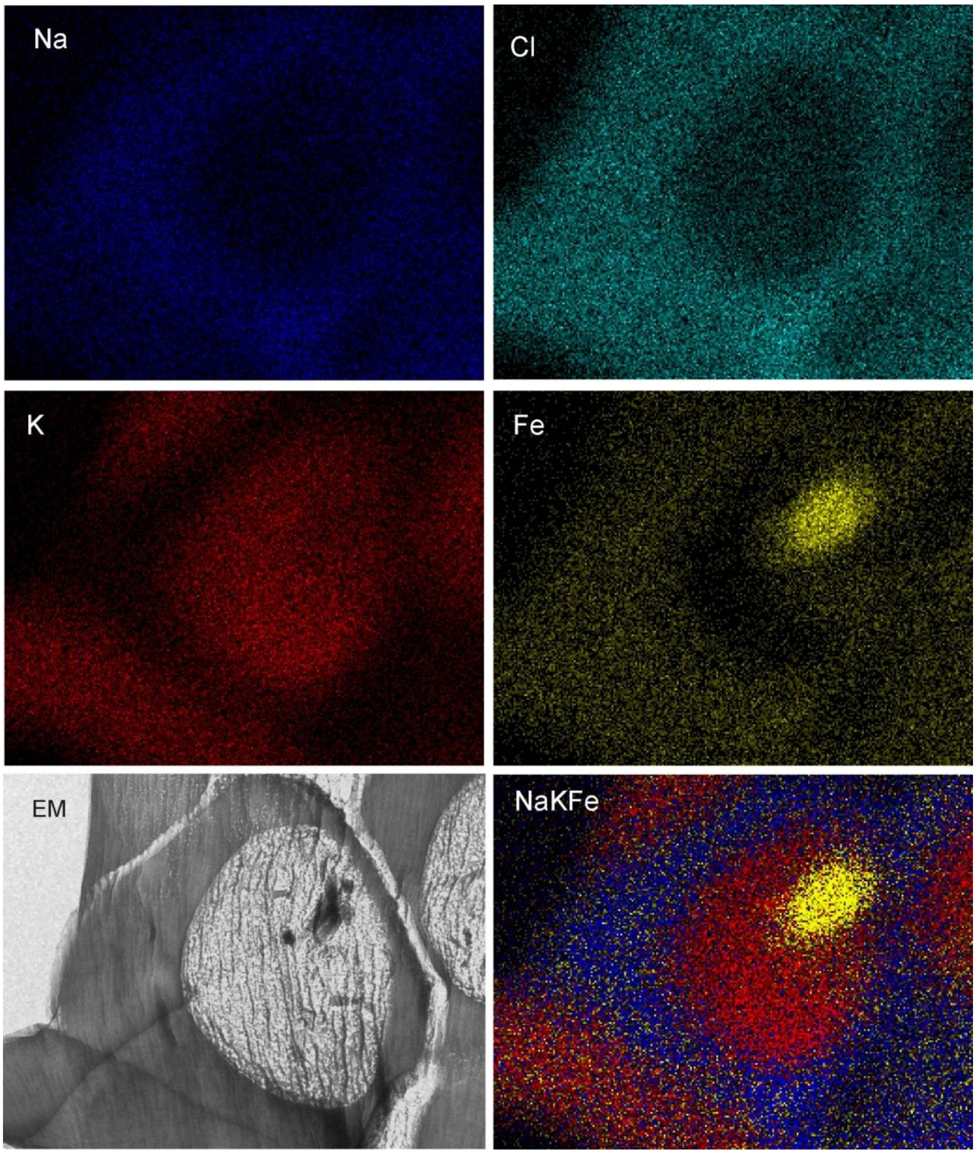

Figure 47: Separate elemental X-ray maps and electronmicrograph from which Figure 2E and 2F were derived. *The upper six and the lower right panel represent the distribution of Na, Cl, Mg, K, Fe, O and C of a mature trophozoite sample that was briefly washed in isotonic* $MgCl_2$ *before freezing, to remove all Na and K signal contribution from the extracellular medium. The lower left panel shows the corresponding electronmicrograph. The image shows two IRBC fragments with a parasite visible in the section and two smaller fragments of uninfected RBCs. The*

lower middle panel is an overlay of the Na, K and Fe distribution, where the strongest elemental pixel sets the pixel colour for the overlay image and the uninfected RBC cytosol can be clearly distinguished from the host cytosol.

Appendix D: Additional Figures of the Volume rendering and calculations of osmotic fragility

Additional Figures.

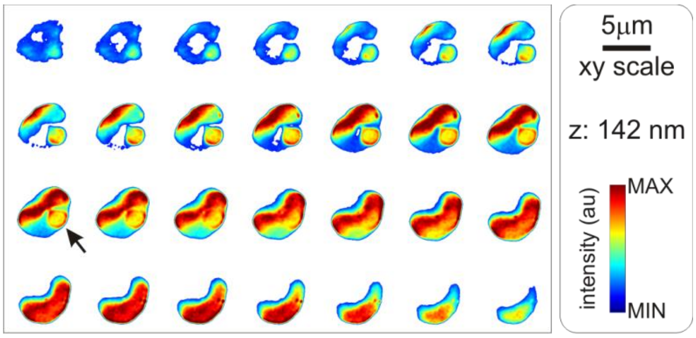

Figure 48. Confocal imaging of a cohort RBC with merozoite attached*. The arrow shows a merozoite attached to the surface of the cohort RBC, ready to invade its host.*

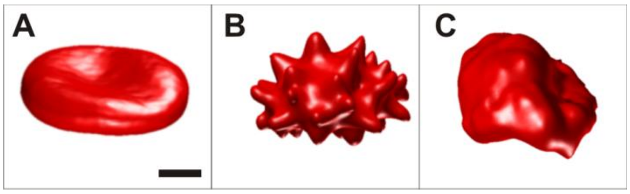

Figure 49. Examples of three dimensional rendering of normal, crenated and infected RBCs by the fit-assisted algorithm.

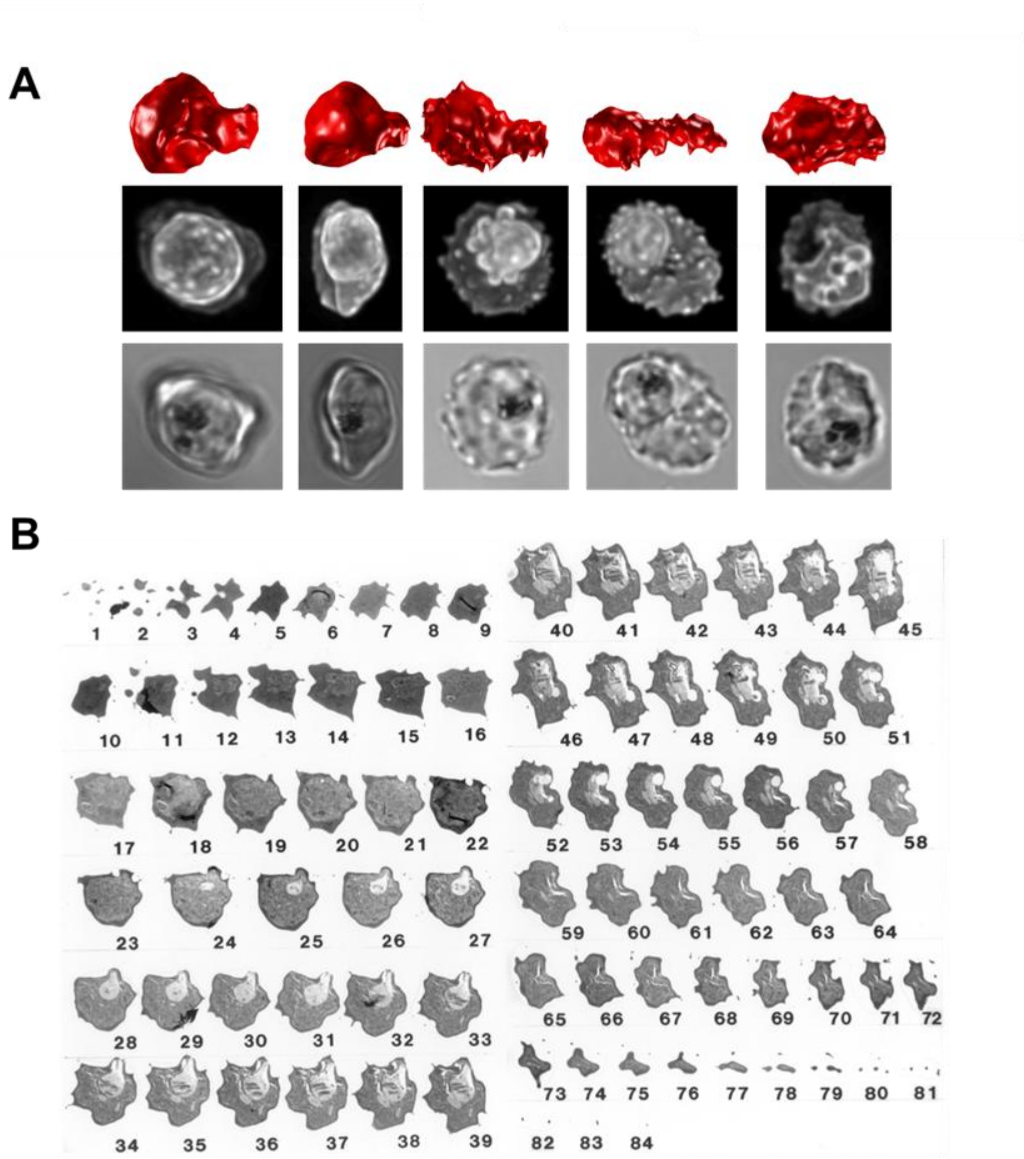

Figure 50*. Variety of shapes observed in red blood cells infected with late-stage parasites**. ***A. *Selected 3D rendered images (in red) are shown above the corresponding maximum-intensity projection of the deconvolved confocal 3D image stacks (second row) and transmission images (third row). Note the relatively smooth appearance of the surface bulges in the first two cells and the more spiky appearance of a substantial proportion of the membrane surface in the last three cells. The dark haemozoin pigment in the transmission images (third row) indicates the position of the food*

vacuole (residual body) in each cell. ***B.*** *Electron-micrograph of a schizont; serial section. Sample processed for electronmicroscopy and serial sectioning as detailed before (31, 32). Note the relatively smooth appearance of the membrane in the regions where the parasite occupies most of the cell volume (i.e frames 23 to 30), and the increased frequency of spikes in membrane regions distal to the parasite (i.e. frame 40 onwards).*

Effect of surface area variations on osmotic fragility.

The relative tonicity at lysis depends on the fractional water volume (w) of a RBC and on its critical haemolytic volume (CHV), *i.e.*, the ratio between the maximum volume that a RBC can contain within its plasma membrane of surface area A_C and its physiological volume (V_C).

The goal is to estimate the shift in osmotic fragility expected from the documented loss in membrane area in IRBCs. With the same equations, the surface area loss can be inferred that would both justify the new volume measurements and the previous osmotic fragility shifts observed. In such cells w is predicted to be substantially decreased at schizont stage to about 0.5 from an original level of about 0.7 in uninfected RBCs (Saliba et al., 1998).

$$RT_L = \frac{w}{CHV-1+w} \tag{S57}$$

$$CHV = \frac{A_{RBC}^{3/2}}{6\sqrt{\pi}V_{RBC}} \tag{S58}$$

For a fractional variation of plasma membrane surface area f, CHV will shift at lower values accordingly to the following power law:

$$CHV' = \frac{[A_{RBC}(1-f)]^{3/2}}{6\sqrt{\pi}V_{RBC}} = CHV(1-f)^{3/2} \tag{S59}$$

Therefore, the RT_L will be shifted to higher values:

$$RT_L' = \frac{w}{CHV(1-f)^{3/2}-1+w} \qquad \text{(S60)}$$

For *w* values of 0.7 and 0.5, *f* = 0.18 and CHV of 1.7, the resulting RT_L values for cohorts and IRBCs with late-schizont parasites is 0.5 and 0.6, respectively. On the other hand, for values of RT_L' within the 0.8-0.9 range (Lew et al., 2004) and *w* = 0.5, an expected reduction of surface area amounts to *f* = 0.24-0.27.

Appendix E: The Optical Cell Stretcher – Calculations and Chemistry

The width of the trapping region of the cell stretcher

The trapping region diameter in the stretcher was calculated with the ABCD-Matrix method. This method is valid for optical calculations of near-axis rays and is described in (Meschede, 2005). A Gaussian TEM_{00} mode

$$E(z,\rho) \approx \frac{A}{kq_i(z)} \exp\left(i\frac{k\rho^2}{2q_i(z)}\right) e^{-ikz} \qquad \text{(S61)}$$

with a complex

$$q_i(z) = \frac{1}{R(z)} + i\frac{2}{k\omega^2(z)}, \qquad \text{(S62)}$$

(index i denotes initial state), is assumed to exit the optical fibre in its Rayleigh zone at $z=0$ with half-width ω_0, curvature $R_0=\infty$ and Rayleigh length $z_0 = \omega^2 \cdot \pi \cdot n \cdot \lambda^{-1}$. A propagation of length z of the TEM_{00} mode is described by the matrix:

$$T_{prop} = \begin{pmatrix} 1 & z \\ 0 & 1 \end{pmatrix}, \qquad \text{(S63)}$$

and a refraction of the mode from material 1 into material 2 with a surface curvature of R_1 is represented by the matrix:

$$T_{ref} = \begin{pmatrix} 1 & 0 \\ \frac{n_1 - n_2}{R_1 n_2} & \frac{n_1}{n_2} \end{pmatrix}, \qquad \text{(S64)}$$

where n represents the refractive index. In the case of the optical stretcher, the mode propagates in the optical gel from the end of the fibre until it reaches the glass capillary, where it is refracted, propagates further and is refracted again upon entering the cell suspension. Finally it propagates to the middle of the capillary where it reaches the trapped cell. The transfer matrix for this system can now be calculated by

$$T = T_{prop,gel} \otimes T_{ref,glass} \otimes T_{prop,glass} \otimes T_{ref,water} \otimes T_{prop,water}\ , \qquad \text{(S65)}$$

with the linear matrix operator transforming a mode as

$$q_f = T \otimes q_i = \frac{T_{11} q_0 + T_{12}}{T_{21} q_0 + T_{22}}. \qquad \text{(S66)}$$

For the calculations, the following parameters were used (taken from the manufacturers specifications, distances measured with a stage micrometer): ω_0=3.3 µm; n_{gel}=1.449; n_{glass}=1.474; n_{med}=1.335; z_{glass}=50 µm; $R_1=\infty$; z_{gel}=30 µm; z_{med}=50 µm; λ=1.07 µm. The optical trapping region has the width of the waist radius of the final state (index *f*), which can than be calculated to be:

$$\omega_f^2 = \frac{\lambda}{\pi} \left(Im \left\{ \frac{1}{q_f} \right\} \right)^{-1} \approx (14 \mu m\ )^2. \qquad \text{(S67)}$$

Ellipse fitting of the cell edges

The following equation on the polar coordinates *(r, θ)* describes a general ellipse with semidiameters *a* and *b*, centred at a point (r_0, θ_0), with the *a* axis rotated by *φ* relative to the polar axis:

$$r(\theta) = \frac{P(\theta) + Q(\theta)}{R(\theta)}, \qquad \text{(S68)}$$

where

$$P(\theta) = r_0\big((b^2 - a^2)\cos(\theta - \theta_0 - 2\varphi) + (a^2 + b^2)\cos(\theta - \theta_0)\big), \qquad \text{(S69)}$$

$$Q(\theta) = ab\sqrt{2(R(\theta) - 2r_0^2 \sin^2(\theta - \theta_0))}, \qquad \text{(S70)}$$

$$R(\theta) = (b^2 - a^2)\cos(2\theta - -2\varphi) + a^2 + b^2. \qquad \text{(S71)}$$

These equations were implemented into a Matlab algorithm to extract the main axis of the ellipse fit in the stretcher experiments and calculate the strain $\varepsilon = a(t)/a_o$.

The mechanism of SU-8 polymerisation

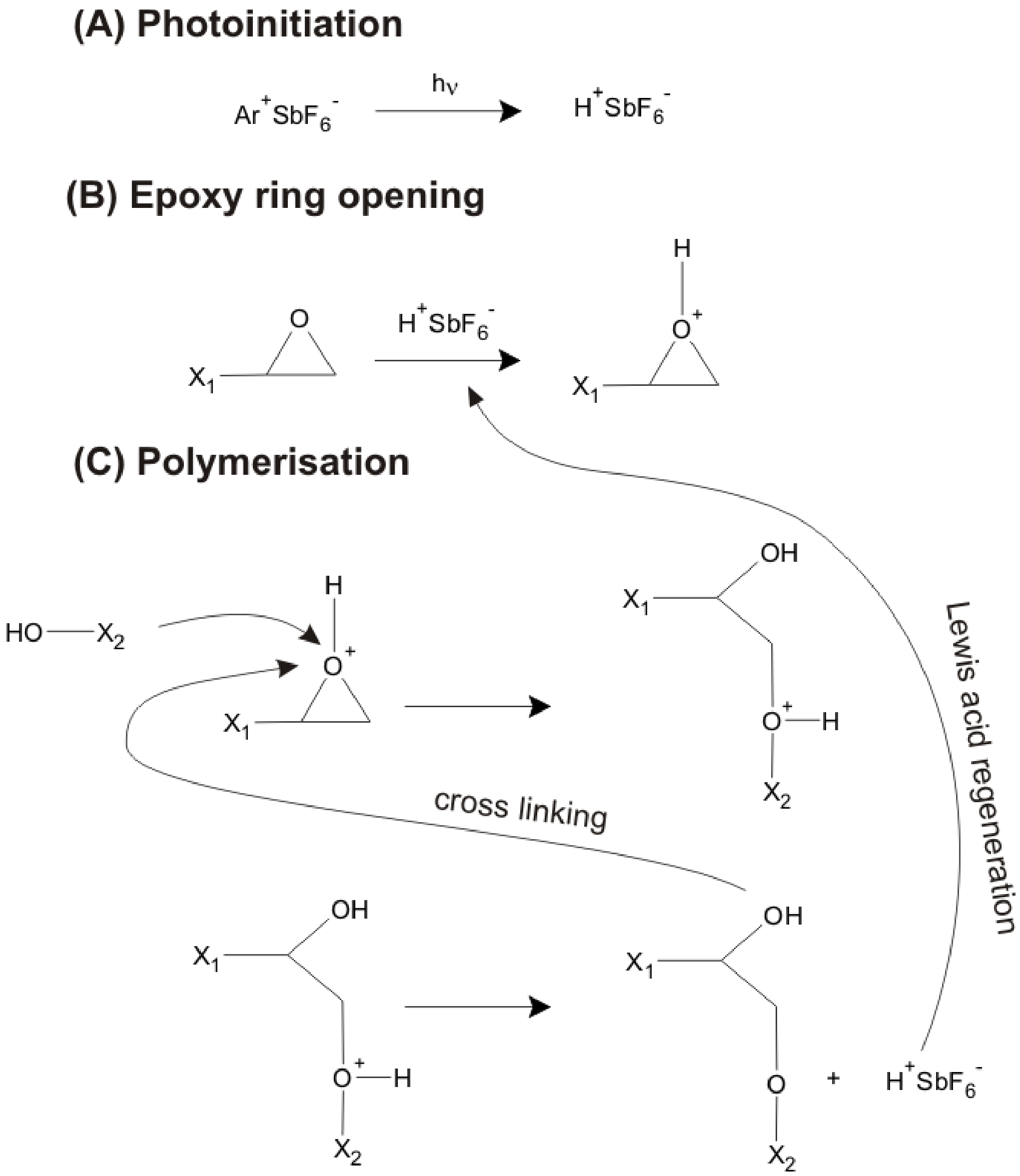

Figure 51: Mechanism of SU-8 polymerisation.

SU-8 consists of an epoxy resin (EPON 815)[1], a cationic photoinitiator[2] and a solvent[3]. The cross-linking reaction occurs through reactive epoxy groups under UV light irradiation, which converts the epoxy groups into ethers and aliphatic hydroxyls. (Crivello and Liu, 1998; Sikanen et al., 2005; Anhoj et al., 2006). The reaction is triggered by UV irradiation and breakdown of the cationic photoinitiatior salt (Figure 51A), which than becomes a very strong Lewis acid. This Lewis acid in turn protonates the epoxy ring, that has now a positive surplus charge, making it susceptible to further reaction (Figure 51B). The epoxy ring opens by binding to a hydroxyl group of a second resin molecule. The proton (and the surplus charge) of the hydroxyl group is released and regenerates the Lewis acid, which protonates another epoxy ring in its proximity (Figure 51C),. By repeating this step, the polymerisation continues.

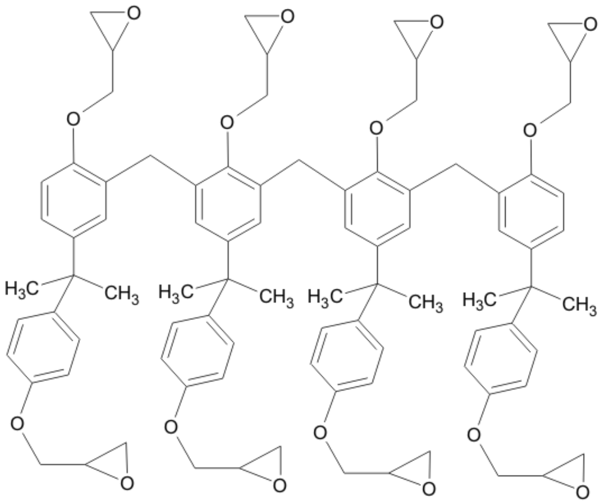

Figure 52: The polymeric structure of SU-8.

---

[1] 4,4'-(1-methylethylidene)bis-[phenol] with (butoxymethyl)oxirane and (chloromethyl)oxirane

[2] triarylsulfonium salts of hexafluoroantimonate

[3] cyclopentanone

SU-8 is a mechanically very durable material. Figure 52 shows its molecular structure. Feature size accuracy of SU-8 structures depend on the wavelength of the UV light used and on the accuracy of the mask (printer). Common pitfalls during SU-8 fabrications are cracking of the layer during baking and detachment from the substrate (glass or silicon wafers).

List of References

Adair, G. S. (1929). "The Thermodynamic Analysis of the Observed Osmotic Pressures of Protein Salts in Solutions of Finite Concentration." Proceedings of the Royal Society of London. Series A **126**(800): 16-24.

Allen, R. J. and K. Kirk (2004). "Cell volume control in the Plasmodium-infected erythrocyte." Trends Parasitol **20**(1): 7-10; discussion 10-1.

Alonso, P. L., J. Sacarlal, et al. (2005). "Duration of protection with RTS,S/AS02A malaria vaccine in prevention of Plasmodium falciparum disease in Mozambican children: single-blind extended follow-up of a randomised controlled trial." Lancet **366**(9502): 2012-8.

Alonso, P. L., J. Sacarlal, et al. (2004). "Efficacy of the RTS,S/AS02A vaccine against Plasmodium falciparum infection and disease in young African children: randomised controlled trial." Lancet **364**(9443): 1411-20.

Anhoj, T. A., A. M. Jorgensen, et al. (2006). "The effect of soft bake temperature on the polymerization of SU-8 photoresist." Journal of Micromechanics and Microengineering **16**(9): 1819-1824.

Ashkin, A. (1970). "Acceleration and Trapping of Particles by Radiation Pressure." Physical Review Letters **24**(4): 156-&.

Ashkin, A. (1992). "Forces of a Single-Beam Gradient Laser Trap on a Dielectric Sphere in the Ray Optics Regime." Biophysical Journal **61**(2): 569-582.

Ashkin, A. and J. M. Dziedzic (1973). "Radiation Pressure on a Free Liquid Surface." Physical Review Letters **30**(4): 139-142.

Ashkin, A. and J. M. Dziedzic (1987). "Optical Trapping and Manipulation of Viruses and Bacteria." Science **235**(4795): 1517-1520.

Atamna, H. and H. Ginsburg (1997). "The malaria parasite supplies glutathione to its host cell--investigation of glutathione transport and metabolism in human erythrocytes infected with Plasmodium falciparum." Eur J Biochem **250**(3): 670-9.

Awaya, T. (1979). "New Method for Curve Fitting to the Data with Low Statistics Not Using the Chi-2-Method." Nuclear Instruments & Methods **165**(2): 317-323.

Barber, P. R., S. M. Ameer-Beg, et al. (2005). Global and pixel kinetic data analysis for FRET detection by multi-photon time-domain FLIM. Multiphoton Microscopy in the Biomedical Sciences V, San Jose, CA, USA, SPIE.

Bartoli, A. (1884). "Il calorico raggiante e il secondo principio di termodinamica." Il nuovo cimento **15**: 193-202.

Becker, W. (2005). Advanced Time-Correlated Single Photon Counting Techniques Berlin, London, Springer.

Becker, W. (2010). The bh TCSPC Handbook. Berlin, Becker & Hickl GmbH.

Becker, W., A. Bergmann, et al. (2004). "Fluorescence lifetime imaging by time-correlated single-photon counting." Microsc Res Tech **63**(1): 58-66.

Begenisich, T., T. Nakamoto, et al. (2004). "Physiological roles of the intermediate conductance, Ca2+-activated potassium channel Kcnn4." J Biol Chem **279**(46): 47681-7.

Beghetto, C., C. Renken, et al. (2000). "Implications of the generation of reactive oxygen species by photoactivated calcein for mitochondrial studies." European journal of biochemistry / FEBS **267**(17): 5585-92.

Bell, M. and S. E. Green (1933). "On radiometer action and the pressure of radiation." Proc. Phys. Soc. **45**: 320.

Bennett, R. G. (1964). "Radiationless intermolecular energy transfer. I. Singlet -> Singlet tranfer." The Journal of Chemical Physics **41**(10): 3037-3040.

Berendt, A. R., D. L. Simmons, et al. (1989). "Intercellular adhesion molecule-1 is an endothelial cell adhesion receptor for Plasmodium falciparum." Nature **341**(6237): 57-59.

Block, S. M., L. S. B. Goldstein, et al. (1990). "Bead Movement by Single Kinesin Molecules Studied with Optical Tweezers." Nature **348**(6299): 348-352.

Bookchin, R. M., D. J. Lew, et al. (1984). "Dehydration and delayed proton equilibria of red blood cells suspended in isosmotic phosphate buffers. Implications for studies of sickled cells." J Lab Clin Med **104**(6): 855-66.

Bookchin, R. M., O. E. Ortiz, et al. (1991). "Evidence for a direct reticulocyte origin of dense red cells in sickle cell anemia." J Clin Invest **87**(1): 113-24.

Boutet de Monvel, J., S. Le Calvez, et al. (2001). "Image restoration for confocal microscopy: improving the limits of deconvolution, with application to the visualization of the mammalian hearing organ." Biophys J **80**(5): 2455-70.

Bouyer, G., S. Egee, et al. (2007). "Toward a unifying model of malaria-induced channel activity." Proc Natl Acad Sci U S A **104**(26): 11044-9.

Boyde, L., K. J. Chalut, et al. (2009). "Interaction of Gaussian beam with near-spherical particle: an analytic-numerical approach for assessing scattering and stresses." J Opt Soc Am A Opt Image Sci Vis **26**(8): 1814-26.

Breman, J. G., M. S. Alilio, et al. (2004). "Conquering the intolerable burden of malaria: what's new, what's needed: a summary." Am J Trop Med Hyg **71**(2 Suppl): 1-15.

Bureau, M. and R. Banerjee (1976). "Structure-volume relationships in hemoglobin. A densitometric and dilatometric study of the oxy leads to deoxy transformation." Biochimie **58**(4): 403-7.

Cass, A. and M. Dalmark (1973). "Equilibrium dialysis of ions in nystatin-treated red cells." Nat New Biol **244**(132): 47-9.

CDC. (2008). "Center for Disease Control: Malaria ", website accessed 23.07.2010, from http://www.cdc.gov/malaria/.

Choi, W., C. Fang-Yen, et al. (2007). "Tomographic phase microscopy." Nat Methods **4**(9): 717-9.

Chu, S. (1991). "Laser Manipulation of Atoms and Particles." Science **253**(5022): 861-866.

Clayton, A. H., Q. S. Hanley, et al. (2004). "Graphical representation and multicomponent analysis of single-frequency fluorescence lifetime imaging microscopy data." Journal of Microscopy **213**(Pt 1): 1-5.

Constable, A., J. Kim, et al. (1993). "Demonstration of a fiber-optical light-force trap." Opt Lett **18**(21): 1867-9.

Cooke, B. M., K. Lingelbach, et al. (2004). "Protein trafficking in Plasmodium falciparum-infected red blood cells." Trends Parasitol **20**(12): 581-9.

Cranston, H. A., C. W. Boylan, et al. (1984). "Plasmodium falciparum maturation abolishes physiologic red cell deformability." Science **223**(4634): 400-3.

Crivello, J. V. and S. Liu (1998). "Free Radical Induced Acceleration of Cationic Photopolymerization." Chemistry of Materials **10**(11): 3724-3731.

Crookes, W. (1874). "On Attraction and Repulsion Resulting from Radiation." Phil. Trans. R. Soc. **164**: 501-527.

Da Silva, A. J. and M. Moser. (2002). "Malaria life cycle." Centre for Disease Control, Public health image library http://phil.cdc.gov/phil/home.asp, Id#3405. 2010, from http://www.dpd.cdc.gov/dpdx/HTML/Malaria.htm.

Dalmark, M. (1975). "Chloride and water distribution in human red cells." J Physiol **250**(1): 65-84.

De Mairan, J.-J. D. (1754). "Traité physique et historique de l'aurore boréale." Académie Royale des Sciences.

Desai, S. A., S. M. Bezrukov, et al. (2000). "A voltage-dependent channel involved in nutrient uptake by red blood cells infected with the malaria parasite." Nature **406**(6799): 1001-5.

Difato, F., F. Mazzone, et al. (2004). "Improvement in volume estimation from confocal sections after image deconvolution." Microsc Res Tech **64**(2): 151-5.

Digman, M., V. R. Caiolfa, et al. (2007). "The Phasor approach to fluorescence lifetime imaging analysis." Biophysical Journal **94**(2): L14-16.

Dondorp, A. M., B. J. Angus, et al. (1997). "Prognostic significance of reduced red blood cell deformability in severe falciparum malaria." American Journal of Tropical Medicine and Hygiene **57**(5): 507-511.

Dondorp, A. M., P. A. Kager, et al. (2000). "Abnormal blood flow and red blood cell deformability in severe malaria." Parasitology Today **16**(6): 228-232.

Dondorp, A. M., E. Pongponratn, et al. (2004). "Reduced microcirculatory flow in severe falciparum malaria: pathophysiology and electron-microscopic pathology." Acta Trop **89**(3): 309-17.

Dunn, M. J. (1969). "Alterations of red blood cell sodium transport during malarial infection." J Clin Invest **48**(4): 674-84.

Dyrda, A., U. Cytlak, et al. (2010). "Local membrane deformations activate Ca2+-dependent K+ and anionic currents in intact human red blood cells." PLoS One **5**(2): e9447.

Egee, S., F. Lapaix, et al. (2002). "A stretch-activated anion channel is up-regulated by the malaria parasite Plasmodium falciparum." J Physiol **542**(Pt 3): 795-801.

Ekpenyong, A. E., C. L. Posey, et al. (2009). "Determination of cell elasticity through hybrid ray optics and continuum mechanics modeling of cell deformation in the optical stretcher." Appl. Opt. **48**(32): 6344-6354.

Elder, A. D., A. Domin, et al. (2009). "A quantitative protocol for dynamic measurements of protein interactions by Forster resonance energy transfer-sensitized fluorescence emission." Journal of the Royal Society Interface **6**: S59-S81.

Elder, A. D., J. H. Frank, et al. (2006). "Calibration of a wide-field frequency-domain fluorescence lifetime microscopy system using light emitting diodes as light sources." Journal of Microscopy-Oxford **224**: 166-180.

Elder, A. D., S. M. Matthews, et al. (2006). "The application of frequency-domain Fluorescence Lifetime Imaging Microscopy as a quantitative analytical tool for microfluidic devices." Optics Express **14**(12): 5456-5467.

Elliott, D. A., M. T. McIntosh, et al. (2008). "Four distinct pathways of hemoglobin uptake in the malaria parasite Plasmodium falciparum." Proc Natl Acad Sci U S A **105**(7): 2463-8.

Elliott, J. L., K. J. Saliba, et al. (2001). "Transport of lactate and pyruvate in the intraerythrocytic malaria parasite, Plasmodium falciparum." Biochem J **355**(Pt 3): 733-9.

Esposito, A., J. B. Choimet, et al. (2010). "Quantitative imaging of human red blood cells infected with Plasmodium falciparum." Biophys J **99**(3): 953-60.

Esposito, A., H. C. Gerritsen, et al. (2007). Fluorescence lifetime imaging microscopy: quality assessment and standards. Standardization in Fluorometry: State of the Art and Future Challenges. O. S. Wolfbeis. Berlin Heidelberg New York, Springer.

Esposito, A., T. Tiffert, et al. (2008). "FRET Imaging of Hemoglobin Concentration in Plasmodium falciparum-Infected Red Cells." PLoS ONE **3**(11): e3780.

Esposito, A., F. S. Wouters, et al. (2004). Fluorescence Lifetime Imaging Microscopy. Current Protocols in Cell Biology.

Evans, E. and Y. C. Fung (1972). "Improved measurements of the erythrocyte geometry." Microvasc Res **4**(4): 335-47.

Fang, S., Y. Dai, et al. (2000). "Three-dimensional microscopy data exploration by interactive volume visualization." Scanning **22**(4): 218-26.

Fernandez-Segura, E. and A. Warley (2008). "Electron probe X-ray microanalysis for the study of cell physiology." Methods Cell Biol **88**: 19-43.

Flatman, P. W. and V. L. Lew (1979). "The magnesium-dependence of sodium:potassium and sodium:sodium exchange mediated by the sodium pump in intact human red cells [proceedings]." J Physiol **287**: 33P-34P.

Förster, T. (1948). "Zwischenmolekulare Energiewanderung und Fluoreszenz." **437**(1-2): 55-75.

Frank, J. H., A. D. Elder, et al. (2007). "A white light confocal microscope for spectrally resolved multidimensional imaging." Journal of Microscopy: 203-15.

Freedman, J. C. and J. F. Hoffman (1979). "Ionic and Osmotic Equilibria of Human Red Blood-Cells Treated with Nystatin." Journal of General Physiology **74**(2): 157-185.

Freeman, C. J., R. M. Bookchin, et al. (1987). "K-permeabilized human red cells lose an alkaline, hypertonic fluid containing excess K over diffusible anions." J Membr Biol **96**(3): 235-41.

Frischknecht, F. and M. Lanzer (2008). "The Plasmodium falciparum Maurer's clefts in 3D." Mol Microbiol **67**(4): 687-91.

Funder, J. and J. O. Wieth (1966). "Chloride and Hydrogen Ion Distribution between Human Red Cells and Plasma." Acta Physiologica Scandinavica **68**(2): 234-245.

Garcia-Sancho, J. (1985). "Pyruvate prevents the ATP depletion caused by formaldehyde or calcium-chelator esters in the human red cell." Biochimica et biophysica acta **813**(1): 148-50.

Gardos, G. (1958). "The function of calcium in the potassium permeability of human erythrocytes." Biochim Biophys Acta **30**(3): 653-4.

Garrahan, P. J. and R. P. Garay (1974). "A kinetic study of the Na pump in red cells: its relevance to the mechanism of active transport." Ann N Y Acad Sci **242**(0): 445-58.

Garrahan, P. J. and I. M. Glynn (1967). "Facftors affecting the relative magnitudes of the sodium:potassium and sodium:sodium exchanges catalysed by the sodium pump." J Physiol **192**(1): 189-216.

Gerthsen, C. and D. Meschede (2002). Gerthsen Physik. Berlin, Springer.

Gilboa, H., B. E. Chapman, et al. (1994). "19F NMR magnetization transfer between 5-FBAPTA and its complexes. An alternative means for measuring free Ca2+ concentration, and detection of complexes with protein in erythrocytes." NMR Biomed **7**(7): 330-8.

Ginsburg, H. (1988). How and why does the malarial parasite permeabilize its host cell membrane? Biomembranes: Basic & Medical Research. G. H. Benga and J. M. Trager. Berlin, Springer-Verlag**:** 188-203.

Ginsburg, H., S. Handeli, et al. (1986). "Effects of red blood cell potassium and hypertonicity on the growth of Plasmodium falciparum in culture." Z Parasitenkd **72**(2): 185-99.

Ginsburg, H., M. Krugliak, et al. (1983). "New permeability pathways induced in membranes of Plasmodium falciparum infected erythrocytes." Mol Biochem Parasitol **8**(2): 177-90.

Ginsburg, H., S. Kutner, et al. (1985). "Characterization of permeation pathways appearing in the host membrane of Plasmodium falciparum infected red blood cells." Mol Biochem Parasitol **14**(3): 313-22.

Ginsburg, H. and W. D. Stein (1987). "New permeability pathways induced by the malarial parasite in the membrane of its host erythrocyte: potential routes for targeting of drugs into infected cells." Biosci Rep **7**(6): 455-63.

Ginsburg, H. and W. D. Stein (2004). "The new permeability pathways induced by the malaria parasite in the membrane of the infected erythrocyte: comparison of results using different experimental techniques." J Membr Biol **197**(2): 113-34.

Ginsburg, H., S. A. Ward, et al. (1999). "An integrated model of chloroquine action." Parasitol Today **15**(9): 357-60.

Glenister, F. K., R. L. Coppel, et al. (2002). "Contribution of parasite proteins to altered mechanical properties of malaria-infected red blood cells." Blood **99**(3): 1060-1063.

Glenister, F. K., K. M. Fernandez, et al. (2009). "Functional alteration of red blood cells by a megadalton protein of Plasmodium falciparum." Blood **113**(4): 919-28.

Glushakova, S., D. Yin, et al. (2007). "Quantification of malaria parasite release from infected erythrocytes: inhibition by protein-free media." Malar J **6**: 61.

Glushakova, S., D. Yin, et al. (2005). "Membrane transformation during malaria parasite release from human red blood cells." Curr Biol **15**(18): 1645-50.

Griffiths, M. J., F. Ndungu, et al. (2001). "Oxidative stress and erythrocyte damage in Kenyan children with severe Plasmodium falciparum malaria." Br J Haematol **113**(2): 486-91.

Guck, J., R. Ananthakrishnan, et al. (2001). "The optical stretcher: A novel laser tool to micromanipulate cells." Biophysical Journal **81**(2): 767-784.

Guck, J., R. Ananthakrishnan, et al. (2000). "Optical deformability of soft biological dielectrics." Phys Rev Lett **84**(23): 5451-4.

Guck, J., S. Schinkinger, et al. (2005). "Optical deformability as an inherent cell marker for testing malignant transformation and metastatic competence." Biophys J **88**(5): 3689-98.

Gupta, B. L. and M. G. Roomans (1993). X-Ray Microprobe Analysis of Chemical Elements in Biology. Chicago, Scanning Microscopy International.

Hamann, S., J. F. Kiilgaard, et al. (2002). "Measurement of cell volume changes by fluorescence self-quenching." Journal of Fluorescence **12**(2): 139-145.

Hanssen, E., R. Sougrat, et al. (2008). "Electron tomography of the Maurer's cleft organelles of Plasmodium falciparum-infected erythrocytes reveals novel structural features." Mol Microbiol **67**(4): 703-18.

Harrison, D. G. and C. Long (1968). "The calcium content of human erythrocytes." J Physiol **199**(2): 367-81.

Hochmuth, R. M. and R. E. Waugh (1987). "Erythrocyte membrane elasticity and viscosity." Annu Rev Physiol **49**: 209-19.

Horecker, B. L. (1943). "The absorption spectra of hemoglobin and its derivatives in the visible and near infra-red regions." J. Biol. Chem. **148**(1): 173-183.

Jackson, J. D. (1975). Classical Electrodynamics. New York, John Wiley & Sons.

Jacobs, M. H. and D. R. Stewarts (1947). "Osmotic properties of the erythrocyte. XII. Ionic and osmotic equilibria with a complex external solution." J. Cell. Comp. Physiology **30**: 79-103.

Jensen, J. B. (1978). "Concentration from continuous culture of erythrocytes infected with trophozoites and schizonts of Plasmodium falciparum." Am J Trop Med Hyg **27**(6): 1274-6.

Kaestner, L., W. Tabellion, et al. (2006). "Calcium imaging of individual erythrocytes: problems and approaches." Cell Calcium **39**(1): 13-9.

Kaminski, C. F., R. S. Watt, et al. (2008). "Supercontinuum radiation for applications in chemical sensing and microscopy." Applied Physics B-Lasers and Optics **92**(3): 367-378.

Kanaani, J. and H. Ginsburg (1988). "Compartment analysis of ATP in malaria-infected erythrocytes." Biochem Int **17**(3): 451-9.

Kanaani, J. and H. Ginsburg (1989). "Metabolic interconnection between the human malarial parasite Plasmodium falciparum and its host erythrocyte. Regulation of ATP levels by means of an adenylate translocator and adenylate kinase." J Biol Chem **264**(6): 3194-9.

Kanaani, J. and H. Ginsburg (1991). "Transport of lactate in Plasmodium falciparum-infected human erythrocytes." J Cell Physiol **149**(3): 469-76.

Kirk, K. (2001). "Membrane transport in the malaria-infected erythrocyte." Physiol Rev **81**(2): 495-537.

Kirk, K., H. M. Staines, et al. (1999). "Transport properties of the host cell membrane." Novartis Found Symp **226**: 55-66; discussion 66-73.

Kiszewski, A., A. Mellinger, et al. (2004). "A global index representing the stability of malaria transmission." Am J Trop Med Hyg **70**(5): 486-98.

Krugliak, M. and H. Ginsburg (2006). "The evolution of the new permeability pathways in Plasmodium falciparum--infected erythrocytes--a kinetic analysis." Exp Parasitol **114**(4): 253-8.

Krugliak, M., J. Zhang, et al. (2002). "Intraerythrocytic Plasmodium falciparum utilizes only a fraction of the amino acids derived from the digestion of host cell cytosol for the biosynthesis of its proteins." Mol Biochem Parasitol **119**(2): 249-56.

Kubinova, L., J. Janacek, et al. (1999). "Comparison of several digital and stereological methods for estimating surface area and volume of cells studied by confocal microscopy." Cytometry **36**(2): 85-95.

Lakowicz, J. R. (1999). Principles of Fluorescence Spectroscopy. New York, Kluwer / Academic Plenum.

Lambros, C. and J. P. Vanderberg (1979). "Synchronization of Plasmodium falciparum erythrocytic stages in culture." J Parasitol **65**(3): 418-20.

Lautenschlager, F., S. Paschke, et al. (2009). "The regulatory role of cell mechanics for migration of differentiating myeloid cells." Proc Natl Acad Sci U S A **106**(37): 15696-701.

Lebedev, P. (1901). "Untersuchungen über die Druckkräfte des Lichts." Annalen der Physik **311**(11): 433-458.

Lee, P., Z. Ye, et al. (1988). "X-ray microanalysis of Plasmodium falciparum and infected red blood cells: effects of qinghaosu and chloroquine on potassium, sodium, and phosphorus composition." Am J Trop Med Hyg **39**(2): 157-65.

Lew, V. L. and R. M. Bookchin (1986). "Volume, pH, and ion-content regulation in human red cells: analysis of transient behavior with an integrated model." J Membr Biol **92**(1): 57-74.

Lew, V. L. and R. M. Bookchin (2005). "Ion transport pathology in the mechanism of sickle cell dehydration." Physiol Rev **85**(1): 179-200.

Lew, V. L., Z. Etzion, et al. (1993). "The Distribution of Intracellular Calcium Chelator (Fura-2) in a Population of Intact Human Red-Cells." Biochimica Et Biophysica Acta **1148**(1): 152-156.

Lew, V. L., C. J. Freeman, et al. (1991). "A mathematical model of the volume, pH, and ion content regulation in reticulocytes. Application to the pathophysiology of sickle cell dehydration." J Clin Invest **87**(1): 100-12.

Lew, V. L., A. Hockaday, et al. (1988). "Mechanism of spontaneous inside-out vesiculation of red cell membranes." J Cell Biol **106**(6): 1893-901.

Lew, V. L. and R. A. Hockaday (1999). The effects of transport perturbations on the homeostasis of erythrocytes. Transport and trafficking in the malaria-infected erythrocyte. G. Bock and R. Cardew, Wiley & Sons**:** 37-54.

Lew, V. L., L. Macdonald, et al. (2004). "Excess haemoglobin digestion by malaria parasites: a strategy to prevent premature host cell lysis." Blood Cells Mol Dis **32**(3): 353-9.

Lew, V. L., J. E. Raftos, et al. (1995). "Generation of normal human red cell volume, hemoglobin content, and membrane area distributions by "birth" or regulation?" Blood **86**(1): 334-41.

Lew, V. L., T. Tiffert, et al. (2003). "Excess hemoglobin digestion and the osmotic stability of Plasmodium falciparum-infected red blood cells." Blood **101**(10): 4189-94.

Lew, V. L., T. Tiffert, et al. (2004). "Response to: Allen and Kirk: Cell volume control in the Plasmodium-infected erythrocyte." Trends in Parasitology **20**(1): 10-11.

Lew, V. L., R. Y. Tsien, et al. (1982). "Physiological [Ca2+]i level and pump-leak turnover in intact red cells measured using an incorporated Ca chelator." Nature **298**(5873): 478-81.

Liang, H., K. T. Vu, et al. (1996). "Wavelength dependence of cell cloning efficiency after optical trapping." Biophysical Journal **70**(3): 1529-1533.

Lincoln, B. (2006). The Microfluidic Optical Stretcher. Fakultät für Physik und Geowissenschaften. Leipzig, Universität Leipzig. **PhD thesis:** 142.

Lincoln, B., S. Schinkinger, et al. (2007). "Reconfigurable microfluidic integration of a dual-beam laser trap with biomedical applications." Biomed Microdevices **9**(5): 703-10.

Lincoln, B., F. Wottawah, et al. (2007). "High-throughput rheological measurements with an optical stretcher." Methods Cell Biol **83**: 397-423.

Liu, X., Z. Y. Tang, et al. (2007). "The measurement of shear modulus and membrane surface viscosity of RBC membrane with Ektacytometry: a new technique." Math Biosci **209**(1): 190-204.

Liu, Y. P., C. Li, et al. (2006). "The deformation of an erythrocyte under the radiation pressure by optical stretch." J Biomech Eng **128**(6): 830-6.

Malm, H., G. Sparr, et al. (2000). "Nonlinear diffusion filtering of images obtained by planar laser-induced fluorescence spectroscopy." Journal of the Optical Society of America a-Optics Image Science and Vision **17**(12): 2148-2156.

Marinkovic, M., M. Diez-Silva, et al. (2009). "Febrile temperature leads to significant stiffening of Plasmodium falciparum parasitized erythrocytes." Am J Physiol Cell Physiol **296**(1): C59-64.

Mauritz, J., A. Esposito, et al. (2010). "Biophotonic techniques for the study of malaria-infected red blood cells." Medical and Biological Engineering and Computing **48**(10):1055-63.

Mauritz, J., R. Seear, et al. (2011). X-ray microanalysis investigation of the changes in Na, K, and hemoglobin concentration in plasmodium falciparum-infected red blood cells. Biophysical Journal **100**(6): 1438-45.

Mauritz, J. M., A. Esposito, et al. (2009). "The homeostasis of Plasmodium falciparum-infected red blood cells." PLoS Comput Biol **5**(4): e1000339.

Mauritz, J. M., T. Tiffert, et al. (2010). "Detection of Plasmodium falciparum-infected red blood cells by optical stretching." J Biomed Opt **15**(3): 030517.

Maxwell, J. C. (1873). A treatise on electricity and magnetism. Oxford at the Clarendon Press, Macmillan and Co.

McConaghey, P. D. and M. Maizels (1961). "The osmotic coefficients of haemoglobin in red cells under varying conditions." J Physiol **155**: 28-45.

Meschede, D. (2005). Optik, Licht und Laser. Wiesbaden, B.G. Teubner Verlag.

Miller, L. H., S. Chien, et al. (1972). "Decreased deformability of Plasmodium coatneyi-infected red cells and its possible relation to cerebral malaria." Am J Trop Med Hyg **21**(2): 133-7.

Miller, L. H., M. F. Good, et al. (1994). "Malaria pathogenesis." Science **264**(5167): 1878-83.

Miller, L. H., S. Usami, et al. (1971). "Alteration in the rheologic properties of Plasmodium knowlesi--infected red cells. A possible mechanism for capillary obstruction." J Clin Invest **50**(7): 1451-5.

Morgan, A., J. Brock, et al. (1994). "Mapping Metal distributions in thin cryosections without scanning transmission electron microscope with the Phillips Electron beam and image deflection (EBID) unit." Scanning Microsc Suppl **8**: 231-243.

Nash, G. B., E. O'Brien, et al. (1989). "Abnormalities in the mechanical properties of red blood cells caused by Plasmodium falciparum." Blood **74**(2): 855-61.

Naughton, J. A., S. Nasizadeh, et al. (2010). "Downstream effects of haemoglobinase inhibition in Plasmodium falciparum-infected erythrocytes." Mol Biochem Parasitol **173**(2): 81-7.

Neuman, K. C., E. H. Chadd, et al. (1999). "Characterization of photodamage to Escherichia coli in optical traps." Biophysical Journal **77**(5): 2856-2863.

Nichols, E. F. and G. F. Hull (1901). "A preliminary communication on the pressure of heat and light radiation." Phys. Rev. **13**: 307-320.

Omodeo-Sale, F., A. Motti, et al. (2003). "Accelerated senescence of human erythrocytes cultured with Plasmodium falciparum." Blood **102**(2): 705-11.

Orjih, A. U., H. S. Banyal, et al. (1981). "Hemin lyses malaria parasites." Science **214**(4521): 667-9.

Overman, R. R. (1947). "Reversible permeability alterations in the erythrocytes of the malarious monkey." Fed Proc **6**(1 Pt 2): 174.

Park, Y. K., M. Diez-Silva, et al. (2008). "Refractive index maps and membrane dynamics of human red blood cells parasitized by Plasmodium falciparum." Proceedings of the National Academy of Sciences of the United States of America **105**(37): 13730-13735.

Pasvol, G., R. J. Wilson, et al. (1978). "Separation of viable schizont-infected red cells of Plasmodium falciparum from human blood." Ann Trop Med Parasitol **72**(1): 87-8.

Paulitschke, M. and G. B. Nash (1993). "Membrane rigidity of red blood cells parasitized by different strains of Plasmodium falciparum." J Lab Clin Med **122**(5): 581-9.

Paulitschke, M., G. B. Nash, et al. (1995). "Perturbation of red blood cell membrane rigidity by extracellular ligands." Blood **86**(1): 342-8.

Paulitschke, M., A. Preece, et al. (1994). "Effect of neuraminidase on rigidity of the red cell membrane." Biorheology **31**(6): 643-50.

Pelet, S., M. J. Previte, et al. (2006). "Comparing the quantification of Forster resonance energy transfer measurement accuracies based on intensity, spectral, and lifetime imaging." J.Biomed.Opt. **11**(3): 34017.

Ponder, E. (1948). Hemolysis and related phenomena. New York, Grune & Stratton.

Przyborski, J. M. (2008). "The Maurer's clefts of Plasmodium falciparum: parasite-induced islands within an intracellular ocean." Trends Parasitol **24**(7): 285-8.

Remmerbach, T. W., F. Wottawah, et al. (2009). "Oral cancer diagnosis by mechanical phenotyping." Cancer Res **69**(5): 1728-32.

Ridley, R. G., A. Dorn, et al. (1997). "Haematin (haem) polymerization and its inhibition by quinoline antimalarials." Ann Trop Med Parasitol **91**(5): 559-66.

Roberts, D. J., A. G. Craig, et al. (1992). "Rapid switching to multiple antigenic and adhesive phenotypes in malaria." Nature **357**(6380): 689-92.

Roberts, K. E., A. K. O'Keeffe, et al. (2003). "Selective dequenching by photobleaching increases fluorescence probe visibility." Journal of Fluorescence **13**(6): 513-517.

Rohrbach, P., O. Friedrich, et al. (2005). "Quantitative calcium measurements in subcellular compartments of Plasmodium falciparum-infected erythrocytes." J Biol Chem **280**(30): 27960-9.

Saliba, K. J., H. A. Horner, et al. (1998). "Transport and metabolism of the essential vitamin pantothenic acid in human erythrocytes infected with the malaria parasite Plasmodium falciparum." J Biol Chem **273**(17): 10190-5.

Savitz, D., V. W. Sidel, et al. (1964). "Osmotic Properties of Human Red Cells." J Gen Physiol **48**: 79-94.

Shelby, J. P., J. White, et al. (2003). "A microfluidic model for single-cell capillary obstruction by Plasmodium falciparum-infected erythrocytes." Proc Natl Acad Sci U S A **100**(25): 14618-22.

Sieracki, M. E., S. E. Reichenbach, et al. (1989). "Evaluation of automated threshold selection methods for accurately sizing microscopic fluorescent cells by image analysis." Appl Environ Microbiol **55**(11): 2762-72.

Sikanen, T., S. Tuomikoski, et al. (2005). "Characterization of SU-8 for electrokinetic microfluidic applications." Lab on a Chip **5**(8): 888-896.

Simpson, J. A., K. Silamut, et al. (1999). "Red cell selectivity in malaria: a study of multiple-infected erythrocytes." Trans R Soc Trop Med Hyg **93**(2): 165-8.

Somlyo, A. V., G. McClellan, et al. (1985). "Electron probe X-ray microanalysis of post-tetanic Ca2+ and Mg2+ movements across the sarcoplasmic reticulum in situ." J Biol Chem **260**(11): 6801-7.

Staines, H. M., A. Alkhalil, et al. (2007). "Electrophysiological studies of malaria parasite-infected erythrocytes: current status." Int J Parasitol **37**(5): 475-82.

Staines, H. M., J. C. Ellory, et al. (2001). "Perturbation of the pump-leak balance for Na(+) and K(+) in malaria-infected erythrocytes." Am J Physiol Cell Physiol **280**(6): C1576-87.

Suresh, S. (2006). "Mechanical response of human red blood cells in health and disease: Some structure-property-function relationships." Journal of Materials Research **21**(8): 1871-1877.

Suresh, S., J. Spatz, et al. (2005). "Connections between single-cell biomechanics and human disease states: gastrointestinal cancer and malaria." Acta Biomater **1**(1): 15-30.

Svetina, S. (1982). "Relations among variations in human red cell volume, density, membrane area, hemoglobin content and cation content." J Theor Biol **95**(1): 123-34.

Swietach, P., T. Tiffert, et al. (2011). "Hydrogen ion dynamics in human red blood cells." J Physiol **588**(24): 4995-5014.

Tabik, S., E. M. Garzon, et al. (2007). "High performance noise reduction for biomedical multidimensional data." Digital Signal Processing **17**(4): 724-736.

Tadir, Y., W. H. Wright, et al. (1990). "Force Generated by Human Sperm Correlated to Velocity and Determined Using a Laser Generated Optical Trap." Fertility and Sterility **53**(5): 944-947.

Taraschi, T. F., M. O'Donnell, et al. (2003). "Generation of an erythrocyte vesicle transport system by Plasmodium falciparum malaria parasites." Blood **102**(9): 3420-6.

Tiffert, T., J. Garcia-Sancho, et al. (1984). "Irreversible ATP depletion caused by low concentrations of formaldehyde and of calcium-chelator esters in intact human red cells." Biochim Biophys Acta **773**(1): 143-56.

Tiffert, T., H. M. Staines, et al. (2000). "Functional state of the plasma membrane Ca2+ pump in Plasmodium falciparum-infected human red blood cells." J Physiol **525 Pt 1**: 125-34.

Tokumasu, F. and J. Dvorak (2003). "Development and application of quantum dots for immunocytochemistry of human erythrocytes." J Microsc **211**(Pt 3): 256-61.

Tokumasu, F., R. M. Fairhurst, et al. (2005). "Band 3 modifications in Plasmodium falciparum-infected AA and CC erythrocytes assayed by autocorrelation analysis using quantum dots." J Cell Sci **118**(Pt 5): 1091-8.

Trager, W. and J. B. Jensen (1976). "Human malaria parasites in continuous culture." Science **193**(4254): 673-5.

van Ham, T. J., A. Esposito, et al. (2010). "Towards Multiparametric Fluorescent Imaging of Amyloid Formation: Studies of a YFP Model of alpha-Synuclein Aggregation." Journal of Molecular Biology **395**(3): 627-642.

Vandorpe, D. H., B. E. Shmukler, et al. (1998). "cDNA cloning and functional characterization of the mouse Ca2+-gated K+ channel, mIK1. Roles in regulatory volume decrease and erythroid differentiation." J Biol Chem **273**(34): 21542-53.

Warley, A. (1997). X-ray Microanalysis for Biologists. London and Miami, Portland Press.

Warley, A. and J. N. Skepper (2000). "Long freeze-drying times are not necessary during the preparation of thin sections for X-ray microanalysis." J Microsc **198**(Pt 2): 116-23.

Wei, M. T., K. T. Yang, et al. (2006). "Three-dimensional optical force field on a Chinese hamster ovary cell in a fiber-optical dual-beam trap." Opt Express **14**(7): 3056-64.

Whitham, R. (1964). Transport and Diffusion in Red Blood Cells. London, Edward Arnold.

WHO (2009). World Malaria Report 2009, World Health Organization, ISBN 978 92 4 156390 1.

Wouters, F. S. and A. Esposito (2008). "Quantitative analysis of fluorescence lifetime imaging made easy." HFSP journal **2**(1): 7.

Wouters, F. S., P. J. Verveer, et al. (2001). "Imaging biochemistry inside cells." Trends in Cell Biology **11**(5): 203-211.

Wunsch, S., C. P. Sanchez, et al. (1998). "Differential stimulation of the Na+/H+ exchanger determines chloroquine uptake in Plasmodium falciparum." J Cell Biol **140**(2): 335-45.

Xu, F., J. A. Lock, et al. (2009). "Optical stress on the surface of a particle: Homogeneous sphere." Physical Review A (Atomic, Molecular, and Optical Physics) **79**(5): 053808-15.

Yu, J. T., J. Y. Chen, et al. (2005). "Surface stress on the erythrocyte under laser irradiation with finite-difference time-domain calculation." J Biomed Opt **10**(6): 064013.

Zanner, M. A., W. R. Galey, et al. (1990). "Water and urea transport in human erythrocytes infected with the malaria parasite Plasmodium falciparum." Mol Biochem Parasitol **40**(2): 269-78.

Zarchin, S., M. Krugliak, et al. (1986). "Digestion of the host erythrocyte by malaria parasites is the primary target for quinoline-containing antimalarials." Biochem Pharmacol **35**(14): 2435-42.